Mon. Not. R. Astron. Soc. **000**, 000–000 (0000) Printed 22 August 2012 (MN LATEX style file v2.2)

Homogeneous studies of transiting extrasolar planets. V. New results for 38 planets

John Southworth⋆
Astrophysics Group, Keele University, Staffordshire, ST5 5BG, UK

22 August 2012

ABSTRACT

I measure the physical properties of 38 transiting extrasolar planetary systems, bringing the total number studied within the *Homogeneous Studies* project to 82. Transit light curves are modelled using the JKTEBOP code, with careful attention paid to limb darkening, orbital eccentricity and contaminating light. The physical properties of each system are obtained from the photometric parameters, published spectroscopic measurements and five sets of theoretical stellar model predictions. Statistical errors are assessed using Monte Carlo and residual-permutation algorithms and propagated via a perturbation algorithm. Systematic errors are estimated from the interagreement between results calculated using five theoretical stellar models.

The headline result is a major upward revision of the radius of the planet in the OGLE-TR-56 system, from 1.23–$1.38\,\mathrm{R_{Jup}}$ to $1.734 \pm 0.051 \pm 0.029\,\mathrm{R_{Jup}}$ (statistical and systematic errors, respectively). Its density is three times lower than previously thought. This change comes from the first complete analysis of published high-quality photometry. Significantly larger planetary radii are also found for Kepler-15, KOI-428, WASP-13, WASP-14 and WASP-21 compared to previous work.

I present the first results based on *Kepler* short-cadence data for Kepler-14, Kepler-15 and KOI-135. More extensive long-cadence data from the *Kepler* satellite is used to improve the measured properties of KOI-196, KOI-204, KOI-254, KOI-423 and KOI-428. The stellar component in the KOI-428 system is the largest known to host a transiting planet, at $2.48 \pm 0.17 \pm 0.20\,\mathrm{R_\odot}$. Detailed analyses are given for HAT-P-3, HAT-P-6, HAT-P-9, HAT-P-14 and WASP-12, based on more extensive datasets than considered in previous studies.

Detailed analyses are also presented for the CoRoT systems 17, 18, 19, 20 and 23; Kepler-7, 12 and 17; KOI-254; OGLE-TR- 111, 113, 132 and L9; and TrES-4.

I revisit the correlations between orbital period and surface gravity, and orbital period and mass of the transiting planets, finding both to be significant at the 4σ level. I conclude by discussing the opportunities for follow-up observations, the sky positions and the discovery rate of the known transiting planets.

Key words: stars: planetary systems — stars: fundamental parameters

1 INTRODUCTION

Even though the first transiting extrasolar planet (TEP) was discovered only as recently as 1999 (Henry et al. 2000; Charbonneau et al. 2000), the number of recognised TEPs – and the size of the literature on them – has grown very quickly. The known planetary systems now display a bewildering diversity of qualities: from super-Earths with extremely short periods (CoRoT-7 b; Léger et al. 2009) to massive planets on wide and highly eccentric orbits (HD 80606 b; Hébrard et al. 2010); a system of six planets showing strong mutual gravitational perturbations (Kepler-11; Lissauer et al. 2011); circumbinary planets (Doyle et al. 2011; Welsh et al. 2012); and ones with a size inexplicably approaching twice that of Jupiter (WASP-17 b; Anderson et al. 2010; Southworth et al. 2012b).

Part of the reason for the known TEP population being such a menagerie is the variety of methods deployed in catching them. Many of the TEPs orbiting brighter stars (including the first, HD 209458 b) were found by radial velocity surveys and later shown to transit. Others (such as the second known TEP OGLE-TR-56 b; Konacki et al. 2003) were unearthed via deep photometric searches and subsequently confirmed spectroscopically. The dominant population of TEPs currently stems from large-scale photometric surveys of stars of intermediate brightness ($V = 9$–13) coupled with spectroscopic follow-up programs, such as those of HAT (Bakos et al. 2002) and WASP (Pollacco et al. 2006). This population is strongly biased towards larger planets with orbital periods

⋆ E-mail: jkt@astro.keele.ac.uk

$P_{\rm orb} \lesssim 10$ d, as these *Hot Jupiters* show the greatest photometric variability. More recently, surveys such as CoRoT and *Kepler* have found success by obtaining uninterrupted photometry of stars using space satellites. The objects found in this way – like the deep ground-based surveys – mostly orbit fainter stars, which hinders attempts to obtain follow-up observations to refine their physical properties or even spectroscopically confirm the planetary nature of the transiting body.

An important problem with the study of TEPs is that their physical properties cannot be obtained simply by measuring some observable quantities and putting them through standard formulae: the number of quantities measurable directly from observations is one too few. An *additional constraint* is therefore needed, which is usually obtained by requiring the physical properties of the host star to match the predictions of stellar theory. In practise, there are several ways of implementing this constraint, and multiple sets of theoretical predictions from which to choose. As different researchers select different approaches, their results are inhomogeneous and therefore non-trivial to compare.

The diversity of the known TEPs, coupled with the varied methods used in their analysis, makes a consistent picture of their properties more difficult to attain. The current series of papers is an attempt to perform a uniform analysis for all suitable TEP systems, in order to produce homogeneous measurements of their physical properties. Such results are valuable in statistical investigations of the characteristics of this population (such as work similar to that by Enoch et al. 2012), as well as providing an independent confirmation (or otherwise) of published numbers. In some cases it is possible to achieve improved results simply by considering all available data rather than concentrating on only one set of observations.

In Paper I (Southworth 2008) I presented the methods used for analysing the transit photometry of TEP systems, and applied them to the fourteen object which had good light curves at that point. Paper II (Southworth 2009) discussed the more thorny issue of how to turn the measured photometric and spectroscopic parameters into physical properties; the primary problem here is the need to incorporate the predictions of theoretical stellar evolutionary models (or some other additional constraint) into the process. This was achieved for the fourteen TEPs by using three sets of stellar models, plus an empirical stellar mass–radius relation as an alternative constraint. In Paper III (Southworth 2010) the net was widened to include the full analysis of 30 TEPs with five sets of stellar models, plus a description of the methods used to incorporate contaminating light and orbital eccentricity into the analysis. Paper IV (Southworth 2011) further extended the project to include 58 TEPs, concentrating on those which had space-based light curves from CoRoT, *Kepler*, or the NASA Epoxi satellites. An improved empirical constraint was also used (based on stellar density, temperature and metal abundance), calibrated on the measured properties of 180 stars in 90 detached eclipsing binaries.

In this work I present new photometric analyses of 30 more TEPs, and measure the physical properties of these plus a further eight objects previously considered in the current project. This brings the total number of TEPs within the *Homogeneous Studies* project to 82. Whilst this is by far the largest source of homogeneous physical properties, it still represents less than half of the known TEP systems. The physical properties, follow-up status, sky positions and discovery rate of the known TEPs are finally discussed in Sections 6 to 8. As with previous papers in this series, extensive tables of intermediate results are available for inspection in the online-only Supplementary Information.

2 LIGHT CURVE ANALYSIS

I have studied the light curves of each TEP system using the methods discussed in detail in Paper I. The JKTEBOP[1] code was used to find the best-fitting model for each light curve, from which the photometric parameters were extracted. JKTEBOP represents the star and planet as biaxial spheroids with shapes governed by the mass ratio. The results in this work are all very insensitive to the adopted mass ratio, in part because the projected surfaces of the stars suffer the least distortions from sphericity close to the times of transit and occultation. The correct terminology for transits (primary eclipses) and occultations (secondary eclipses) was discussed in sect. 4 of Paper IV.

The main parameters for JKTEBOP are the orbital inclination (i), and fractional radii of the star ($r_{\rm A}$) and planet ($r_{\rm b}$), defined as:

$$r_{\rm A} = \frac{R_{\rm A}}{a} \qquad\qquad r_{\rm b} = \frac{R_{\rm b}}{a} \tag{1}$$

where a is the orbital semimajor axis, and $R_{\rm A}$ and $R_{\rm b}$ are the volume-equivalent stellar and planetary radii. In this work I fitted for the sum and ratio of the fractional radii:

$$r_{\rm A} + r_{\rm b} \qquad\qquad k = \frac{r_{\rm b}}{r_{\rm A}} = \frac{R_{\rm b}}{R_{\rm A}} \tag{2}$$

as these are less strongly correlated. In all cases the time of transit midpoint (T_0) was included as a fitted parameter. When modelling one transit, the orbital period ($P_{\rm orb}$) was fixed to a value taken from the literature. When modelling multiple transits at the same time, $P_{\rm orb}$ was included as a fitted parameter.

Limb darkening (LD) was considered in detail. Every light curve was solved with each of five different LD laws (see Paper I) and with three different approaches to the LD coefficients: (1) both fixed ('LD-fixed'); (2) the linear coefficients ($u_{\rm A}$) fitted and the nonlinear coefficients ($v_{\rm A}$) fixed but perturbed[2] by ±0.10 in the error analysis simulations ('LD-fit/fix'); (3) both coefficients fitted ('LD-fitted'). In a few cases where the photometric data are of limited quality the LD-fitted alternatives were not calculated. Initial or fixed values for the LD coefficients were obtained by bilinear interpolation to the correct $T_{\rm eff}$ and $\log g$ within tabulated theoretical predictions[3]. Once the best of the three options (LD-fixed, LD-fit/fix, LD-fitted) was determined, the final light curve parameters were taken to be the weighted mean of the relevant results for the four nonlinear laws.

Errorbars for the parameters were obtained from 1000 Monte Carlo (MC) simulations (Southworth et al. 2004), for each of the solutions with the adopted approach to LD. The largest of these was retained, and an additional contribution added to reflect any variation in the parameter values from the four nonlinear LD laws. Finally, alternative errorbars were calculated using a residual permutation (RP) algorithm (as implemented in Paper I), which accounts for correlated noise. The RP errorbars were adopted if they were greater than the MC equivalents.

Any contaminating 'third' light (e.g. Daemgen et al. 2009),

[1] JKTEBOP is written in FORTRAN77 and the source code is available at `http://www.astro.keele.ac.uk/jkt/codes/jktebop.html`

[2] The size of the perturbation was incorrectly stated to be ±0.05 in Paper IV, rather than the true value of ±0.10. I thank the referee of a previous paper (Southworth et al. 2012a) for bringing this to my attention.

[3] Interpolation within multiple tables of theoretical LD coefficients was performed using the JKTLD code, written in FORTRAN77 and available at `http://www.astro.keele.ac.uk/jkt/codes/jktld.html`

denoted by L_3, was included as a constraint following the procedure of Southworth et al. (2010). A detailed investigation of the issue of third light was given in Paper III. Orbital eccentricity was treated similarly (Southworth et al. 2009c), with constraints on the combinations $e\cos\omega$ and $e\sin\omega$ preferred over those for eccentricity (e) and periastron longitude (ω) directly (see Paper III). Numerical integration over long exposure times is important for several TEPs, most notably those observed in long cadence by the *Kepler* satellite, and was dealt with in JKTEBOP following the scheme given in Paper IV.

3 CALCULATION OF PHYSICAL PROPERTIES

The analysis of transit light curves gives the orbital ephemeris ($P_{\rm orb}$, T_0) and the photometric parameters ($r_{\rm A}$, $r_{\rm b}$ and i). For each system we also have the orbital velocity amplitude of the host star ($K_{\rm A}$). These measured parameters alone do not lead to a unique solution for the physical properties of the system, so an additional constraint has to be sought from elsewhere. The possible constraints are outlined below[4]

In each case, the physical properties calculated were the mass, radius, surface gravity and density of the star ($M_{\rm A}$, $R_{\rm A}$, $\log g_{\rm A}$, $\rho_{\rm A}$) and of the planet ($M_{\rm b}$, $R_{\rm b}$, $g_{\rm b}$, $\rho_{\rm b}$), a surrogate for the planetary equilibrium temperature:

$$T'_{\rm eq} = T_{\rm eff}\left(\frac{R_{\rm A}}{2a}\right)^{1/2} = T_{\rm eff}\left(\frac{r_{\rm A}}{2}\right)^{1/2} \quad (3)$$

and the Safronov (1972) number:

$$\Theta = \frac{1}{2}\left(\frac{V_{\rm esc}}{V_{\rm orb}}\right)^2 = \left(\frac{a}{R_{\rm b}}\right)\left(\frac{M_{\rm b}}{M_{\rm A}}\right) = \frac{1}{r_{\rm b}}\frac{M_{\rm b}}{M_{\rm A}} \quad (4)$$

The set of physical constants used in the process above were tabulated in sect. 3.3 of Paper IV[5], and are very close to the values proposed to the astronomical community by Harmanec & Prša (2011).

3.1 Additional constraint from theoretical stellar models

The standard approach in obtaining the additional constraint is to use the predictions of theoretical stellar evolutionary models. These provide the mass and radius of the host star, guided by determinations of its effective temperature ($T_{\rm eff}$), metal abundance ($\left[\frac{\rm Fe}{\rm H}\right]$) and light-curve-derived density (Seager & Mallén-Ornelas 2003). The full physical properties of the system are then straightforward to calculate. I adopted the procedure introduced in Paper II, which begins with estimating the velocity amplitude of the *planet* ($K_{\rm b}$). The other measured quantities ($P_{\rm orb}$, $K_{\rm A}$, $r_{\rm A}$, $r_{\rm b}$, i, e) were used to determine the ensuing physical properties using standard formulae (e.g. Hilditch 2001). The value of $K_{\rm b}$ could then be iteratively refined to minimise the figure of merit

$$\text{fom} = \left[\frac{r_{\rm A}^{\rm (obs)} - (R_{\rm A}^{\rm (calc)}/a)}{\sigma(r_{\rm A}^{\rm (obs)})}\right]^2 + \left[\frac{T_{\rm eff}^{\rm (obs)} - T_{\rm eff}^{\rm (calc)}}{\sigma(T_{\rm eff}^{\rm (obs)})}\right]^2 \quad (5)$$

where $r_{\rm A}^{\rm (obs)}$ and $T_{\rm eff}^{\rm (obs)}$ are quantities determined from observations. $R_{\rm A}^{\rm (calc)}$ and $T_{\rm eff}^{\rm (calc)}$ were obtained for a given $K_{\rm b}$ value by interpolating in the tabulations of theoretical models for the calculated mass and observed $\left[\frac{\rm Fe}{\rm H}\right]$ of the star. The outcome of this procedure is a set of physical properties corresponding to the best agreement between observed and calculated quantities. The solution control parameter, $K_{\rm b}$, represents the entirety of the input from theoretical stellar models. Because the evolution of a star is highly non-linear with time, the above procedure was carried out for a range of ages starting from 0.01 Gyr and incrementing in 0.01 Gyr chunks until the star was significantly evolved (surface gravity $\log g < 3.5$). This led to a set of overall best physical properties plus a model-dependent estimate of the age of the system.

The statistical uncertainties on the input parameters were propagated using a perturbation analysis (Southworth et al. 2005) implemented in the JKTABSDIM code. This had the additional benefit of yielding a complete error budget for every output parameter, allowing identification of how best to improve our understanding of each TEP. The use of theoretical stellar models also incurs a systematic error due to our incomplete understanding of stellar physics. I therefore ran JKTABSDIM solutions for each of five sets of theoretical models (see Paper III): *Claret* (Claret 2004, 2005, 2006, 2007), *Y*^{2} (Demarque et al. 2004), *Teramo* (Pietrinferni et al. 2004), *VRSS* (VandenBerg et al. 2006) and *DSEP* (Dotter et al. 2008). This yielded five sets of values and statistical errorbars for each output parameter. For the final result for each parameter I have taken the unweighted mean of the five values. The largest of the individual statistical errors was adopted as the final statistical error, and the standard deviation of the five values was taken to represent the systematic error.

Three of the derived physical properties have no dependence on stellar theory so are quoted without systematic errorbars: $g_{\rm b}$ (Southworth et al. 2007); $\rho_{\rm A}$ to a good approximation (Seager & Mallén-Ornelas 2003); and $T'_{\rm eq}$ (Paper III).

3.2 Additional constraint from eclipsing binary relations

In Paper II I found a way to avoid the use of stellar models entirely, by defining an empirical mass–radius relation based on well-studied eclipsing binaries. This approach was not very successful because it did not allow for either the chemical composition or evolution of the host star. It was also subject to the known phenomenon that the components of low-mass eclipsing binaries tend to have larger radii and lower $T_{\rm eff}$s than those predicted by stellar theory (e.g. López-Morales 2007; Ribas et al. 2008).

An alternative approach is to explicitly include a dependence on $T_{\rm eff}$ and $\left[\frac{\rm Fe}{\rm H}\right]$. Enoch et al. (2010) proposed a set of calibration equations giving $\log M$ or $\log R$ as functions of ρ, $T_{\rm eff}$ and $\left[\frac{\rm Fe}{\rm H}\right]$, where ρ was chosen because a very good approximation to this quantity is calculable directly from transit light curves (Seager & Mallén-Ornelas 2003). In Paper IV I adopted this approach, but with modified calibration coefficients obtained from a larger and better-conditioned sample of eclipsing binary systems[6]. A similar re-calibration has been performed by Gillon et al. (2011).

In the current work I have calculated the physical properties

[4] A small fraction of TEP systems have direct distance measurements from parallaxes, or stellar diameter measurements from interferometry (e.g. von Braun et al. 2012). These observations can supply the crucial additional constraint, but are not possible for most TEP host stars due to their distance from the Earth.

[5] The radius of the Sun and of Jupiter were wrong by a factor of ten in sect. 3.3 of Paper IV, due to a typographical error. The correct values are 6.95508×10^8 m and 7.1492×10^7 m respectively. This does not affect any of the calculations in Paper IV or other analyses by the current author.

[6] See the catalogue of well-studied detached eclipsing binary star systems: `http://www.astro.keele.ac.uk/~jkt/debcat/`

Table 1. Final photometric parameters for the 38 TEPs analysed in this work. Orbital periods are also given, and are either from this work or taken from the literature. Systems for which a constraint on orbital eccentricity or third light was required, are marked using a $\star$ in the column headed "e?" or "L_3?".

System	Orbital period (days)	e?	L_3?	Orbital inclination, i (degrees)	Fractional stellar radius, $r_{\rm A}$	Fractional planetary radius, $r_{\rm b}$	Reference
CoRoT-2	1.7429935 (10)	$\star$	$\star$	87.45 ± 0.34	0.1478 ± 0.0023	0.02462 ± 0.00035	Paper IV
CoRoT-17	3.7681 (3)		$\star$	$89.3^{+0.7}_{-4.9}$	$0.157^{+0.043}_{-0.012}$	$0.0100^{+0.0034}_{-0.0009}$	This work
CoRoT-18	1.9000693 (28)		$\star$	86.8 ± 1.7	0.1502 ± 0.0072	0.0209 ± 0.0013	This work
CoRoT-19	3.89713 (2)			$89.7^{+0.3}_{-3.6}$	$0.143^{+0.028}_{-0.007}$	$0.0111^{+0.0024}_{-0.0006}$	This work
CoRoT-20	9.24285 (30)			83.5 ± 3.8	0.070 ± 0.019	0.0062 ± 0.0014	This work
CoRoT-23	3.6313 (1)	$\star$	$\star$	$84.7^{+3.4}_{-3.0}$	$0.168^{+0.022}_{-0.014}$	$0.0117^{+0.0018}_{-0.0011}$	This work
HAT-P-3	2.8997360 (20)			86.15 ± 0.19	0.1053 ± 0.0020	0.01178 ± 0.00030	This work
HAT-P-6	3.8530030 (14)			84.88 ± 0.51	0.1346 ± 0.0054	0.01271 ± 0.00070	This work
HAT-P-9	3.922814 (2)			86.10 ± 0.54	0.1177 ± 0.0060	0.01250 ± 0.00089	This work
HAT-P-14	4.6276691 (50)	$\star$		83.01 ± 0.27	0.1211 ± 0.0036	0.00954 ± 0.00045	This work
Kepler-7	4.8854922 (38)		$\star$	85.32 ± 0.16	0.1491 ± 0.0013	0.01246 ± 0.00015	This work
Kepler-12	4.4379637 (2)		$\star$	$89.02^{+0.25}_{-0.21}$	$0.12486^{+0.00110}_{-0.00075}$	$0.014687^{+0.000071}_{-0.000068}$	This work
Kepler-14	6.7901230 (43)	$\star$	$\star$	86.64 ± 0.59	0.1260 ± 0.0058	0.00698 ± 0.00029	This work
Kepler-15	4.942782 (13)		$\star$	86.144 ± 0.051	0.10002 ± 0.00048	0.010575 ± 0.000086	This work
Kepler-17	1.4857108 (2)		$\star$	$89.73^{+0.27}_{-0.94}$	$0.1755^{+0.0018}_{-0.0008}$	$0.02403^{+0.00024}_{-0.00013}$	This work
KOI-135	3.0240933 (27)		$\star$	84.89 ± 0.21	0.1409 ± 0.0020	0.01212 ± 0.00025	This work
KOI-196	1.8555588 (15)		$\star$	$89.5^{+0.5}_{-1.6}$	$0.1508^{+0.0091}_{-0.0020}$	$0.01406^{+0.00107}_{-0.00029}$	This work
KOI-204	3.2467220 (73)		$\star$	84.30 ± 0.83	0.1485 ± 0.0090	0.01259 ± 0.00098	This work
KOI-254	2.45524122 (65)	$\star$	$\star$	87.48 ± 0.38	0.0849 ± 0.0040	0.01616 ± 0.00091	This work
KOI-423	21.087168 (21)	$\star$	$\star$	89.06 ± 0.21	0.0370 ± 0.0015	0.00339 ± 0.00017	This work
KOI-428	6.8731697 (96)		$\star$	85.47 ± 0.94	0.1437 ± 0.0072	0.00859 ± 0.00052	This work
OGLE-TR-56	1.21191096 (65)			73.47 ± 0.37	0.3292 ± 0.0048	0.03378 ± 0.00059	This work
OGLE-TR-111	4.0144477 (16)			88.50 ± 0.35	0.0817 ± 0.0018	0.01033 ± 0.00030	This work
OGLE-TR-113	1.43247425 (34)			87.80 ± 0.86	0.1572 ± 0.0020	0.02296 ± 0.00039	This work
OGLE-TR-132	1.68986531 (64)			83.83 ± 0.96	0.2056 ± 0.0078	0.01941 ± 0.00096	This work
OGLE-TR-L9	2.48553417 (64)			82.19 ± 0.21	0.1722 ± 0.0025	0.01928 ± 0.00028	This work
TrES-4	3.5539268 (32)		$\star$	82.33 ± 0.47	0.1697 ± 0.0064	0.01650 ± 0.00059	This work
WASP-1	2.5199464 (8)			88.0 ± 2.0	$0.1737^{+0.0057}_{-0.0089}$	$0.0182^{+0.0007}_{-0.0011}$	Paper I
WASP-2	2.15222144 (39)		$\star$	84.81 ± 0.17	0.1238 ± 0.0018	0.01643 ± 0.00030	Southworth et al. (2010)
WASP-4	1.33823144 (32)			89.0 ± 1.0	$0.1825^{+0.0011}_{-0.0010}$	$0.02812^{+0.00022}_{-0.00014}$	Southworth et al. (2009b)
WASP-5	1.6284246 (13)			85.8 ± 1.1	0.1847 ± 0.0061	0.02050 ± 0.00091	Southworth et al. (2009a)
WASP-7	4.9546416 (35)			87.03 ± 0.93	0.1102 ± 0.0061	0.01053 ± 0.00070	Southworth et al. (2011)
WASP-12	1.0914222 (11)			83.3 ± 1.1	0.3260 ± 0.0052	0.03777 ± 0.00088	This work
WASP-13	4.353011 (13)			84.88 ± 0.45	0.1382 ± 0.0049	0.01310 ± 0.00059	This work
WASP-14	2.2437661 (11)	$\star$		81.1 ± 1.5	0.2084 ± 0.0099	0.0210 ± 0.0010	This work
WASP-18	0.94145181 (44)	$\star$		85.0 ± 2.1	0.2795 ± 0.0084	0.0272 ± 0.0012	Southworth et al. (2009c)
WASP-21	4.3225060 (31)			86.77 ± 0.45	0.1069 ± 0.0037	0.01170 ± 0.00054	This work
XO-2	2.6158640 (16)			88.8 ± 1.2	$0.1237^{+0.0024}_{-0.0047}$	$0.01300^{+0.00033}_{-0.00070}$	Paper III

for each TEP system using equation 7 in Paper IV with the coefficients of the calibration for $\log_{10} R$ covering stellar masses of 0.2–3.0 $\mathrm{M}_{\odot}$. These results are presented as an alternative to the default solutions incorporating the predictions of theoretical stellar models.

4 DATA ACQUISITION

The CoRoT data used here are the N2 public version obtained in FITS format from the public archive[7]. The data for each object exist in short and/or long cadence flavours, with effective integration times of 32 s and 512 s respectively. I used the total flux as given by the "WHITEFLUX" column. The chromatic light curves were not considered as they add little to the results and have passbands which vary from star to star. I rejected any datapoints which were flagged as being unreliable (i.e. I required STATUS $= 0$). Numerical integration was used for the long-cadence data, adopting $N_{\rm int} = 3$ as the number of integration points.

The *Kepler* data used were the public data obtained from the Multimission Archive at STScI (MAST[8]). These also come in two forms: short cadence (effective integration time 58.84876 s; Gilliland et al. 2010) and long cadence (29.4244 min; Jenkins et al. 2010). Numerical integration is crucial for the interpretation of the latter type of data (see Paper IV for a demonstration) and I adopted $N_{\rm int} = 10$ in all cases. The *Kepler* data cover Quarter 0 (Q0) to Quarter 2 (Q2) with additional data up to Quarter 6 (Q6) available for some objects.

In order to account for slow variations in these data, both astrophysical and instrumental, all data more than one transit duration away from a transit were discarded. A straight line was then fitted

[7] `http://idoc-corot.ias.u-psud.fr/`

[8] `http://archive.stsci.edu/kepler/data_search/search.php`

Table 2. Spectroscopic quantities for the TEP host stars, taken from the literature and adopted in the analysis in the present work.

System	Velocity amplitude ($\mathrm{m\,s^{-1}}$)		$T_{\rm eff}$ (K)	Reference	$\left[\frac{\rm Fe}{\rm H}\right]$	Reference
CoRoT-2	603 ± 18	Gillon et al. (2010)	5598 ± 50	Schröter et al. (2011)	0.04 ± 0.05	Schröter et al. (2011)
CoRoT-17	312.4 ± 29.0	Csizmadia et al. (2011)	5740 ± 80	Csizmadia et al. (2011)	0.0 ± 0.1	Csizmadia et al. (2011)
CoRoT-18	590 ± 14	Hébrard et al. (2011b)	5440 ± 100	Hébrard et al. (2011b)	-0.1 ± 0.1	Hébrard et al. (2011b)
CoRoT-19	126 ± 6	Guenther et al. (2012)	6090 ± 70	Guenther et al. (2012)	-0.02 ± 0.10	Guenther et al. (2012)
CoRoT-20	454 ± 9	Deleuil et al. (2012)	5880 ± 90	Deleuil et al. (2012)	0.14 ± 0.12	Deleuil et al. (2012)
CoRoT-23	377 ± 34	Rouan et al. (2012)	5900 ± 100	Rouan et al. (2012)	0.05 ± 0.1	Rouan et al. (2012)
HAT-P-3	89.1 ± 2.0	Torres et al. (2007)	5185 ± 50	Torres et al. (2007)	0.27 ± 0.05	Torres et al. (2007)
HAT-P-6	115.5 ± 4.2	Noyes et al. (2008)	6570 ± 80	Noyes et al. (2008)	-0.13 ± 0.08	Noyes et al. (2008)
HAT-P-9	84.7 ± 7.9	Shporer et al. (2009a)	6350 ± 150	Shporer et al. (2009a)	0.12 ± 0.20	Shporer et al. (2009a)
HAT-P-14	218.9 ± 5.8	Torres et al. (2010)	6600 ± 90	Torres et al. (2010)	0.11 ± 0.08	Torres et al. (2010)
Kepler-7	42.9 ± 3.5	Latham et al. (2010)	5933 ± 50	Latham et al. (2010)	0.11 ± 0.05	Latham et al. (2010)
Kepler-12	$48.2^{+4.3}_{-4.4}$	Fortney et al. (2011)	5947 ± 100	Fortney et al. (2011)	0.07 ± 0.04	Fortney et al. (2011)
Kepler-14	683^{+27}_{-25}	Buchhave et al. (2011)	6395 ± 60	Buchhave et al. (2011)	0.12 ± 0.06	Buchhave et al. (2011)
Kepler-15	$78.7^{+8.5}_{-9.1}$	Endl et al. (2011)	5595 ± 120	Endl et al. (2011)	0.36 ± 0.07	Endl et al. (2011)
Kepler-17	399 ± 9	Bonomo et al. (2012)	5781 ± 85	Bonomo et al. (2012)	0.26 ± 0.10	Bonomo et al. (2012)
KOI-135	375 ± 13	Bonomo et al. (2012)	6041 ± 143	Bonomo et al. (2012)	0.33 ± 0.11	Bonomo et al. (2012)
KOI-196	85 ± 11	Santerne et al. (2011a)	5660 ± 100	Santerne et al. (2011a)	-0.09 ± 0.16	Santerne et al. (2011a)
KOI-204	124 ± 5	Bonomo et al. (2012)	5757 ± 134	Bonomo et al. (2012)	0.26 ± 0.10	Bonomo et al. (2012)
KOI-254	110 ± 10	Johnson et al. (2012)	3820 ± 90	Johnson et al. (2012)	0.20 ± 0.10	Johnson et al. (2012)
KOI-423	1251^{+30}_{-27}	Bouchy et al. (2011)	6260 ± 140	Bouchy et al. (2011)	-0.29 ± 0.10	Bouchy et al. (2011)
KOI-428	179 ± 27	Santerne et al. (2011b)	6510 ± 100	Santerne et al. (2011b)	$0.10^{+0.15}_{-0.10}$	Santerne et al. (2011b)
OGLE-TR-56	212 ± 22	Bouchy et al. (2005)	6119 ± 62	Santos et al. (2006)	0.25 ± 0.08	Santos et al. (2006)
OGLE-TR-111	78 ± 14	Pont et al. (2004)	5044 ± 83	Santos et al. (2006)	0.19 ± 0.07	Santos et al. (2006)
OGLE-TR-113	267 ± 34	Torres et al. (2008)	4790 ± 75	Torres et al. (2008)	0.09 ± 0.08	Torres et al. (2008)
OGLE-TR-132	167 ± 18	Moutou et al. (2004)	6210 ± 59	Gillon et al. (2007)	0.37 ± 0.07	Gillon et al. (2007)
OGLE-TR-L9	510 ± 170	Snellen et al. (2009)	6933 ± 58	Snellen et al. (2009)	-0.05 ± 0.20	Snellen et al. (2009)
TrES-4	97.4 ± 7.2	Mandushev et al. (2007)	6200 ± 75	Sozzetti et al. (2009)	0.14 ± 0.09	Sozzetti et al. (2009)
WASP-1	125 ± 5	Albrecht et al. (2011)	6213 ± 51	Albrecht et al. (2011)	0.17 ± 0.05	Albrecht et al. (2011)
WASP-2	153.6 ± 3.0	Triaud et al. (2010)	5170 ± 60	Sect. 5.31	0.04 ± 0.05	Albrecht et al. (2011)
WASP-4	242.1 ± 3.0	Triaud et al. (2010)	5540 ± 55	Maxted et al. (2011)	-0.03 ± 0.09	Gillon et al. (2009)
WASP-5	268.7 ± 1.8	Triaud et al. (2010)	5770 ± 65	Maxted et al. (2011)	0.09 ± 0.09	Gillon et al. (2009)
WASP-7	97 ± 13	Hellier et al. (2009b)	6520 ± 70	Maxted et al. (2011)	0.00 ± 0.10	Hellier et al. (2009b)
WASP-12	226 ± 4	Hebb et al. (2009)	6250 ± 100	Fossati et al. (2010)	0.32 ± 0.12	Fossati et al. (2010)
WASP-13	55.7 ± 5.5	Skillen et al. (2009)	5826 ± 100	Skillen et al. (2009)	0.0 ± 0.2	Skillen et al. (2009)
WASP-14	990 ± 3	Blecic et al. (2011)	6475 ± 100	Joshi et al. (2009)	0.0 ± 0.2	Joshi et al. (2009)
WASP-18	1816.7 ± 1.9	Triaud et al. (2010)	6455 ± 70	Maxted et al. (2011)	0.00 ± 0.09	Hellier et al. (2009a)
WASP-21	37.2 ± 1.1	Bouchy et al. (2010)	5800 ± 100	Bouchy et al. (2010)	-0.46 ± 0.11	Bouchy et al. (2010)
XO-2	92.2 ± 1.7	Narita et al. (2011)	5340 ± 50	Burke et al. (2007)	0.45 ± 0.05	Burke et al. (2007)

to the data around each transit (not including the datapoints in transit) and divided out to normalise the transit to unit flux. A straight line was in almost all cases sufficient to remove the slow variations, and is also unable to distort the shape of the transit. A few instances where a polynomial was used instead are noted below. In those cases where a large number of datapoints remained, they were converted into orbital phase, sorted, and then phase-binned into a much smaller number of normal points. The amount of binning was carefully chosen to avoid smearing out the transit shape. Details of this process are given below when relevant.

Other data were obtained from public archives, from published papers, and by personal communication when necessary.

5 RESULTS FOR INDIVIDUAL SYSTEMS

In this section I present JKTEBOP and JKTABSDIM analyses of 38 TEPs based on published high-quality data. The results were obtained using the same methods as those in previous papers, leading to homogeneous measurements for a sample of 82 TEPs. The final photometric parameters of the 38 TEPs considered in the current work are aggregated in Table 1, and their adopted spectroscopic parameters are given in Table 2. I have enforced minimum errorbars of ± 50 K for $T_{\rm eff}$ and ± 0.05 dex for $\left[\frac{\rm Fe}{\rm H}\right]$, as the stellar effective temperature and metallicity scales set a lower limit on how precisely we can measure these quantities. Such minimum errorbars may still be optimistic (see e.g. Bruntt et al. 2010a, 2012), and this will be revisited in future.

5.1 CoRoT-17

Discovered by Csizmadia et al. (2011), the CoRoT-17 system harbours a fairly massive planet ($2.46 \pm 0.25\,\mathrm{M_{Jup}}$) around an old star ($8.0^{+1.0}_{-3.9}$ Gyr). The only available light curve is that from the CoRoT satellite, which is comparatively poor due to the faintness of the star ($V = 15.46$). Csizmadia et al. (2011) found that their observations were consistent with a circular orbit, and that the CoRoT light curve is contaminated with a third light of $L_3 = 8 \pm 4\,\%$.

The CoRoT data comprise 10 248 datapoints at 512 s cadence covering 23 transit events. 1571 datapoints in the vicinity of transits were retained (see Sect. 4), of which ten were subsequently rejected

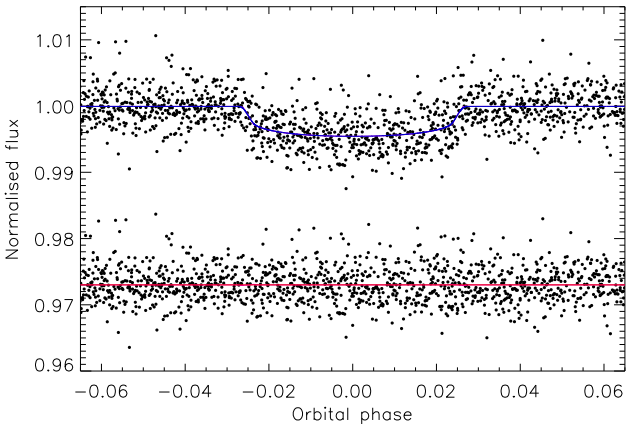

Figure 1. Phased CoRoT 512 s cadence light curve of CoRoT-17 compared to the best fit found using JKTEBOP and the quadratic LD law. The residuals are plotted at the base of the figure, offset from unity. The purple line through the data shows the best-fitting model without numerical integration, and through the residuals shows the difference between this model with and without numerical integration. In this case the purple lines are barely visible behind the other lines.

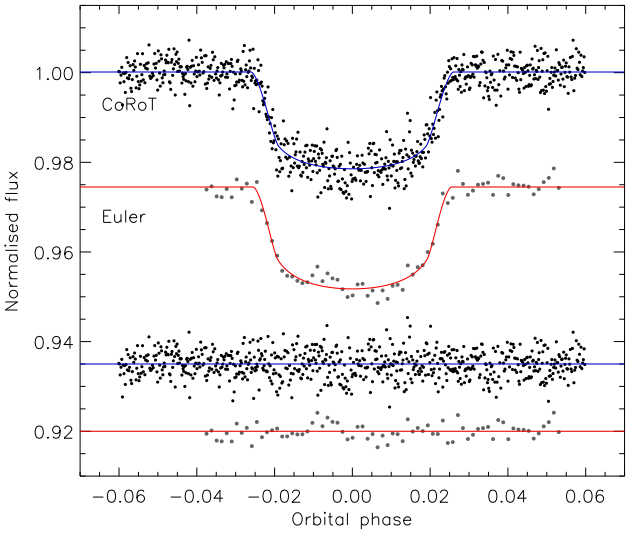

Figure 2. The CoRoT and Euler telescope light curves of CoRoT-18 compared to the JKTEBOP best fits. Other comments are the same as Fig. 1.

by a 4σ clip. I modelled the light curve using numerical integration ($N_{\rm int} = 3$) and with $P_{\rm orb}$ and T_0 included as fitted parameters. LD-fixed and LD-fit/fix solutions were attempted, but LD-fitted solutions were avoided due to the modest quality of the light curve. The Monte Carlo algorithm implemented in JKTEBOP includes the application of random perturbations to the starting parameters for each simulation, in order to sample the parameter space well. I had to turn this option off as the perturbations yielded many poorly conditioned results, a situation also encountered for Kepler-4 in Paper IV (sect. 6.2). The RP errorbars were therefore adopted, as they are significantly larger than the MC errorbars. The full light curve solutions are given in Table A1.

A summary of the light curve solutions is given in Table A2 and the best fit to the CoRoT light curve is plotted in Fig. 1. The parameters found by Csizmadia et al. (2011) agree with my own to within the errorbars, although I find a solution with slightly larger i, smaller $r_{\rm A}$ and $r_{\rm b}$, and asymmetric errorbars. The physical properties of CoRoT-17 are given in Table A3 and again show good agreement with those of Csizmadia et al. (2011), except that the stellar surface gravity found in that work ($\log g = 4.40 \pm 0.10$) is incompatible with the star's mass and radius ($M_{\rm A} = 1.04 \pm 0.10\,{\rm M}_{\odot}$ and $R_{\rm A} = 1.59 \pm 0.07\,{\rm R}_{\odot}$). I provide the first measurement of the surface gravity of the planet.

CoRoT-17 would benefit from new photometric and spectroscopic observations, in order to refine its physical properties and check the spectroscopic $T_{\rm eff}$ value. The orbital ephemeris is imprecise, and will be unable to accurately predict transit midpoints by 2012 August (see Sect. 7).

5.2 CoRoT-18

The discovery of CoRoT-18 b was presented by Hébrard et al. (2011b), and contains a relatively massive planet ($M_{\rm b} = 3.27 \pm 0.17\,{\rm M}_{\rm Jup}$) orbiting an active star with a rotation period of 5.4 ± 0.4 d. Its relative faintness ($V = 15.0$) made RV measurements difficult. This was not a problem for the $K_{\rm A}$ value, which is large, but observations of the Rossiter-McLaughlin effect (Rossiter 1924; McLaughlin 1924) only constrain the orbit to be prograde and probably aligned.

The CoRoT data are all of 32 s cadence, and cover 13 consecutive transits. Of the 56 819 original datapoints, 6932 in the vicinity of a transit were retained and then phase-binned by a factor of ten to yield 694 normal points. Hébrard et al. (2011b) modelled these data after taking the unusual approach of binning them in time by a factor of 16 to be equivalent to 512 s cadence, to improve computational tractibility. They therefore substantially lower the information content of the data they analysed. By comparison, the phase-binned data I worked on have a cadence equivalent to 32.2 s. These were modelled with the assumptions of $L_3 = 2.0 \pm 0.1\,\%$ and $e = 0$ (Hébrard et al. 2011b). The MC errors were found to be larger than the RP ones, and the full solutions are in Table A4.

Hébrard et al. (2011b) also presented ground-based transit observations of CoRoT-18, from the Swiss Euler Telescope and EulerCam. This shows intriguing evidence around phase -0.008 for the passage of the planet over a starspot, but as noted by Hébrard et al. (2011b) the deviation cannot conclusively be assigned to this phenomenon. It was conservatively treated as correlated noise in my analysis. G. Hébrard (private communication) confirmed that these data were obtained through an R filter. They were modelled as with the CoRoT light curve, except that third light was not included (Table A5).

The light curve solutions are summarised in Table A6 and show that the CoRoT and Euler data agree well. The values from Hébrard et al. (2011b) differ by about 1σ, probably due to their approach to binning the data. The best fits are shown in Fig. 2.

The physical properties of CoRoT-18 are shown in Table A7 and show that I find a smaller system scale than Hébrard et al. (2011b), meaning that the masses and radii of both components are slightly smaller. Hébrard et al. (2011b) were unable to constrain the age of the star, as different age indicators were inconsistent with each other. The more precise light curve parameters derived in the current work point to a large age of roughly 10 Gyr, which disagrees with the comparatively fast rotation and strong lithium abundance indicative of an age of $<$1 Gyr. The evolutionary status of the star is therefore uncertain. I provide the first measurement of $g_{\rm b}$. The system would benefit from a better light curve, which would allow

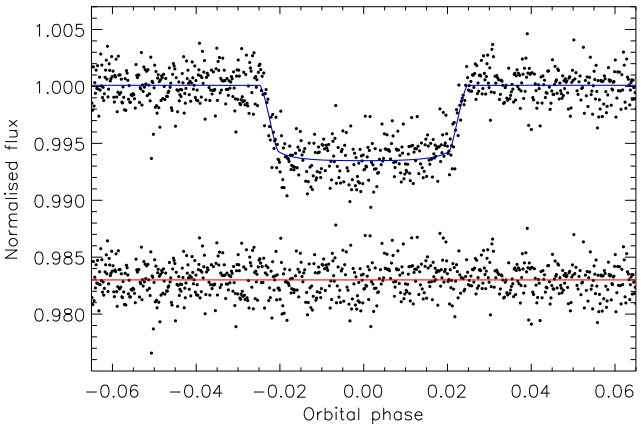

Figure 3. The CoRoT light curve of CoRoT-19 (Guenther et al. 2012) compared to the JKTEBOP best fit. Other comments are the same as Fig. 1.

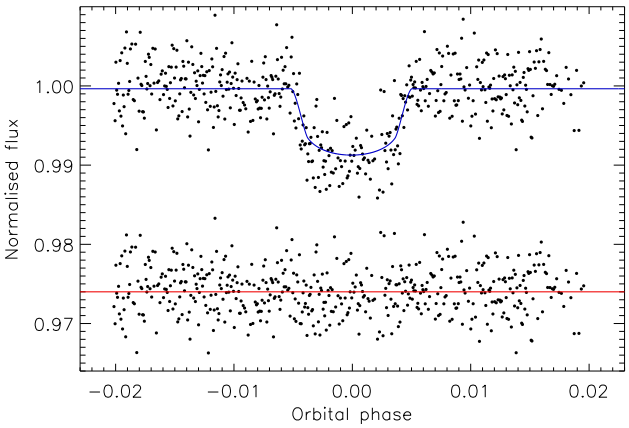

Figure 4. The CoRoT light curve of CoRoT-20 compared to the JKTEBOP best fit. Other comments are the same as Fig. 1.

refined physical properties to be obtained and also shed light on the star's age via a more precise measurement of its density.

5.3 CoRoT-19

The planetary nature of this system was discovered by Guenther et al. (2012). The CoRoT data comprise 56 837 datapoints at 32 s cadence covering seven consecutive transits, of which 9229 points near transit were binned by a factor of ten to give 924 normal points (Fig. 3). Guenther et al. (2012) constrained $L_3 < 0.32\,\%$ and $e < 0.15$ (3σ) so third light and orbital eccentricity were neglected in my analysis (Table A8). The RP errors were used, as they are modestly larger than the MC ones. From Table A9 it is clear that I find a slightly different solution to the light curve compared to Guenther et al. (2012), with much larger and asymmetric errorbars. The two solutions are compatible within my errors, but not within those of Guenther et al. (2012).

The physical properties I find for the CoRoT-19 system (Table A10) are imprecise and agree with those of Guenther et al. (2012). A discrepant solution with a young stellar age (zero-age main sequence versus ∼5 Gyr) was found when using the Y^2 models, but restricting the possible solutions to older ages yielded results which were consistent with those from the other four model sets. I provide the first measurement of $g_{\rm b}$. Further photometry and spectroscopy of CoRoT-19 are needed to refine measurements of its physical properties, including the orbital ephemeris.

5.4 CoRoT-20

As found by Deleuil et al. (2012), CoRoT-20 contains a rather massive planet ($5.06 \pm 0.34\,{\rm M_{Jup}}$) in an eccentric ($e = 0.562 \pm 0.013$) and long-period (9.24 d) orbit around a G2 V star. Third light is constrained to be less than 0.6% so was neglected in my analysis. I adopted $e\cos\omega = 0.312 \pm 0.022$ and $e\sin\omega = 0.468 \pm 0.017$ (Deleuil et al. 2012). The CoRoT data comprise 56 855 datapoints at 32 s cadence but cover only three transits. The 2479 datapoints near these transits were binned by a factor of five into 496 normal points and modelled using JKTEBOP (Table A11). The light curve is of limited quality (Fig. 4) so I obtained imprecise results. Compared to Deleuil et al. (2012) I find a solution with 1σ lower i and correspondingly larger $r_{\rm A}$ and $r_{\rm b}$, with much larger errorbars (Table A12).

A similar problem was found, when calculating the physical properties of the system, as for CoRoT-19 above. The Y^2 models gave a discrepant solution with a very young age (Table A13). This was solved in the same way, by artifically restricting the possible ages for the Y^2 models to >1 Gyr. Deleuil et al. (2012) opted for the low-age solution, which is more consistent with their different photometric parameters and with their detection of the Li 6708 Å absorption line. The discrepancy supports the much larger errorbars I find, and suggests further observations of CoRoT-20 would be valuable. I find significantly different physical properties for the planet: $M_{\rm b} = 5.06 \pm 0.36 \pm 0.04\,{\rm M_{Jup}}$ (Deleuil et al. 2012 obtained $4.24 \pm 0.23\,{\rm M_{Jup}}$), $R_{\rm b} = 1.16 \pm 0.26\,{\rm R_{Jup}}$ ($0.84 \pm 0.04\,{\rm R_{Jup}}$) and $T'_{\rm eq} = 1100 \pm 150$ K (1002 ± 24 K). I provide the first published measurement of $g_{\rm b}$.

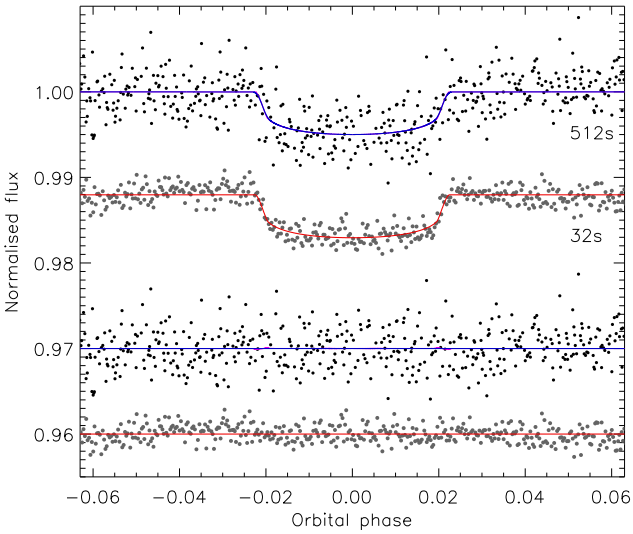

Figure 5. The CoRoT light curve of CoRoT-23 compared to the JKTEBOP best fit. Other comments are the same as Fig. 1.

5.5 CoRoT-23

CoRoT-23 (Rouan et al. 2012) contains another massive and eccentric planet ($M_{\rm b} = 3.06 \pm 0.31\,{\rm M_{Jup}}$ and $e = 0.16 \pm 0.02$), orbiting a somewhat evolved star ($\log g_{\rm A} = 4.01^{+0.08}_{-0.11}$). CoRoT observed it at 512 s cadence initially (3598 datapoints covering nine transits) and then switched to 32 s cadence (130 544 datapoints covering 15

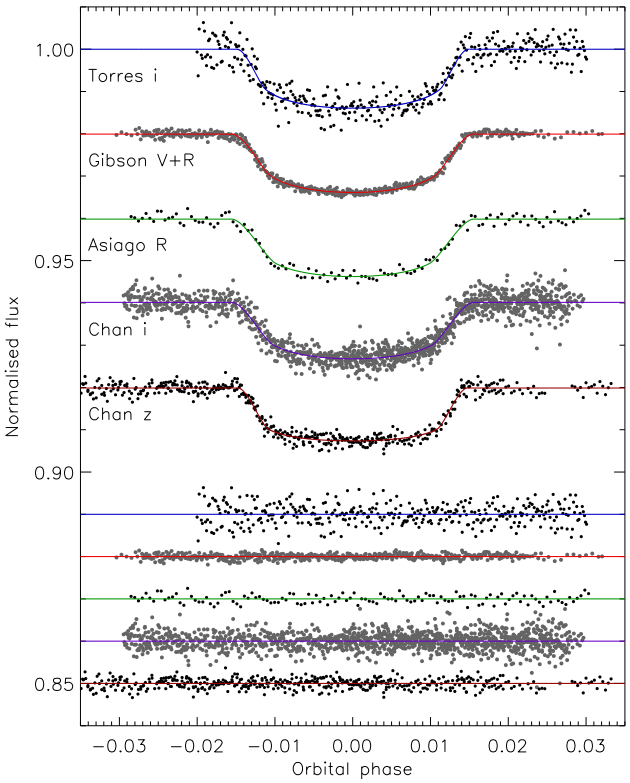

Figure 6. Light curves of HAT-P-3 compared to the best fit found using JKTEBOP and the quadratic LD law. The residuals are plotted at the base of the figure, offset from unity. The light curve sources and passbands are labelled.

transits) after it was identified as a planet candidate. The 584 datapoints at 512 s cadence in the region of transits were modelled using $N_{\rm int} = 3$. The 20 614 datapoints at 32 s cadence near transit were phased and binned by a factor of 40 to yield 516 normal points. Both sets of data were modelled adopting $e = 0.16 \pm 0.02$, $\omega = 52^\circ \pm 9^\circ$, and with $L_3 = 7.2\%$. Rouan et al. (2012) did not give an errorbar for L_3, so I used an estimate of 3%. For the 512 s data (Table A14) the RP errorbar was larger than the MC one for i, whereas for the 32 s data (Table A15) the RP errorbars were all smaller than the MC equivalents.

The light curve solutions are summarised in Table A16 and the best fits plotted in Fig. 5. Compared to Rouan et al. (2012), I find larger errorbars, and 1.5σ larger $r_{\rm A}$ and $r_{\rm b}$. The solutions to both datasets are ill-defined and have asymmetric errorbars. Despite these issues, my physical properties of CoRoT-23 are in good agreement with those of Rouan et al. (2012) both for values and errorbars (Table A17). A lower $T_{\rm eff}$ would match the photometric parameters better, and an improved light curve is important for refining these parameters plus improving the orbital ephemeris. CoRoT-23 would be an interesting system to study further, due to its evolved host star, but its faintness may be an issue ($V = 15.63 \pm 0.07$). I provide the first published measurement of $g_{\rm b}$.

5.6 HAT-P-3

Presented by Torres et al. (2007), HAT-P-3 is a fairly typical TEP system except that it is metal-rich ($\left[\frac{\rm Fe}{\rm H}\right] = 0.27 \pm 0.05$) and the planet is unexpectedly small, two qualities which may be connected. Torres et al. (2007) found that a heavy-element core of mass $\sim$75 $\mathrm{M}_\oplus$ was needed for theoretical models to match the planet's radius; Chan et al. (2011) suggested $\sim$100 $\mathrm{M}_\oplus$.

The discovery paper (Torres et al. 2007) included follow-up photometry of one transit obtained with the KeplerCam imager on the FLWO 1.2 m telescope. The dataset comprises 386 datapoints obtained in the i-band. I multiplied the errorbars of the data by $\sqrt{8.503}$ to obtain a reduced χ^2 of $\chi^2_\nu = 1.0$. The data were modelled with JKTEBOP, with the findings that the LD-fit/fix results are best, RP errors are similar to MC errors, and the errorbars are significantly asymmetric (Table A18).

Gibson et al. (2008) published an extensive analysis of HAT-P-3 based on photometry of seven transits obtained with LT/RISE, with the intention of probing for transit-timing variations (TTVs). To solve these data I phase-binned them by a factor of 40 to reduce the 19 681 original points to 493 normal points, with the rejection of 24 points by a 4σ clip, and multiplied the errorbars by $\sqrt{2.358}$ to obtain $\chi^2_\nu = 1.0$. The LD-fit/fix solutions are best, MC and RP errors are similar, and the errorbars are symmetric (Table A19).

Nascimbeni et al. (2011) obtained high-speed photometry of one transit of HAT-P-3 (exposure time 2 s, cadence 5 s) using AFOSC on the Asiago 1.8 m telescope. The 2247 original datapoints were already condensed to 122 binned points in the datafile lodged with the CDS; I modelled these after multiplying the errors by $\sqrt{1.985}$. The results (Table A20) show insignificant correlated noise and that the LD-fit/fix solutions are best.

Finally, Chan et al. (2011) observed HAT-P-3, again using KeplerCam, over three transits in the i-band and three more in the z-band. The two sets of data (1258 and 506 points respectively) were solved separately with fixed $P_{\rm orb}$. I found that the RP errors were similar to the MC ones and that the LD-fit/fix solutions are best (Tables A21 and A22). The scatter of the z-band data is around 1.3 mmag, usefully lower than the 2.2 mmag for the i-band data. The best fits to all datasets are shown in Fig. 6.

The light curve solutions are summarised in Table A23, and show a comparatively poor agreement between datasets. Ths is primarily due to the z-band data from Chan et al. (2011) but also to the data from Torres et al. (2007). The χ^2_ν of the model "the values from different light curves agree" is 1.7–2.1 for $r_{\rm A} + r_{\rm b}$, k, $r_{\rm A}$ and $r_{\rm b}$, and 1.0 for i. If the z-band data are discounted then I instead find a much better $\chi^2_\nu = 0.3$–1.0. The source of this discrepancy is not clear, so I have adopted the results ignoring the z-band data. The agreement between my final photometric parameters and those of previous studies is not great; my parameter values mostly lie in the middle of the distribution of those from previous studies. This situation is understandable in that I have included multiple datasets which are in modest disagreement, whereas previous researchers have tended to concentrate on only their own data rather than the full set of available observations.

The results from my JKTABSDIM analysis (Table A24) show good agreement with previous work, except that I find modestly larger radii for both star and planet. The larger stellar radius shifts the age of the system from 0.4–1.6 Gyr to $7.5^{+4.2}_{-3.8}$ Gyr. My new solution should be the most reliable as I have based it on all available photometry (albeit with one dataset rejected). Further photometry would be useful in helping to understand the two discrepant datasets, but HAT-P-3 is already well-characterised so such effort is better spent on other TEPs.

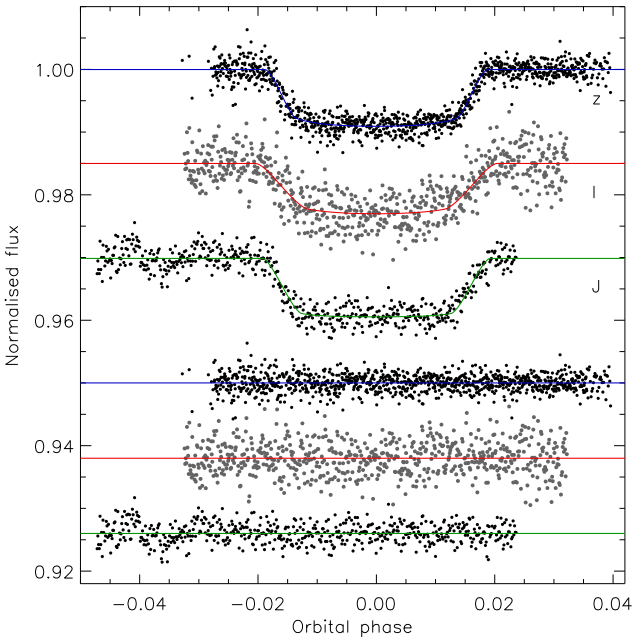

Figure 7. Light curves of HAT-P-6 compared to the JKTEBOP best fits. From top to bottom the datasets are z-band (Noyes et al. 2008), I-band (Todorov et al. 2012) and J-band (Todorov et al. 2012; Sada et al. 2012). Other comments are the same as Fig. 6.

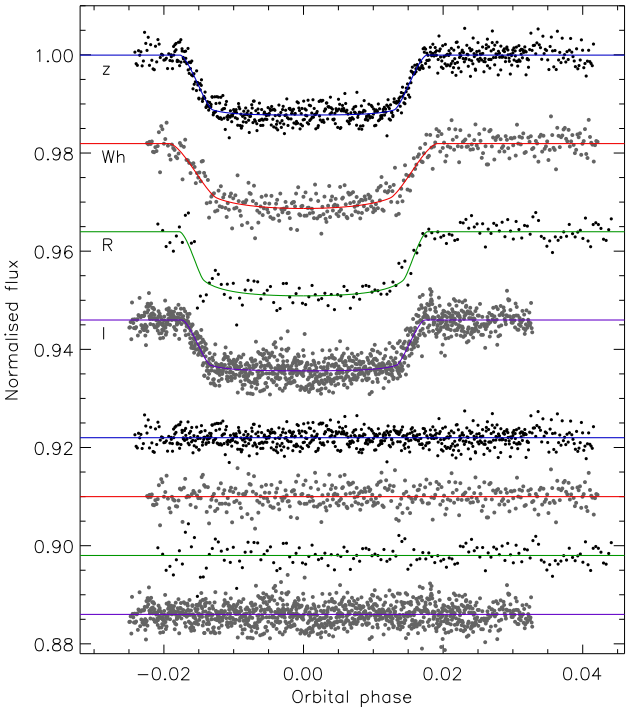

Figure 8. The light curves of HAT-P-9 compared to the JKTEBOP best fits. The top three datasets are from Shporer et al. (2009b) and the fourth is from Dittmann et al. (2012). Other comments are the same as Fig. 6.

5.7 HAT-P-6

HAT-P-6 b was discovered by Noyes et al. (2008) and is known to have a retrograde orbit from Rossiter-McLaughlin observations (Hébrard et al. 2011a), in agreement with the high $T_{\rm eff}$ of the host star. Todorov et al. (2012) have presented *Spitzer* observations of occultations at 3.6 and 4.5 μm which provide a useful constraint on the orbital shape: $e\cos\omega < 0.004$ (3σ).

Two z-band follow-up transits of HAT-P-6 were presented by Noyes et al. (2008), observed with the FLWO 1.2 m and KeplerCam on two nights separated by 312 d. I used the decorrelated version of the data, as is plotted in fig. 1b of that paper. The number of datapoints is 499 and 515, respectively, and I multiplied the errorbars by $\sqrt{3.76}$ to obtain $\chi^2_\nu = 1.0$. The results (Table A25) show that the LD-fit/fix solutions are good and that the MC errors are larger than the RP alternatives.

Aside from their *Spitzer* photometry, Todorov et al. (2012) presented two transits, one observed in the I-band using a 0.36 m telescope and one observed in the J-band using the KPNO 2.1 m telescope with FLAMINGOES infrared imager and spectrograph. The latter dataset was also presented by Sada et al. (2012), who required a fifth-order polynomial to normalise the light curve to unit flux due to the increased complications involved in infrared versus optical observations.

The i-band light curve comprises 649 datapoints which suffer from a large scatter, requiring the use of fixed LD coefficients as well as a fixed out-of-transit brightness in order to arrive at a 'reasonable' model for the data (Table A26). For this reason I did not use the results from these data when calculating the final photometric parameters.

For the 560 J-band datapoints, I multiplied the errorbars by $\sqrt{2.65}$ and calculated JKTEBOP solutions using a fifth-order polynomial flux normalisation (Table A27). The RP errors are twice as big as the MC errors, indicating that these data contain significant correlated noise (see in particular around phase -0.04 in Fig. 7. I adopted the LD-fit/fix results and RP errors. The best-fitting LD is weaker than theoretically predicted, but only by 1σ.

The z-band and J-band results show a reasonable agreement (Table A28), except for k where $\chi^2_\nu = 2.1$. This is likely due to the lower reliability of the J-band transit, and the errorbars of the final photometric parameters have been inflated accordingly. Further photometry of HAT-P-6 would be useful. Noyes et al. (2008) and Torres et al. (2008) find almost identical photometric parameters to each other, which are also in agreement with my own.

I find physical properties for the HAT-P-6 system which are in good ageement with previous work (Table A29) but indicate a sightly larger star and smaller planet. My new results are based on more extensive data than other studies of HAT-P-6 so should be the most reliable. Further improvement could be achieved by obtaining new photometry, as the light curves are the current bottleneck in our understanding of this TEP system.

5.8 HAT-P-9

The discovery of HAT-P-9 b was announced by Shporer et al. (2009b), who also obtained two follow-up transits with the FLWO 1.2 m (z-band), one with the WISE 0.46 m (unfiltered) and one with the WISE 1.0 m (R-band) telescopes. Moutou et al. (2011) measured the Rossiter-McLaughlin effect to find $\lambda = -16\pm8$, which is consistent with alignment between the orbital axis of the planet and the spin axis of the star. Dittmann et al. (2012) obtained two more transit observations in the I-band using the 1.6 m Kuiper telescope.

For the z-band data, 675 points over two transits, I fitted for $P_{\rm orb}$. The RP errors were smaller than the MC errors and full solutions are in Table A30. For the unfiltered (399 datapoints) and R-band (154) data I did not fit for $P_{\rm orb}$.

For the unfiltered data I adopted LD coefficients appropriate for the CoRoT white light curves as these are close enough for the current purposes, and found that the RP errors were slightly bigger than the MC ones (Table A31). For the R-band data I multiplied the errorbars by $\sqrt{5.45}$ to get $\chi^2_\nu = 1.0$, and found that the data prefer a central transit (Table A32) in disagreement to the other datasets for this star. The different light curve shape can clearly be seen in Fig. 8.

The two I-band transits appear to have slightly different depths (see fig. 2 in Dittmann et al. 2012) but individual solutions showed that the difference is not significant. I therefore modelled all 1144 datapoints together, with $P_{\rm orb}$ included as a fitted quantity (Table A33).

The light curve solutions are summarised in Table A34. Agreement between the three datasets (z, R, I) is poor ($\chi^2_\nu = 2.7$ for $r_{\rm A} + r_{\rm b}$, $\chi^2_\nu = 8.7$ for k) and not easily explicable. The R-band results appear to be somewhat different to the z and I ones, but rejection of these does not improve matters ($\chi^2_\nu = 13.7$ for k). I therefore calculated the final photometric parameters from the z, R and I individual results, with the errors inflated to account for the disagreement. Further photometry of HAT-P-9 is recommended to help understand this discrepancy and improve the measured system parameters. The results from Shporer et al. (2009b) agree with my values to within my errorbars, but not to within their errorbars.

The JKTABSDIM results (Table A35) show a very good agreement between the values obtained via different stellar models, and with the values found by Shporer et al. (2009b). HAT-P-9 would benefit from further photometric and spectroscopic ($T_{\rm eff}$ and $\left[\frac{\rm Fe}{\rm H}\right]$) study.

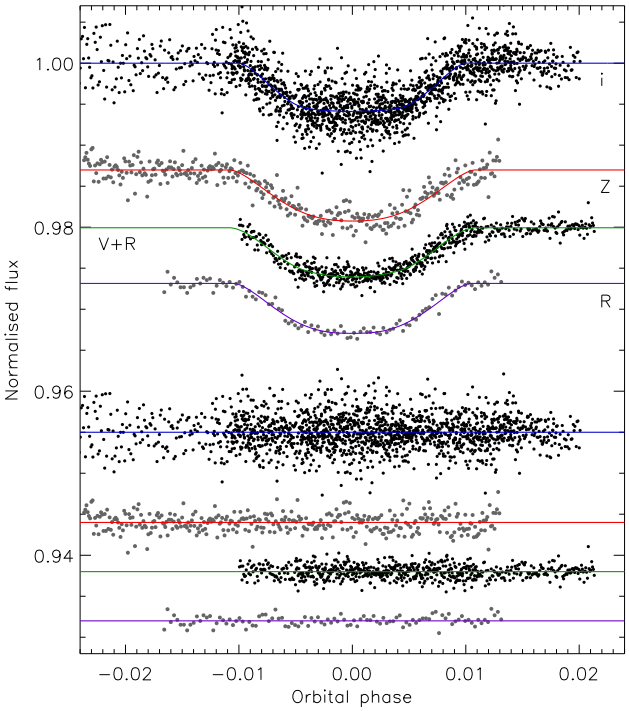

Figure 9. Light curves of HAT-P-14 compared to the JKTEBOP best fit. From top to bottom the datasets are i-band from Torres et al. (2010), FTN Z and RISE $V+R$ from (Simpson et al. 2011) and R from Nascimbeni et al. (2011). Other comments are the same as Fig. 6.

5.9 HAT-P-14

Discovered by Torres et al. (2010), the HAT-P-14 system contains a relatively massive planet ($2.27 \pm 0.08\,{\rm M_{Jup}}$). Its low orbital inclination (i.e. high impact parameter) is potentially helpful in measuring the light curve parameters to high precision, and in probing for variations in these quantities. It was independently discovered by the WASP survey (Simpson et al. 2011), from whom additional photometry and spectroscopy is available. The spectroscopic properties from the two consortia ($T_{\rm eff}$ and $\left[\frac{\rm Fe}{\rm H}\right]$) agree. One more transit light curve has been presented by Nascimbeni et al. (2011), and Winn et al. (2011) have found it to be in a retrograde orbit from observing its Rossiter-McLaughlin effect.

Both Torres et al. (2010) and Simpson et al. (2011) find a significant orbital eccentricity. This is expected given the correlation between the presence of a relatively massive planet and an eccentric orbit (Southworth et al. 2009c). I adopted $e = 0.107 \pm 0.013$ and $\omega = 94^\circ \pm 4^\circ$ (Torres et al. 2010; Winn et al. 2011; Pont et al. 2011) in the analysis below. Due to the limited quality of individual light curves I did not attempt LD-fitted solutions.

Torres et al. (2010) presented i-band observations of five transits using the FLWO 1.2 m, for which I multiplied the errorbars by $\sqrt{9.82}$ to get $\chi^2_\nu = 1.0$. The full solutions are in Table A36 and the MC errors are larger than the RP ones.

The work by Simpson et al. (2011) includes two $V+R$ band transits obtained using LT/RISE, of which one is only patially covered, and one Z-band transit using FTN/Spectral. I put the former onto a common flux zeropoint and multiplied the errorbars by $\sqrt{5.15}$ before the JKTEBOP analysis. For both datasets (Table A37 and Table A38), the LD-fit/fix solutions returned unphysical LD coefficients so I adopted the LD-fixed results. The RP errors are significantly larger than the MC errors, showing that correlated noise is important for both datasets.

The data of Nascimbeni et al. (2011) were originally 2247 datapoints but the file deposited at the CDS is binned to 109 normal points. Solutions of these data (Table A39) once more yielded unphysical LD coefficients so the LD-fixed solutions had to be adopted.

A summary of the light curve solutions can be found in Table A40 and a plot of the best fits in Fig. 9. Agreement between the four light curves is within the uncertainties for $r_{\rm A} + r_{\rm b}$, i and $r_{\rm A}$, and slightly greater than the uncertainties for k and $r_{\rm b}$. Literature value agree with my own, but the errorbars are in some cases too small. This situation persists for the physical properties of the system (Table A41). More photometry and RV measurements would be useful, especially in reducing the reliance on theoretical LD coefficients, but HAT-P-14 is a well-understood system.

5.10 Kepler-7

Kepler-7 contains a low-density TEP ($0.094 \pm 0.009\,\rho_{\rm Jup}$) and a slightly evolved star ($\log g = 3.97 \pm 0.02$). The discovery paper (Latham et al. 2010) presented an analysis of the *Kepler* Q0 and Q1 data. The studies of Kipping & Bakos (2011) and Paper IV had access also to the Q2 data, although none of the three datasets were short-cadence. Demory et al. (2011) presented a study of the Q0-Q4 data, of which Q3 and Q4 are short-cadence, and found the planet to have a high albedo from consideration of the occultation visible in the *Kepler* data. Their analysis included asteroseismological constraints, which are not used here in order to avoid inhomogeneity.

In the current work I have analysed the Q3 data, which are

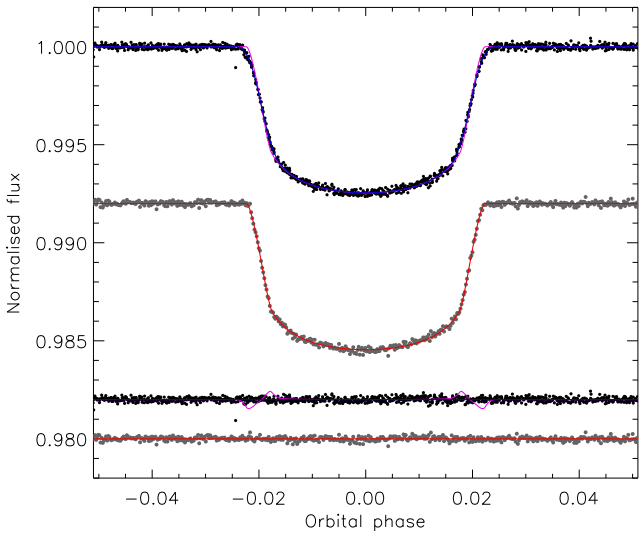

Figure 10. The *Kepler* light curves of Kepler-7 compared to the JKTEBOP best fits. The top light curve is the Q0-Q3 long-cadence data and the bottom one is the Q3 short-cadence data. Other comments are the same as Fig. 1.

the only short-cadence data publicly available for Kepler-7. The improved time sampling of these data means that my results are better than those from Paper IV, which were based on long-cadence data. A third light value of $L_3 = 1.4\%$ is listed in the Kepler Input Catalogue (KIC; Brown et al. 2011), but without uncertainties. I therefore adopted an uncertainty of 0.5%.

A new orbital ephemeris was derived from the Q0-Q3 long-cadence data, fitting only those data near one of the 42 transits and using $N_{\rm int} = 10$. This yielded:

$$T_0 = \mathrm{BJD(TDB)}\ 2\,455\,074.756840(53) + 4.8854922(38) \times E$$

where the reference time of minimum has been carefully chosen to be near the midpoint of the data interval, thus minimising its covariance with the orbital period. E represents an integer cycle count, and the bracketed quantities give the uncertainty in the last digit of the preceding number. Errorbars were calculated using MC and RP simulations and the larger of the two options is quoted. The two sets of errorbars were very similar, and also close to the formal errors calculated by JKTEBOP from the covariance matrix of the best-fitting solution.

The Q3 data comprise 125 082 datapoints covering 17 full transits. One transit had a brightening feature affecting six datapoints around time BJD(TDB) 55133.35 which could indicate a stellar flare or instrumental artefact, so the data for this transit were ignored. 16 897 datapoints around the remaining transits were phase-binned by a factor of 25 to give 676 normal points. These data were modelled using JKTEBOP (Table A42). The LD-fitted solutions are good enough to be adopted, and the RP errors are smaller than the MC ones (as usual for phase-binned data).

The light curve solutions are summarised in Table A43 and the best fit to the data is plotted in Fig. 10. The new results from the Q3 short-cadence data are in excellent agreement with those from Paper IV but are more precise. I combined the two to get the final photometric parameters. The values found by Kipping & Bakos (2011) are in agreement with my new results, whereas the ones from Latham et al. (2010) are in marginal disagreement.

When determining the physical properties of Kepler-7 I found that the results using the different stellar models are in comparatively poor agreement (Table A44), as often happens when the host star is evolved. My final results give a more massive star and planet than previously found, but within the errorbars. *Kepler* continues to observe this system, so even better results will available in the future.

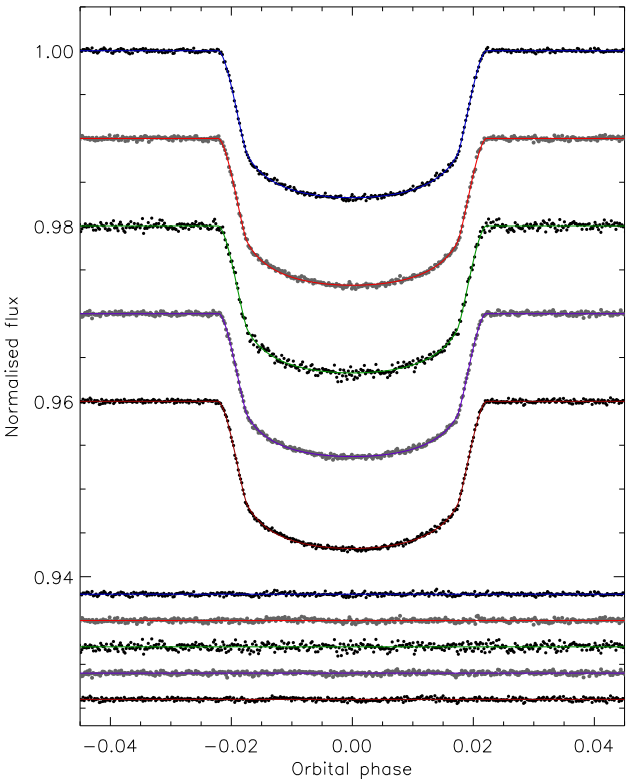

Figure 11. The *Kepler* light curves of Kepler-12 compared to the JKTEBOP best fits. From top to bottom are the phase-binned short-cadence light curves from Q2 to Q6. Other comments are the same as Fig. 6.

5.11 Kepler-12

Discovered by Fortney et al. (2011), the Kepler-12 system contains the second-least-dense planet after WASP-17 (Anderson et al. 2010, 2011; Southworth et al. 2012b) and ahead of Kepler-7 (see above). Fortney et al. (2011) obtained the constraint $e < 0.09$ at the 3σ level. Data from Q0 to Q6 are publicly available, but the Q0 and Q1 data are only long-cadence so I did not consider them further. Q4 is split into three periods, of which the Q4.1 data are available but the Q4.2 and Q4.3 data are not.

I analysed the Q2 to Q6 data, all of which are short-cadence, using the season-dependent third light values given in the KIC and assuming an uncertainty of 0.5%. The data from different quarters had to be analysed separately in order to be able to assign the appropriate third light values. In each case the transits were extracted from the full data, normalised to unit flux, and then phase-binned by a factor of 25 (a factor of seven for Q4 as it contains three times fewer datapoints). The solutions are given in Tables A45 to A49. In each case the MC and RP errors are similar. The light curve solutions are summarised in Table A50 and the best fits are plotted in Fig. 11. The five sets of solutions agree well with each other, and the combined results also agree well with those of Fortney et al. (2011).

The resulting physical properties (Table A51) are also in very good agreement with those of Fortney et al. (2011). Whilst *Kepler*

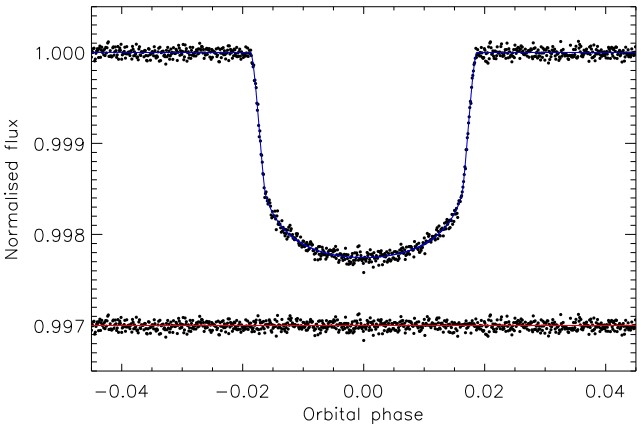

Figure 12. The *Kepler* Q3-Q6 short-cadence light curve of Kepler-14 compared to the JKTEBOP best fit. Other comments are the same as Fig. 6.

continues to observe this system, the precision of its physical properties is limited by the spectroscopic properties of the host star and by imperfect interpolation within tabulated predictions from theoretical stellar models.

5.12 Kepler-14

Discovered by Buchhave et al. (2011), the system holds a massive ($7.7 \pm 0.4\,\mathrm{M_{Jup}}$) hot Jupiter orbiting a comparatively hot star ($T_{\rm eff} = 6395 \pm 60$ K). The *Kepler* light curve is strongly contaminated by the light from a similarly bright star within $0.29''$ of system. Buchhave et al. (2011) measured a magnitude difference in the *Kepler* passband of $\Delta m_{\rm Kp} = 0.44 \pm 0.10$, and corrected both the light curves and RVs for this contamination. Given the very low contamination levels from KIC (0.007–0.010 for the four *Kepler* seasons) it seems that the only relevant third light comes from the very close star. Its closeness means that the data from different seasons will be affected in the same way, so it is reasonable to adopt $L_3 = 0.333 \pm 0.062$ when fitting all the *Kepler* data.

Kepler observed Kepler-14 in long cadence in Q0-Q6, and in short cadence in Q3-Q6. Buchhave et al. (2011) opted to use the full set of long-cadence data only, for homogeneity and simplicity and because the transit is relatively long (L. Buchhave, private communication). Results based on short-cadence data stand a good chance of providing improved results due to their much better time resolution. I have therefore modelled the Q3 to Q6 short-cadence data.

These data comprise a total of 507 006 datapoints covering 50 complete transits. 58 161 of these datapoints are close to transits, and I phase-binned them by a factor of 50 to get 1164 normal points. I adopted $e\cos\omega = 0.0006 \pm 0.0099$ and $e\sin\omega = 0.0350 \pm 0.0170$ (Buchhave et al. 2011), whch suggests that eccentricity is significant at the 2σ level. The RP errorbars were smaller than the MC ones, and I was able to adopt LD-fitted solutions (Table A52).

Given the extremely high quality of the light curve I tried fitting for L_3 directly. Investigations of this possibility in Paper III showed that third light is almost completely degenerate with other photometric parameters ($r_{\rm A}$, $r_{\rm b}$ and i), so may not be obtainable even from exceptionally good data. I obtained $L_3 = 0.223 \pm 0.085$ which is within 1σ of the expected value but still poorer than using outside constraints. I also checked whether it was possible to fit for $e\cos\omega$ and/or $e\sin\omega$, and confirmed the result of Kipping (2008) that such parameters cannot be extracted. The best-fitting values were $e\cos\omega = 0.350 \pm 0.065$ and $e\sin\omega = 0.149 \pm 0.019$, which are inconsistent with the known results determined by Buchhave et al. (2011) from RVs and a *Spitzer* occultation.

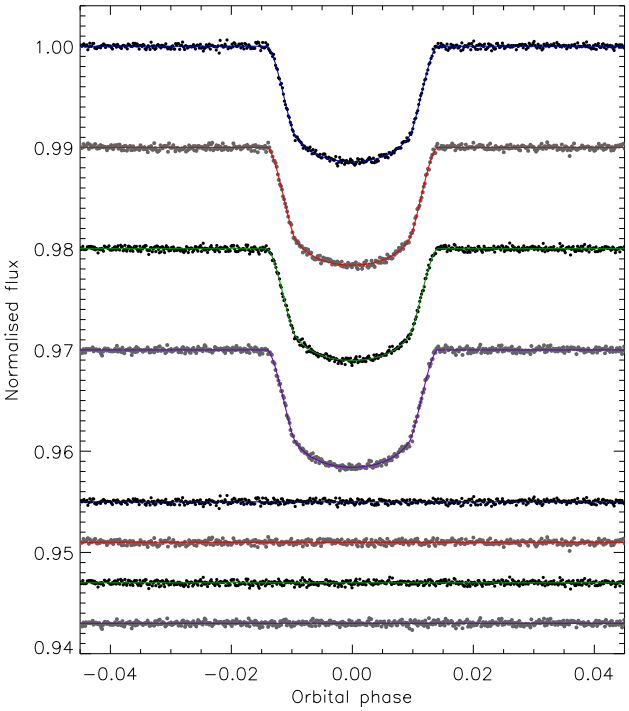

Figure 13. The *Kepler* Q3 to Q6 short-cadence light curves of Kepler-15 compared to the JKTEBOP best fits. Other comments are the same as Fig. 6.

A summary of the light curve solutions is given in Table A53 and the best fit is plotted in Fig. 12. I find somewhat different photometric parameters from those of Buchhave et al. (2011), which is likely down to the use of short-cadence data in the current work. The third light has a strong effect on the results, as the photometric parameters are all strongly correlated with it. It thus sets a limit on the quality of the solution, so improved measurements of L_3 would be the best way to improve our understanding of the system.

I find a rather different set of physical properties for Kepler-14 (Table A54), with a less massive but more evolved star. Compared to Buchhave et al. (2011) I find a stellar mass of $M_{\rm A} = 1.318 \pm 0.052 \pm 0.029\,\mathrm{M_\odot}$ rather than $1.512 \pm 0.043\,\mathrm{M_\odot}$ (a change of 2.6σ), a very similar stellar radius and a 1.4σ different surface gravity ($\log g_{\rm A} = 3.918 \pm 0.040 \pm 0.003$ versus $3.994^{+0.028}_{-0.036}$). The $\log g_{\rm A}$ derived from spectral analysis is 4.11 ± 0.10 (Buchhave et al. 2011). These changes propagate to the planet, which is found to be less massive but the same size as before. *Kepler* will provide further photometry to help investigate this system, but obtaining revised $T_{\rm eff}$, $\left[\frac{\rm Fe}{\rm H}\right]$ and L_3 values would be the best way to improving our understanding of the Kepler-14 system.

5.13 Kepler-15

Endl et al. (2011) presented the discovery of this planetary system containing a comparatively low-mass ($0.70 \pm 0.10\,\mathrm{M_{Jup}}$) planet around a cool ($5595 \pm 120$ K) star. Endl et al. (2011) used the *Kepler* long-cadence photometry from quarters Q1 to Q6 plus RVs from two telescopes to characterise the system. However, *Kepler* short-cadence data are also available for quarters Q3 to Q6, and their

much greater time resolution should yield better results than for the long-cadence data.

The *Kepler* Q3 to Q6 short-cadence data were modelled individually quarter-by-quarter, using the third light values from the KIC and adopting an uncertainty of 0.5% in these values. Eccentricity was not found to be significant by Endl et al. (2011) so I assumed $e = 0$. Each dataset was phase-binned by a factor of 20, giving 613, 563, 685 and 644 normal points respectively. The full solutions are in Tables A55 to A58 and the best fits are shown in Fig. 13.

Table A59 summarises the light curve solutions, and shows that their interagreement is good (except for k where $\chi^2_\nu = 1.8$). The final photometric parameters are extremely precise. However, their ageement with the findings of Endl et al. (2011) is very poor: differences of 24σ occur for $r_{\rm A}$ and i, 7σ for k and 33σ for $r_{\rm b}$. It is unclear how such a large discrepancy could arise, although one possibility to investigate would be the use of long-cadence versus short-cadence data. I was unable to reproduce the results of Endl et al. (2011) by fitting the long-cadence data either with or without numerical integration. My new results should be preferred because the short-cadence data are much better for measuring planet parameters than the long-cadence data (see Paper IV).

As would be expected from the rather different photometric parameters, my calculated physical properties (Table A60) are at odds with those of Endl et al. (2011). The most obvious changes are for the radii of the two components, which go from $R_{\rm A} = 0.992^{+0.058}_{-0.070}\,{\rm R}_\odot$ and $R_{\rm b} = 0.96^{+0.06}_{-0.07}\,{\rm R}_{\rm Jup}$ (Endl et al. 2011) to $R_{\rm A} = 1.253 \pm 0.047 \pm 0.020\,{\rm R}_\odot$ and $R_{\rm b} = 1.289 \pm 0.050 \pm 0.021\,{\rm R}_{\rm Jup}$ (this work). The $\log g_{\rm A}$ I find is in better agreement with the spectroscopic measurement, albeit at low significance. My revisions to the physical properties of the Kepler-15 system decrease the planet's measured density by more than a factor of 2, increase the measured age of the star, and include the first measurement of $g_{\rm b}$, $T'_{\rm eq}$ and Θ.

5.14 Kepler-17

Kepler-17 comprises a hot and massive planet ($T'_{\rm eq} = 1712 \pm 25$ K, $M_{\rm b} = 2.34^{+0.09}_{-0.24}\,{\rm M}_{\rm Jup}$) orbiting an active star. Starspot activity is obvious both in the overall light curve and by spot crossings during the planetary transits, allowing a measurement of the star's rotation period in the discovery paper (Désert et al. 2011). The rotation period is close to eight times $P_{\rm orb}$, giving a 'stroboscopic' effect whereby some starspots can be identified each eighth transit. This also allows the orbital obliquity to be constrained to be less than 15° (Désert et al. 2011). *Spitzer* observations of an occultation allowed limits to be placed on orbital shape $e < 0.011$ in combination with the *Kepler* photometry and RV observations. An independent discovery of the Kepler-17 system was made by Bonomo et al. (2012), who combined their RVs with those of Désert et al. (2011) to obtain a more precise $K_{\rm A}$. Their other result were in good agreement with those from the discovery paper, but less precise as they only had *Kepler* Q1-Q2 data versus the Q1-Q6 available to Désert et al. (2011).

As before (see HAT-P-11 in Paper IV) I have assumed that the starspot activity under the transit chord is on average the same as that for the rest of the stellar photosphere. This means that the data affected by starspots do not require special treatment, and the effect of the starspot crossings on the solution will simply be to inflate the errorbars as an additional source of correlated noise. This in turn is partially coverted into white noise when the data are phase-binned,

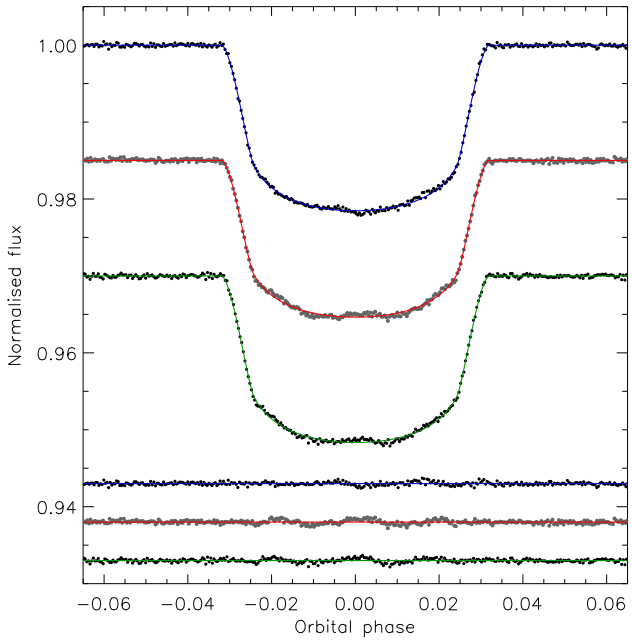

Figure 14. The *Kepler* Q4-Q6 short-cadence light curves of Kepler-17 compared to the JKTEBOP best fits. Other comments are the same as in Fig. 6.

and will ultimately cause larger errorbars to be found than if the star were quiet.

The *Kepler* Q4 to Q6 data are available in short-cadence flavour, and these were phase-binned as usual to yield 621, 634 and 621 normal points, respectively. A significant fraction (∼15%) of transits were normalised using a quadratic function instead of a straight line, in order to cope with the modulation due to starspot activity. 120 datapoints were rejected from the Q5 data by a 4σ clip, due to an unusually large number of scattered observations, whereas the numbers rejected from Q4 and Q6 data were 3 and 11 respectively.

Third light was tackled by adopting the season-dependent contamination values from the KIC and assigning an uncertainty of 0.5% to each one. The orbit was assumed to be circular. The full sets of light curve solutions are given in Tables A61 to A63 and in each case the RP errors were found to be moderately larger than the MC ones, due to the starspots on the stellar surface. The best fits are plotted in Fig. 14, where the influence of spot activity can be seen in the residuals of the best fit. The light curve solutions are summarised in Table A64, and are in good agreement, except for k where $\chi^2_\nu = 5.8$. This is due both to starspot activity and the need to use quadratic functions to normalise some transits, and has been accounted for in the errorbars. It is not sufficient to cause a disagreements in $r_{\rm A}$ or $r_{\rm b}$.

The light curve solution I find is close to a central transit ($i = 89.73^{+0.27}_{-0.94}$ deg) whereas Désert et al. (2011) prefer a lower-inclination solution ($i = 87.2 \pm 0.15$ deg) which differs by 2.6σ from my own. This affects $r_{\rm A}$ (which is 3.9σ larger according to Désert et al.) and k (3.9σ smaller). The source of this divergence is unclear. Bonomo et al. (2012) had access to only a little of the *Kepler* data, so adopted the photometric parameters from Désert et al. (2011) rather than calculate their own. Given the discrepancies, the larger errorbars found in the present study should be preferred to those given in the literature.

When calculating the physical properties of the Kepler-17 system I found slight disagreements within results using the five sets of

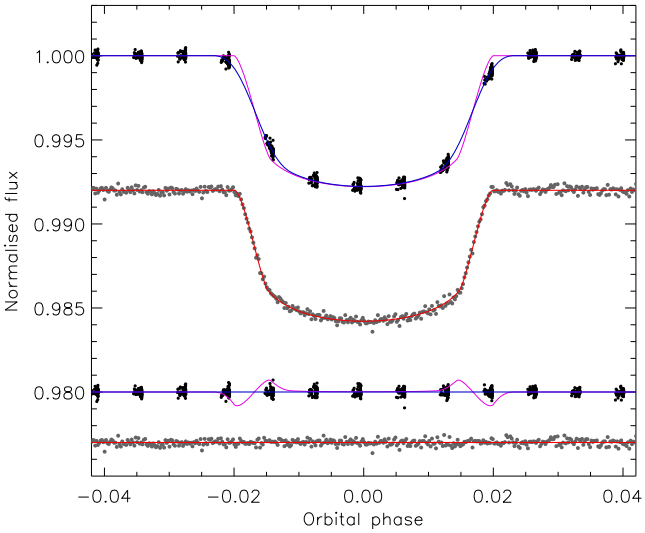

Figure 15. The *Kepler* light curves of KOI-135 compared to the JKTEBOP best fits. The upper dataset is the Q1-Q3 long cadence data and the lower dataset is the Q3 short cadence data. Other comments are the same as Fig. 1.

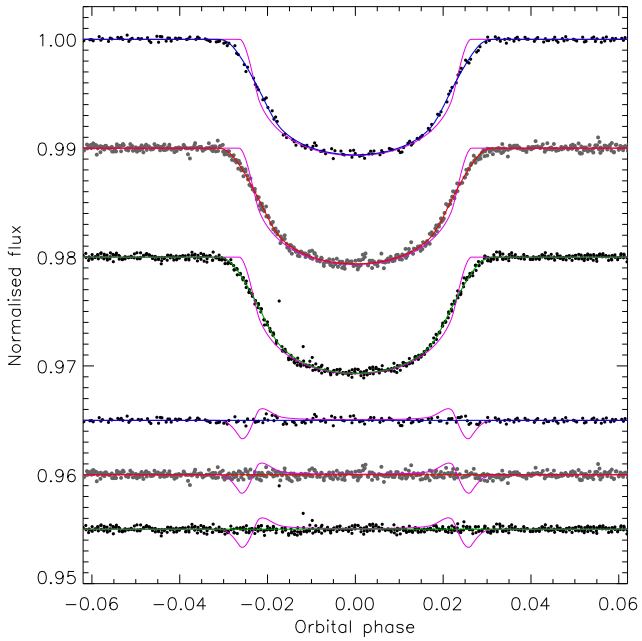

Figure 16. The *Kepler* light curves of KOI-196 compared to the JKTEBOP best fits. From top to bottom the three datasets come from the Q1, Q2 and Q3 time period. Other comments are the same as Fig. 1.

stellar models, which leads to a significant systematic component in the errorbars of the final system parameters. The values themselves are in reasonable agreement with previous studies (Table A65). As *Kepler* continues to gather photometry of this system, the action with the most benefit would be the procurement of improved spectroscopy for $T_{\rm eff}$, $\left[\frac{\rm Fe}{\rm H}\right]$ and RV measurements.

5.15 KOI-135

KOI-135 was discovered by Bonomo et al. (2012) to contain a massive planet ($3.09 \pm 0.21\,{\rm M_{Jup}}$). Bonomo et al. (2012) had access to only the Q1 and Q2 long-cadence data. One of the problems they faced is that the *Kepler* long-cadence sampling rate is close to an integer multiple of the $P_{\rm orb}$ of KOI-135, leading to very poor sampling of the shape of the transit (see Fig. 15). Q3 short-cadence data have now been released, which should allow the current work to produce a significant improvement in the measured system parameters.

Bonomo et al. (2012) found that their spectroscopic measurement of $\log g_{\rm A}$ disagreed with that obtained from analysis of the transits by 2.7σ. They found that using the transit-derived $\log g_{\rm A}$ resulted in an insignificantly different measurement of $T_{\rm eff}$ from their spectra.

My first action was to obtain an improved orbital ephemeris using the Q1 to Q3 data. This was done in the same way as for Kepler-7 in Sect. 5.10, resulting in:

$$T_0 = {\rm BJD(TDB)}\ 2\,455\,068.235237(54) + 3.0240933(27) \times E$$

The precision of this $P_{\rm orb}$ is a factor of ten better than that based on only Q1 and Q2 data (Bonomo et al. 2012).

Constraints on third light were obtained from the KIC as above, and errors of 0.5% specified. A circular orbit was adopted as Bonomo et al. (2012) found $e < 0.025$ (significance level not stated). Only the short-cadence (Q3) data were modelled, for the reasons given above. The original 125 140 datapoints were slimmed down to 18 938 close to any of the 27 transits observed by *Kepler*, 13 were rejected by a 4σ clip, and the remainder were phase-binned by a factor of 25 to get 759 normal points. Table A66 shows that the LD-fitted solutions can be used. The RP errors were smaller than the MC errors. The Q3 data yield a 3σ smaller $r_{\rm A}$ and $r_{\rm b}$ than found by Bonomo et al. (2012), so the availability of improved photometry has resulted in the modification of the measured system properties (Table A67).

Despite the large uncertainties in $T_{\rm eff}$ (143 K) and $\left[\frac{\rm Fe}{\rm H}\right]$ (0.11 dex), I found highly consistent physical properties for the KOI-135 system using different sets of stellar models (Table A68). Both the star and planet are slightly smaller than found by Bonomo et al. (2012), but these changes are within the errorbars. Forthcoming *Kepler* photometry and further spectroscopic measurements of $T_{\rm eff}$ and $\left[\frac{\rm Fe}{\rm H}\right]$ would be very helpful in refining the system properties.

5.16 KOI-196

Santerne et al. (2011a) discovered the planetary nature of this system, based on Q1-Q2 data from the *Kepler* satellite and RVs from the SOPHIE spectrograph. Santerne et al. also detected occultations in the *Kepler* data, of a depth which suggest the planet has a high albedo and at an orbital phase which is consistent with a circular orbit. Since this study the Q3 data have become available, but like Q1 and Q2 are only long-cadence.

Third light was estimated from the KIC, 0.5% errors assigned, and a circular orbit assumed. An improved orbital ephemeris was obtained from the Q1-Q3 data using the method in Sect. 5.10:

$$T_0 = {\rm BJD(TDB)}\ 2\,455\,066.669310(48) + 1.8555588(15) \times E$$

For the Q1 data, 257 of the 1625 datapoints are in the region of one of the 18 transits. For Q2 these numbers are 4802, 648 and 45, and for Q3 they are 4145, 662 and 46. The data were not binned or phased, and $N_{\rm int} = 10$ was used in the modelling process. Two families of solutions were found: one with a nearly central transit ($i \approx 90^\circ$) and one with $i \approx 80$–82°. The $i \approx 80$–82° family occurs mainly for the LD-fixed light curve solutions, and results

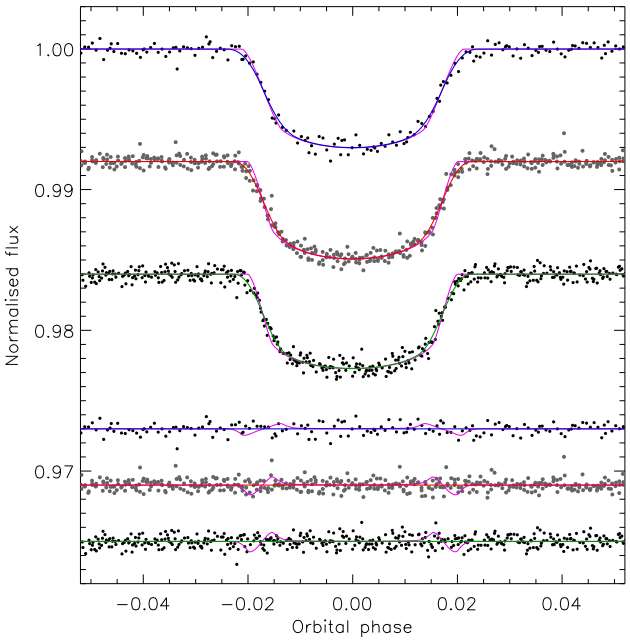

Figure 17. The *Kepler* Q1, Q2 and Q3 long-cadence light curves of KOI-204 compared to the JKTEBOP best fits. Other comments are the same as Fig. 1.

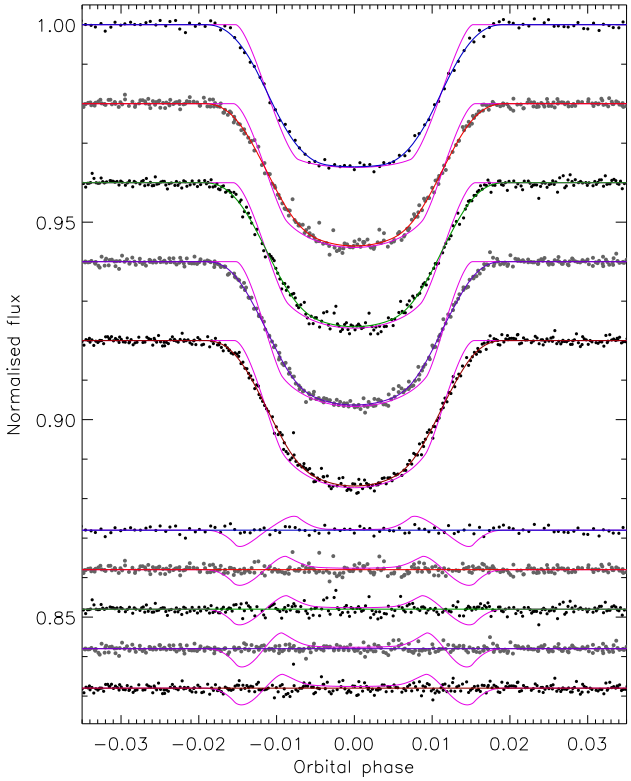

Figure 18. The *Kepler* Q1 to Q5 light curves (from top to bottom) of KOI-254 compared to the JKTEBOP best fits. Other comments are the same as Fig. 1.

in weird physical properties. In contrast, the LD-fit/fix solutions universally have $i \approx 90^\circ$ and lead to reasonable physical properties. This implies that fixing LD coefficients can have a deleterious effect on a light curve solution, specifically when working with long-cadence data. I adopted the LD-fit/fix solutions (Tables A69 to A71), in agreement with Santerne et al. (2011a), and found that the RP errors are of similar size to the MC errors.

The photometric parameters are given in Table A72 and the best fits are plotted in Fig. 16. The interagreement between the Q1-Q3 data is excellent, but further photometry (preferably short-cadence) is needed to obtain a definitive solution. Santerne et al. (2011a) found similar but slightly discrepant photometric parameters, based on fewer data.

As with KOI-135, I found highly consistent physical properties for the KOI-135 system from different sets of stellar models (Table A73) despite the large uncertainties in $T_{\rm eff}$ (100 K) and $\left[\frac{\rm Fe}{\rm H}\right]$ (0.11 dex). Compared to Santerne et al. (2011a), I deduced a slightly smaller and less massive star and planet. Further spectroscopy and forthcoming *Kepler* photometry would allow a useful improvement in measurements of the physical properties of KOI-196.

5.17 KOI-204

KOI-204 b was discovered by Bonomo et al. (2012) as part of a program to observe the brighter *Kepler* TEP candidate systems with SOPHIE. Bonomo et al. (2012) had access to *Kepler* Q1 and Q2 data, and Q3 data are now available. I derived an improved orbital ephemeris using these data and the method in Sect. 5.10, finding

$$T_0 = \mathrm{BJD(TDB)}\ 2\,455\,067.02680(15) + 3.2467220(73) \times E$$

The orbit was assumed to be circular (Bonomo et al. found $e < 0.021$) and third light values were obtained from the KIC. These are a little larger than usual, being 0.060, 0.093, 0.154 and 0.044, in seasons 0 to 3 respectively. The individual quarters of data were then fitted using $N_{\rm int} = 10$, and the full solutions are given in Tables A74 to A76. The RP errors are smaller than those from the MC algorithm. The best fits are plotted in Fig. 17.

Table A77 gives the final photometric parameters. The three datasets agree well except for k ($\chi^2_\nu = 1.9$), which is likely a symptom of spot crossings duing the transit. These are not visible to the eye, due to the poor time resolution of the long-cadence data. The values from Bonomo et al. (2012) are concordant with my own, but their errorbars are smaller despite being based on significantly less data. The same comments apply to the physical properties determined and gathered in Table A78. More observations of all types are needed to characterise this planetary system well.

5.18 KOI-254

Johnson et al. (2012) discovered this planetary system from RV follow-up of *Kepler* KOI objects (Borucki et al. 2011) classified as M dwarfs, in order to probe this host star mass regime. The stellar component is on the border of the M spectral class ($M_{\rm A} = 0.57 \pm 0.06\,{\rm M}_\odot$ and $T_{\rm eff} = 3820 \pm 90$ K), and the planet is the largest one found around a sub-4000 K star ($R_{\rm b} = 1.00 \pm 0.07\,{\rm R}_{\rm Jup}$) by some distance (the next is GJ 436 b at $0.37 \pm 0.02\,{\rm R}_{\rm Jup}$). KOI-254 is therefore an interesting object in delineating the minimum stellar mass required to host a Jupiter-sized object. Johnson et al. (2012) analysed the *Kepler* Q1 and Q2 data, which shows clear spot activity, plus a Z-band transit light curve obtained using the 1 m Nickel telescope at Lick Observatory.

At the time of writing, *Kepler* Q1 to Q5 data were available, all at long cadence. A refined orbital ephemeris was calculated as

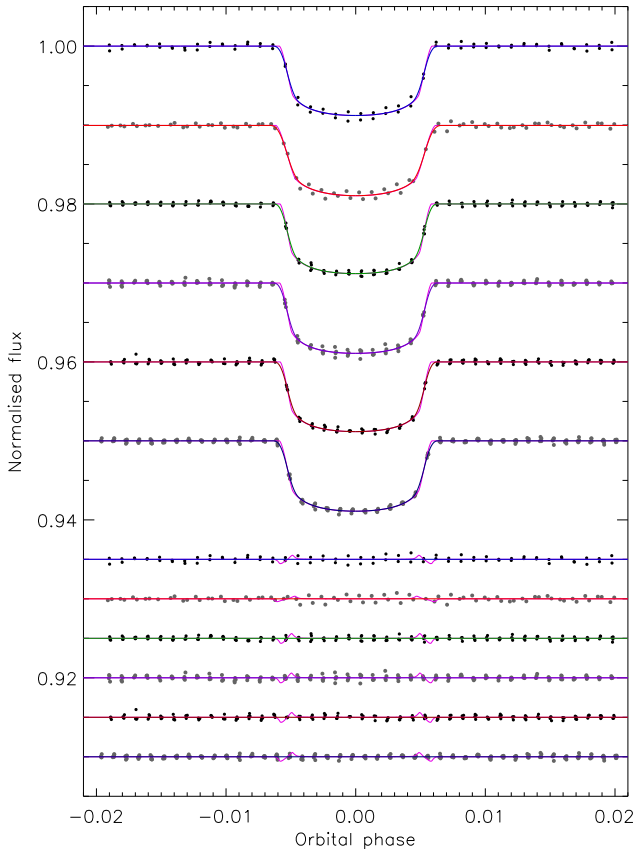

Figure 19. The *Kepler* Q1 (top) to Q6 (bottom) light curves of KOI-423 compared to the JKTEBOP best fits. Other comments are the same as Fig. 1.

in Sect. 5.10:

$$T_0 = \mathrm{BJD(TDB)}\ 2\,455\,160.956396(31) + 2.45524122(65) \times E$$

which is a factor of ten more precise than the ephemeris based on only the Q1 and Q2 data.

The data from each quarter were modelled assuming an eccentric orbit with $e = 0.11^{+0.1}_{-0.09}$ and $\omega = 230^\circ \pm 68^\circ$ (Johnson et al. 2012), third light values from the KIC with uncertainties assumed to be 0.5%, and $N_{\rm int} = 10$ (Tables A79 to A83). Table A84 shows the agreement to be very good both between the five datasets and with the values from Johnson et al. (2012). The RP errors were all smaller than the MC errors. The best fits are shown in Fig. 18.

Precise physical properties become difficult to obtain into the M-dwarf regime, as the interagreement between stellar models deteriorates, but KOI-254 is thankfully not strongly affected. The physical properties I find (Table A85) agree well with those of Johnson et al. (2012), but the availability of additional data allows the errorbars to be beaten down. *Kepler* will deliver further photometry, but more spectroscopy would be useful in nailing down the $T_{\rm eff}$, $\left[\frac{\rm Fe}{\rm H}\right]$ and spectrosocpic orbit of the host star. A significant source of uncertainty in the current results stems from the measurement of e and ω, which is rather imprecise due to the small RV signal exhibited by the star.

5.19 KOI-423

KOI-423 contains an object of brown-dwarf mass ($M_{\rm b} = 17.9 \pm 1.8$) in a long-period (21.1 d) eccentric orbit ($e = 0.121^{+0.022}_{-0.023}$) around a hot and metal-poor ($T_{\rm eff} = 6260 \pm 140$ K and $\left[\frac{\rm Fe}{\rm H}\right] = -0.29 \pm 0.10$) star (Bouchy et al. 2011). Its mass, however, places it firmly in the planetary rather than the stellar population according to Grether & Lineweaver (2006). Bouchy et al. (2011) based their analysis on RVs from the SOPHIE spectrograph, and the *Kepler* Q1 and Q2 data (which encompass only five transits between them).

The Q3 to Q6 data are also now public; all six datasets are not only long-cadence but also sample the transit shape poorly (Fig. 19). A revised orbital ephemeris was first procured using the method in Sect. 5.10:

$$T_0 = \mathrm{BJD(TDB)}\ 2\,455\,204.55515(14) + 21.087168(21) \times E$$

Each dataset was solved with numerical integration ($N_{\rm int} = 10$), constraints on L_3 from the KIC, and adopting $e\cos\omega = 0.120^{+0.022}_{-0.024}$ and $e\sin\omega = -0.019^{+0.015}_{-0.012}$ (Bouchy et al. 2011). A quadratic or cubic function was needed to normalise the majority of the transits to unit flux. MC errors were larger than RP errors, and full solutions (except for LD-fitted) can be found in Tables A86 to A91. The total dataset covers 22 transits, of which one had to be rejected due to normalisation problems caused by missing data, which is a significant improvement on the five available to Bouchy et al. (2011).

Table A92 shows that the six different light curves agree well. The combined solution has a somewhat larger i, $r_{\rm A}$ and $r_{\rm b}$, but these are within 1–2σ of those found by Bouchy et al. (2011). The physical properties of KOI-423 (Table A93) are tolerably well defined, and are reasonably close to the values found by Bouchy et al. (2011). *Kepler* short-cadence data would be valuable for this object, as would further spectroscopy to refine $T_{\rm eff}$ and $\left[\frac{\rm Fe}{\rm H}\right]$.

5.20 KOI-428

This planetary system was discovered by Santerne et al. (2011b), and studied using the *Kepler* Q1 data. It was subsequently analysed in Paper IV, based on the Q1 and Q2 data. I have revisited it because Q3 to Q6 data are now available – all long-cadence – and cover 67 transits compared to the four in Q1 and the eight in Q2. The other modification to my previous work concerns the small L_3, which in Paper IV was ignored but in the current work is taken from the KIC as usual. The new orbital ephemeris based on the Q1 to Q6 data is:

$$T_0 = \mathrm{BJD(TDB)}\ 2\,455\,204.83996(20) + 6.8731697(96) \times E$$

A circular orbit was assumed, and each quarter of data was tackled separately with $N_{\rm int} = 10$. The full solutions are given in Tables A94 to A99 and the best fits displayed in Fig. 20. Correlated noise is unimportant, and the six light curves agree within the rather large MC errorbars (Table A100). This underlines the low information content in data with a sampling rate of only one per 30 min. Short-cadence data is necessary to obtain good results on this object. The revised $r_{\rm A}$ is comfortably larger than found in the two previous studies; the change is within the errors for Paper IV but outside the rather small errorbars quoted by Santerne et al. (2011b).

The revised physical properties (Table A101) are significantly different, due to their sensitivity to $r_{\rm A}$ via the stellar density. The masses are almost unchanged but the radii both increase by about 10%. The star is now quite evolved ($\log g_{\rm A} = 3.812 \pm 0.048 \pm 0.017$) and the largest known TEP host star at $R_{\rm A} = 2.48 \pm 0.17 \pm 0.20\,{\rm R}_\odot$ (the second-largest being Kepler-14 A at $2.09 \pm 0.11 \pm 0.02\,{\rm R}_\odot$; Sect. 5.12). A significant contribution to the uncertainties in these numbers comes from significant disagreement between the five model sets. The *DSEP* and *Y*^{2} models prefer a larger system scale and a slightly pre-main-sequence star,

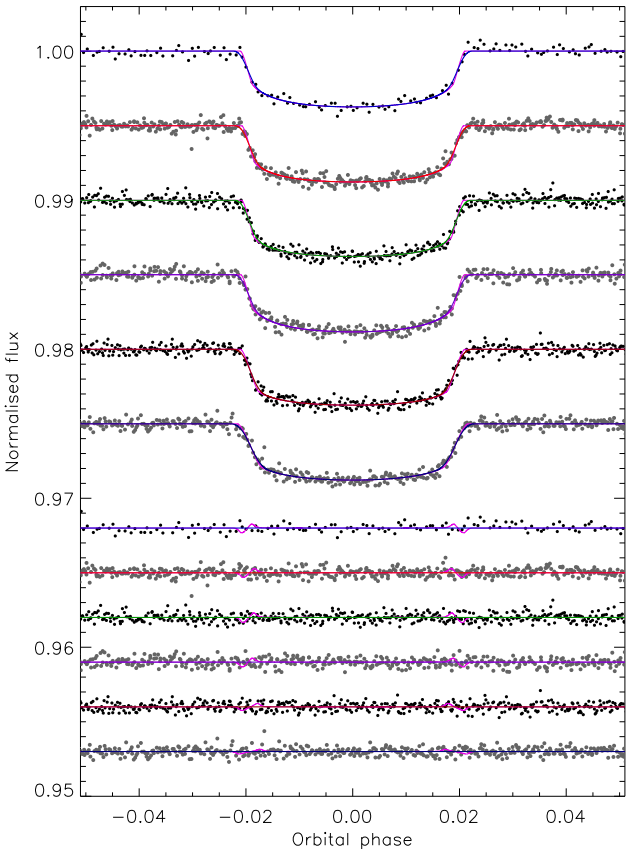

Figure 20. The *Kepler* Q1 (top) to Q6 (bottom) light curves of KOI-428 compared to the JKTEBOP best fits. Other comments are the same as Fig. 1.

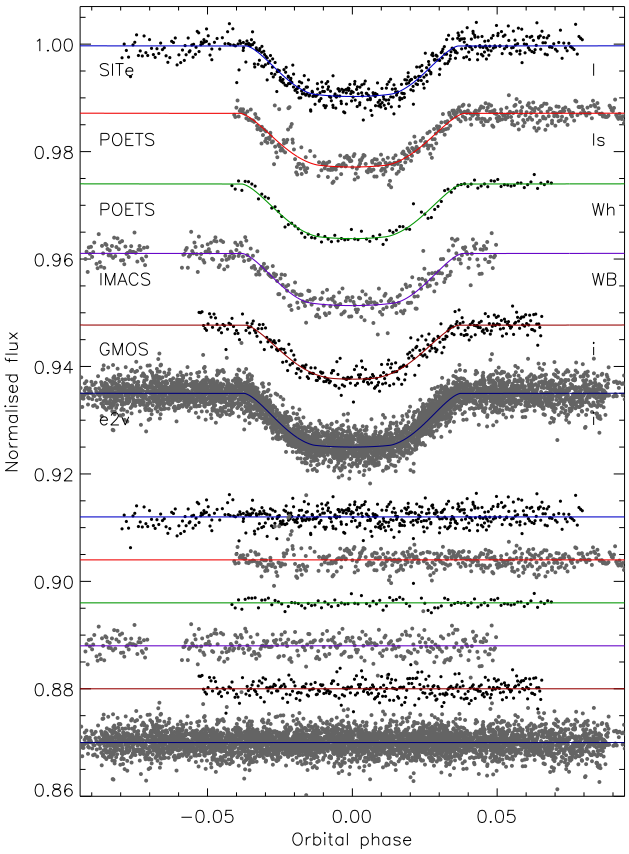

Figure 21. The Adams et al. (2011b) light curves of OGLE-TR-56 compared to the JKTEBOP best fits. The sources of the data and the filters used are annotated on the left and right, respectively. Other comments are the same as Fig. 6.

whereas the other three models find an age of 1–2 Gyr. Arbitrarily restricting the star to be on the main sequence would improve the agreement between models, but cannot be scientifically justified. Further *Kepler* photometry and ground-based spectroscopy would be important steps towards confirming and refining the physical properties of this planetary system.

5.21 OGLE-TR-56

OGLE-TR-56 has been studied in previous papers of this series, but qualifies for further attention due to the recent publication of much improved photometric data. Paper I summarises the observational history of OGLE-TR-56. Adams et al. (2011b) have since obtained 19 new transit light curves, primarily with the high-resolution MagIC camera on the Magellan telescopes. A few transits were also observed using the POETS and IMACS imagers on the same telescopes, and with GMOS on Gemini-South. Adams et al. (2011b) found a discrepancy between their transit duration and that obtained by Pont et al. (2007) from one transit observed using VLT/FORS2. A re-analysis of the VLT data resulted in a smaller discrepancy but more scattered photometry. One observation by Adams et al. (2011b) is of the same transit observed using the VLT, and the transit shape is in good agreement with the others presented by Adams et al. (2011b). I have therefore discounted the VLT data (as analysed in Paper I) as possibly suffering from systematic noise, and rederived the properties of OGLE-TR-56 based on the photometry obtained by Adams et al. (2011b). The datasets obtained using the SITe CCD and B, r and z filters were ignored as each do not cover a whole transit.

5.21.1 *Light curve analysis*

The data taken by Adams et al. (2011b) using the SITe CCD and I filter cover four transits, of which one was only partially observed and suffers from correlated noise so was rejected. 498 datapoints cover the remaining three transits and were fitted with $P_{\rm orb}$ fixed. The RP errors are slightly larger than the MC errors, and the LD-fixed solutions were adopted because the LD-fit/fix alternatives gave unphysical LD coefficients (Table A102).

Two transits were observed using POETS in the I_s band (a filter described as 'Schuler Astrodon Johnson-Cousins'). There is a short-lived increase in flux just before second contact for the first transit, which could be due to a stellar flare. The observations were taken at a high cadence, resulting in 8961 datapoints. These were binned in time by a factor of 20 to obtain 449 normal points, with four datapoints rejected by a 3σ clip. Once again, the RP errors were slightly larger than the MC ones, and the LD-fixed solution had to be adopted (Table A103).

One more transit was observed using POETS without a filter, in an attempt to achieve a lower Poisson noise. This transit event was the same one observed by Pont et al. (2007) using VLT/FORS2. The observations were taken at high cadence, resulting in 3245 datapoints. Those after time HJD 2453936.68 were rejected as they are well after the completion of the transit and suffer

from systematic noise. The remainder were time-binned by a factor of ten to give 95 normal points, then modelled using JKTEBOP. LD coefficients appropriate for the Cousins R band were used. The LD-fit/fix solutions are unfortunately poor (Table A104), and the LD-fixed solutions are possibly biased due to the imposition of R-band LD coefficients onto an unfiltered dataset. I therefore did not consider these data when calculating the final photometric parameters.

One transit (352 datapoints) was observed using IMACS and a wide-band filter (630–950 nm), for which I adopted Cousins I-band LD coefficients. Correlated noise was unimportant, but once again LD-fixed solutions had to be adopted (Table A105). Another transit (307 datapoints) was obtained using Gemini/GMOS and an i filter. For this one correlated noise was unimportant and it was possible to adopt the LD-fit/fix solution (Table A106).

Finally, nine complete transits were observed in the i band using Magellan/MagIC and its E2V CCD. For these 5186 datapoints I found that correlated noise was moderately important but that it was also possible to adopt the LD-fit/fix solution (Table A107). All light curves are compared in Fig. 21 to their respective best-fitting models.

One minor concern is that OGLE-TR-56 b is sufficiently close to its parent star to be distorted beyond the formal limit of applicability of the EBOP model. All other work on OGLE-TR-56 has been performed using spherical geometry, such as the analytical models by Mandel & Agol (2002) and Giménez (2006). JKTEBOP is more sophisiticated than those, in its use of biaxial spheroids to represent the stellar and planetary figures, but it would be worthwhile to check them using a more physically realistic model which incorporates Roche geometry. An excellent discussion of this can be found in Budaj (2011).

The agreement between the six different datasets from Adams et al. (2011b) is very good, ranging from $\chi^2_\nu = 0.19$ for i to $\chi^2_\nu = 0.98$ for k. The combined solution was calculated excluding the unfiltered POETS data, and the errorbars were (as usual) conservatively *not* reduced in light of the low χ^2_ν values. The solutions are summarised in Table A108, which also hosts a comparison with (the many) previous results for OGLE-TR-56. My new photometric parameters are in good agreement with those of Adams et al. (2011b) but are in severe disagreement with all previous work. This is expected because my new results are based on the data from Adams et al. 2011b, whereas all prior analyses had access to only the original survey-quality OGLE data and/or the VLT observations which have turned out to be affected by red noise (Adams et al. 2011b).

5.21.2 *Physical properties*

A major change in the photometric parameters induces a similar effect in the physical properties of the system. My results (Table A109) show that there is some disagreement between different model sets, in that the *Claret* and *Teramo* models coverge on solutions with a 1σ lower $T_{\rm eff}$. This causes a significant systematic uncertainty to enter the error budget, but does not obscure the main story. I have found physical properties which are very different from all previous estimates, and point to OGLE-TR-56 A being somewhat evolved ($M_{\rm A} = 1.339 \pm 0.077 \pm 0.066\,{\rm M}_\odot$ and $R_{\rm A} = 1.737 \pm 0.035 \pm 0.029\,{\rm R}_\odot$). By contrast, all nine previously published measurements of $R_{\rm A}$ were in the range 1.10–1.36 $\rm R_\odot$. The same situation is found for the planet ($M_{\rm b} = 1.41 \pm 0.17 \pm 0.05\,{\rm M_{Jup}}$), for which the new radius measurement is $R_{\rm b} = 1.734 \pm 0.051 \pm 0.029\,{\rm R_{Jup}}$ whereas all previous values are in the range 1.23–1.378 $\rm R_{Jup}$. This is illustrated in Fig. 22. OGLE-TR-56 b therefore joins the group of the most inflated TEPs. This is unsurprising insofar as its host star is relatively hot and massive. A detailed discussion of the most inflated TEPs is given by Southworth et al. (2012b).

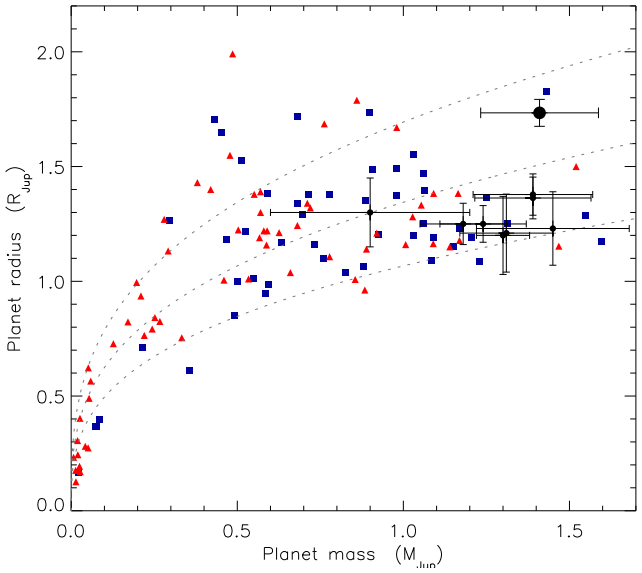

Figure 22. Mass–radius plot showing the known TEPs (blue squares for those in the *Homogeneous Studies* series and red triangles for the remainder) with their errorbars suppressed for clarity. The new result for OGLE-TR-56 b is shown with a large black filled circle, whereas previous results are shown with small black filled circles.

How did such a large change in the measured properties occur? Early analyses of the system (Konacki et al. 2003; Torres et al. 2004; Santos et al. 2006; Bouchy et al. 2005) all relied on on the OGLE discovery light curve (Udalski et al. 2002b) which is of low quality compared to dedicated follow-up observations. Later analyses (Pont et al. 2007; Torres et al. 2008; Paper II; Paper III) rested on the VLT light curve from Pont et al. (2007), which has been shown by Adams et al. (2011b) to suffer from substantial systematic noise. It is only with the data gathered by Adams et al. (2011b) that it is now possible to derive definitive physical properties of the system.

Adams et al. (2011b) themselves studied their light curves in detail, but adopted old values of $M_{\rm A}$ and $R_{\rm A}$ from Paper III for calculating the system properties. They therefore did not propagate the stellar density found from their light curves to the physical properties of the system, and so ended up with properties similar those found in previous works. It is only when the newer photometric data are used to specify the stellar density, and therefore its mass and radius in conjunction with theoretical models, that the system parameters experience a significant change. The physical properties of OGLE-TR-56 found in the current work are the first ones to provide a full picture of the system.

One moral from this story is that a single good light curve is not enough to provide a definitive set of physical properties, as undetected sysmatic errors may bias the results. A significant fraction of other TEPs might be subject to this concern, for example HD 80606 (Hébrard et al. 2010) and WASP-7 (Southworth et al. 2011). A second moral is that any significant revision to the photometric parameters should be propagated into the physical properties of the system.

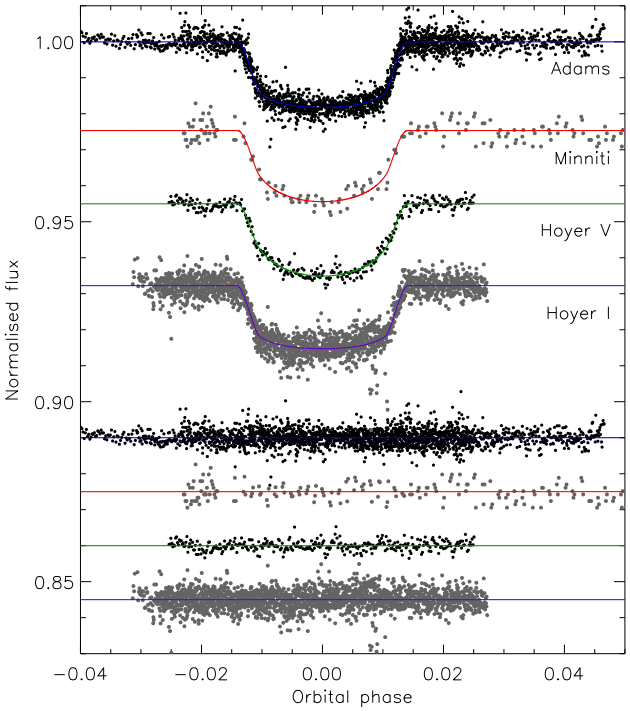

Figure 23. The Magellan (Adams et al. 2010a) and VLT (Minniti et al. 2007; Hoyer et al. 2011) light curves of OGLE-TR-111 compared to the JKTEBOP best fits. Other comments are the same as Fig. 6.

5.22 OGLE-TR-111

The transiting nature of OGLE-TR-111 was announced by Udalski et al. (2002a) and its planetary nature confirmed by Pont et al. (2004). Its publication history was summarised in Paper I (sect. 3.9), where the data from Winn et al. (2007) were analysed. Three new sets of transit light curves have been published since then, prompting this rediscussion of the system. Adams et al. (2010a) observed six transits through an SDSS i filter, using Magellan/MagIC-e2v high-resolution imager, allowing them to improve the measurement of $R_{\rm b}$ and dismiss the existence of the TTVs tentatively found by Díaz et al. (2008). Hoyer et al. (2011) studied five transits, one with VLT/FORS1 and a "*v-HIGH*" filter and the remaining four with VLT/FORS2 and a Bessell I filter. I have also included the single V-band light curve from Minniti et al. (2007) in my analysis.

The six transits observed by Adams et al. (2010a) are contained in 2205 datapoints, for which I found that correlated noise was moderately important. I fitted for $P_{\rm orb}$, and the light curve solutions are given in Table A110. Minniti et al. (2007) obtained 213 datapoints covering one transit in V, for which I found no evidence of correlated noise (Table A111). The data from Hoyer et al. (2011) were supplied with timestamps in JD, which I converted to BJD(TDB) before analysis. The V-band transit has 323 datapoints and the four I-band transits comprise 1967 datapoints. I found the RP errors to be larger than the MC errors for both datasets (Tables A112 and A113).

The light curve solutions are summarised in Table A114 and the best fits are shown in Fig. 23. The agreement between the light curves is good, except for k which has $\chi^2_\nu = 1.9$. This situation has occured frequently within this series of papers. Published photometric properties agree well with my own. A similar story occurs for the physical properties (Table A115), although I find a comparatively low concordance between the results for different stellar models. OGLE-TR-111 would benefit from an improved measurement of $K_{\rm A}$, although its faintness ($V = 16.96$) makes this non-trivial.

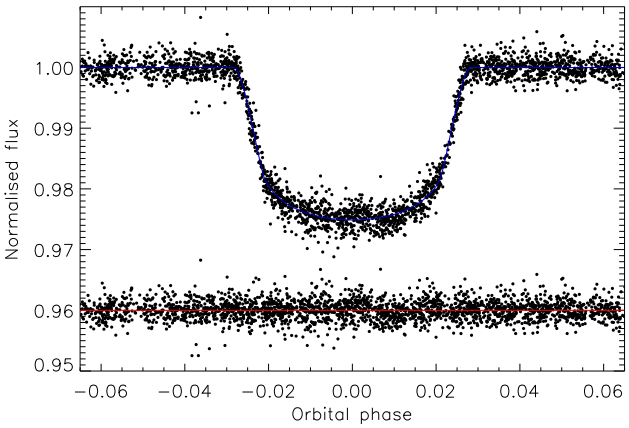

Figure 24. The Magellan light curve of OGLE-TR-113 (Adams et al. 2010b) compared to the JKTEBOP best fit. Other comments are the same as Fig. 6.

5.23 OGLE-TR-113

OGLE-TR-113 was also found to be a transiting system by Udalski et al. (2002a), and a planetary system by Bouchy et al. (2004). It was studied in Paper III (sect. 4.3 and fig. 7), based on the photometry presented by Gillon et al. (2006), Snellen & Covino (2007) and Díaz et al. (2007). Since then Adams et al. (2010b) have published six nice transit light curves from Magellan/MagIC, allowing them to revise $R_{\rm b}$ and set limits on TTVs. They found a possible gradual decrease in $P_{\rm orb}$, with a significance of 4σ, which should be investigated once a longer temporal baseline is available.

I fitted the data from Adams et al. (2010b), which represents 2697 datapoints, including $P_{\rm orb}$ as a fitted parameter. My initial model was compromised by some poor data which were included in the datafile but not in the analysis by Adams et al. (2010b). 79 datapoints were rejected, allowing a good fit to be found to the remaining data. I found correlated noise to be slightly important. The LD-fit/fix solution was adopted (Table A116 and Fig. 24).

The new data from Adams et al. (2010b) allow a great improvement in the photometric parameters (Table A117) and in the physical properties (Table A118). I found a good agreement between results from different model sets, and against values from the literature. As with OGLE-TR-111, a more precise $K_{\rm A}$ would be useful but difficult to achieve because the system is faint ($V = 16.48$).

5.24 OGLE-TR-132

Udalski et al. (2003) observed transits in this system, and Bouchy et al. (2004) confirmed its planetary nature. OGLE-TR-132 was studies in Paper I (sect. 3.10 and fig. 12) using a nice VLT/FORS2 light curve from Gillon et al. (2007). I have revisited the system because Adams et al. (2011a) has published a light curve of 4940 datapoints covering seven transits, using them to measure a revised $R_{\rm b}$ and put upper limits on the presence of TTVs. Two of these transits were observed at a much higher cadence (10–15 s) versus the rest (35–130 s), so these were time-binned by a factor of five.

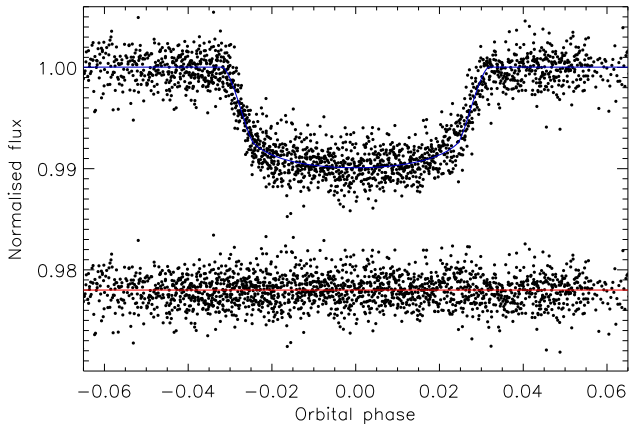

Figure 25. The Magellan light curves of OGLE-TR-132 from Adams et al. (2011a), compared to the JKTEBOP best fit. Other comments are the same as Fig. 6.

This is an important step if the data are modelled together and subjected to an RP algorithm.

The resulting 2131 datapoints were analysed, with the findings that modest correlated noise is present and that the LD-fit/fix solution is good (Table A119 and Fig. 25). Final photometric parameters were calculated from these results and those in Paper I. The agreement between these results and also with published values is excellent (Table A120). The ensuing physical properties (Table A121) are an improvement over Paper I due to the additional data, but are in good agreement with literature results. OGLE-TR-132 needs more RVs if its measured physical properties are going to be improved significantly.

5.25 OGLE-TR-L9

This was discovered by Snellen et al. (2009) based on archival OGLE data, follow-up four-band photometry from the GROND imager, and UVES spectroscopy. It is of interest as containing a massive planet ($4.4 \pm 1.5\,\mathrm{M_{Jup}}$) around an unusually hot star (6933 ± 58 K), and was duly studied in Paper III. Lendl et al. (2010) have recently obtained five more transits with GROND[9] I have modelled the combined dataset of six transits from Snellen et al. (2009) and Lendl et al. (2010) as they were obtained with the same instrument and observing strategy. The numbers of datapoints is as follows: 922 in g, 921 in r, 917 in i and 922 in z. In all cases the RP errors were smaller than the MC errors. The full sets of solutions can be found in Tables A122 to A125, the summary in Table A126, and the best fits in Fig. 26. The final photometric parameters agree well with those found by Lendl et al. (2010), as expected given the identical datasets used, but not so well with those from Snellen et al. (2009) or Paper III (both of which used the same smaller dataset).

Lendl et al. (2010) did not derive the full physical properties of OGLE-TR-L9, so Table A127 contains the first physical properties measured using their extensive photometry. The parameters are consistent with previous solutions, but with a useful lowering of the errorbars due to the new light curves. An improved K_A and $\left[\frac{\mathrm{Fe}}{\mathrm{H}}\right]$ are needed; the light curves are unusually not the observational bottleneck because these spectroscopic constraints are so poor (mainly due to the faintness of the system at $V \approx 15.5$).

[9] The datafiles as lodged on CDS are incorrect but the data are available on request to M. Lendl.

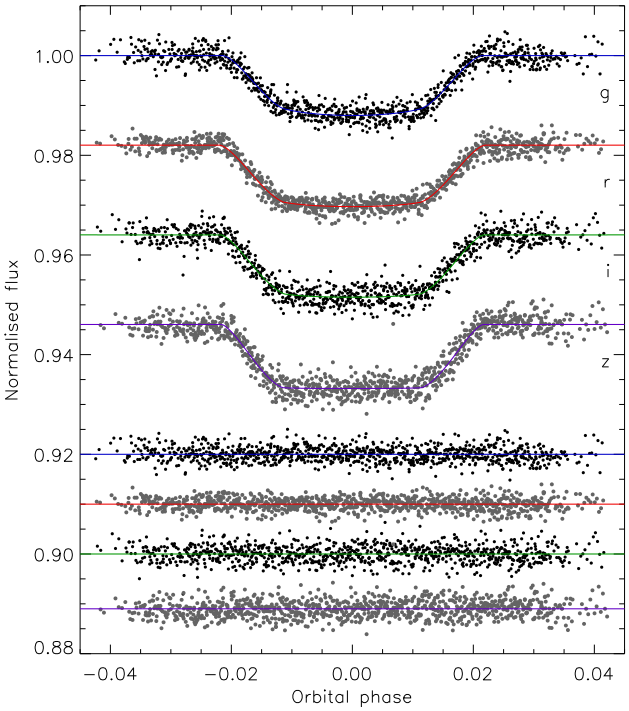

Figure 26. The GROND light curves of OGLE-TR-L9 from Lendl et al. (2010) compared to the JKTEBOP best fits. Other comments are the same as Fig. 6.

5.26 TrES-4

This system, containing a large and low-density planet, was studied in Paper III based on the photometry presented in the discovery paper (Mandushev et al. 2007). New data are now available from Chan et al. (2011), covering five transits in the i band obtained using KeplerCam. Here I present revised results incorporating these new data. A notable result since Paper III is the measurement of the Rossiter-McLaughlin effect by Narita et al. (2010), showing the system to be aligned to within 1.5σ.

TrES-4 is straightforward except for the presence of a much fainter star separated by only $1.5''$ on the sky. This was treated as third light (Paper III). The magnitude difference measured in the i band by Daemgen et al. (2009), $\Delta i = 4.560 \pm 0.017$, was converted into a flux ratio to obtain the constraint on L_3.

The data from Chan et al. (2011) cover five transits, two of them fully, with 765 datapoints. I fitted for P_orb, and found that correlated noise was unimportant and that the LD-fit/fix solutions were good (Table A128). These results were added to the B- and z-band (Mandushev et al. 2007) results from Paper III, and a comparatively poor agreement was found. The most concordant parameter was, unusually, k ($\chi^2_\nu = 0.4$), whereas the other photometric parameters have $\chi^2_\nu = 1.1$–1.8. The new i-band data yield results roughly in the middle of those from the B and z data, which are formally discrepant. The final photometric parameters are the weighted average of the individual ones from the B, i and z data, with the errorbars inflated to enforce $\chi^2_\nu = 1$ (Table A129). This leads to a significant difference with respect to Paper III, where the B data were rejected and the z-band results taken as final, but is in reasonable agreement with other studies. The best fits to the three light curves (i.e. those studied in Paper III as well as the current work) are plotted in Fig. 27.

When calculating the physical properties of TrES-4 I found

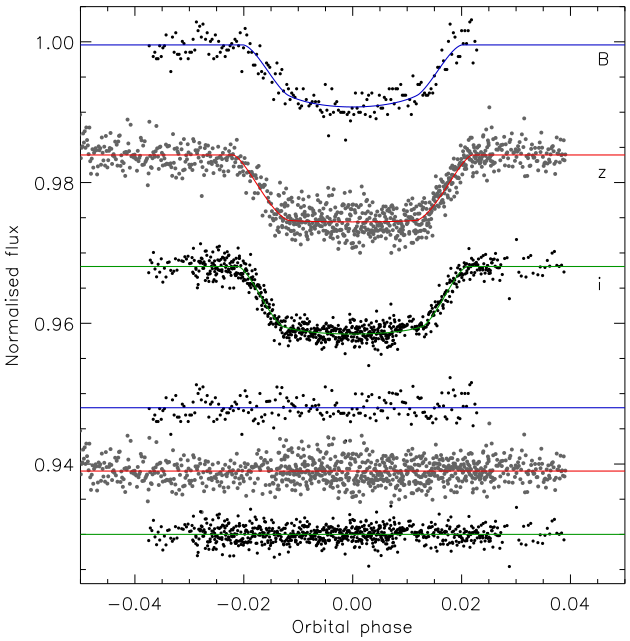

Figure 27. The B and z (Mandushev et al. 2007) and i light curves (Chan et al. 2011) of TrES-4 compared to the JKTEBOP best fits. Other comments are the same as Fig. 6.

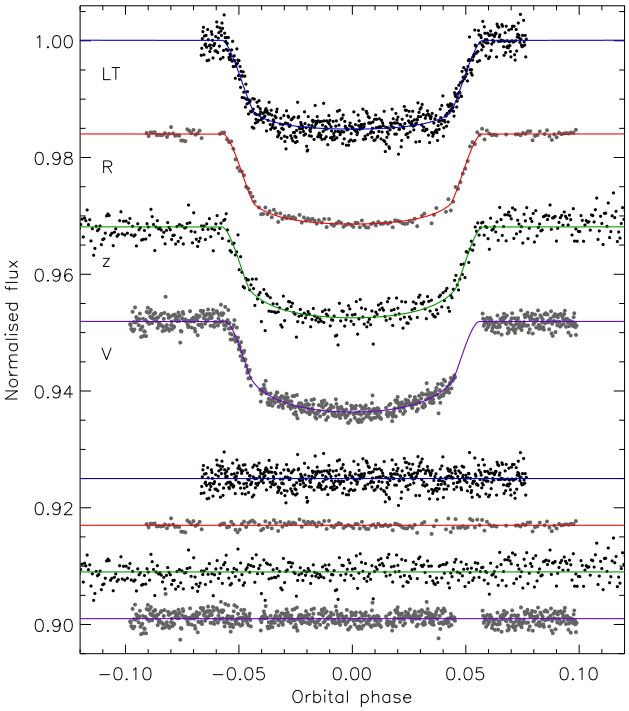

Figure 28. Light curve of WASP-12 compared to the JKTEBOP best fits. From top to bottom the datasets are from Hebb et al. (2009), Maciejewski et al. (2011), and two from Chan et al. (2011). Other comments are the same as Fig. 6.

that the different model sets did not agree completely. The Y^2 models are a strong outlier, but are also the closest to the spectroscopically-measured stellar $T_{\rm eff}$. These results have nevertheless been rejected, and the final values based on those from the other four sets of models (Table A130). They point to the planet having an unexpectedly large radius ($R_{\rm b} = 1.735 \pm 0.072 \pm 0.007\,{\rm R_{Jup}}$), confirming the conclusions from previous studies. I recommend that new transit photometry and échelle spectra are obtained for TrES-4 in order to provide a definitive answer to the question of its physical properties.

5.27 WASP-12

At the time of its discovery, WASP-12 contained the hottest, most irradiated and shortest-period planet then known (Hebb et al. 2009), making it a key object in our understanding of gas-giant planets. Occultations of the planet by the star have been observed in the z band (López-Morales et al. 2010), in the J, H and K_s bands (Croll et al. 2011), and in the 3.6, 4.5, 5.8 and 8.0 μm *Spitzer*/IRAC bands (Campo et al. 2011). Madhusudhan et al. (2011) interpreted the occultation depths in these bands as evidence of an enhanced ratio of carbon to oxygen in the atmosphere of the planet. Most recently, Cowan et al. (2012) used *Spitzer* to obtain photometry at 3.6 and 4.5 μm covering full orbits of WASP-1, and Swain et al. (2012) have measured transit and occultation depths in the infrared using HST/WFC3. High-precision optical transit photometry has been obtained by Maciejewski et al. (2011) and Chan et al. (2011) and used to confirm the large planetary radius measurement obtained by Hebb et al. (2009).

The possibility of orbital eccentricity in the WASP-12 system has received much attention. Hebb et al. (2009) found a value of $e = 0.049 \pm 0.015$, which was unexpected because tidal effects should have circularised such a short-period orbit (Goldreich & Soter 1966). The probability that this eccentricity is real is 99.5% according to the test of Lucy & Sweeney (1971). The occultation timing found by López-Morales et al. (2010) leads to the constraint $e\cos\omega = 0.0156 \pm 0.0035$, which agrees with the eccentricity detection of Hebb et al. (2009). However, the later occultation observations (Croll et al. 2011; Campo et al. 2011) define the eclipse shape much more precisely and constrain e to be very small and probably zero. Further support for a circular orbit comes from continued RV monitoring (Husnoo et al. 2011), and from consideration of the effect of tidal deformation of the host star on its measured RV (Arras et al. 2012). I have therefore assumed a circular orbit in the analysis below.

Hebb et al. (2009) presented photometry of two transits, a z-band one from LT/RATCam and a B-band one from the 0.8 m Tenagra telescope in Arizona. The former of the two datasets is of much better quality than the latter, and was included in my analysis. Maciejewski et al. (2011) obtained photometry of two transits in the Johnson R band with the CAHA 2.2m/CAFOS. The second dataset suffers from greater scatter, gaps and very little data outside transit, so I considered only the observations of the first transit. Chan et al. (2011) suffered from a lot of bad weather, but were able to get good observations of one transit in i using KeplerCam[10] and one transit in V using NOT/ALFOSC. Both datasets were added to my analysis.

One problem is the asphericity of the planet, which is technically outside the range of validity of the EBOP model (models assuming spherical planets will be more strongly affected). This was discussed in the context of OGLE-TR-56 in Sect. 5.21; the corol-

[10] The observing log in Chan et al. (2011) specifies a z-band filter for this dataset but the datafile from ApJ labels it as i. J. Winn (2011, private communication) has confirmed that the latter is correct.

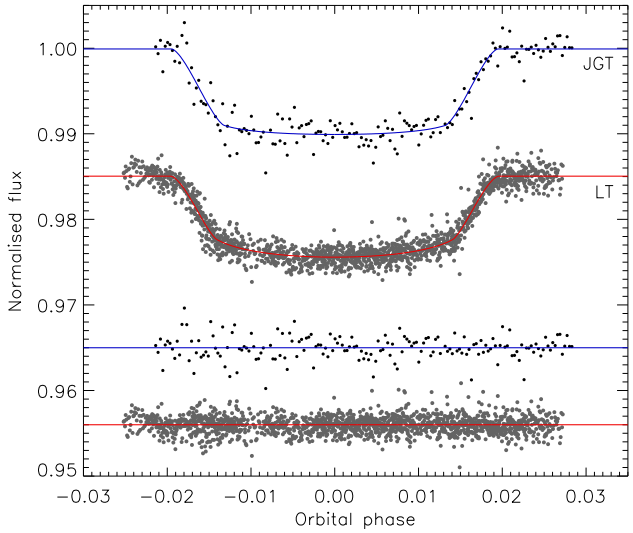

Figure 29. The JGT (top) and LT (lower) light curves of WASP-13 compared to the JKTEBOP best fits. Other comments are the same as Fig. 6.

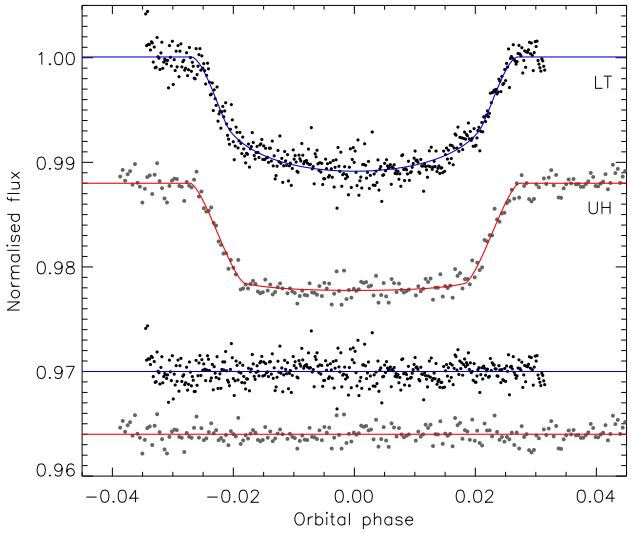

Figure 30. Light curves of WASP-14 from Joshi et al. (2009) and Johnson et al. (2009) compared to the JKTEBOP best fits. Other comments are the same as in Fig. 6.

lary for WASP-12 is that the volume-equivalent radius is up to 5% larger than the measured transit radius.

For all datasets I found that the MC errors were bigger than the RP errors and that the LD-fit/fix solutions were good. Results for the z-band data (613 points) are given in Table A131; for the R-band data (167 points) in Table A132; and for the i and V band data (470 and 670, respectively) in Table A133 and Table A134. The R-band data from Maciejewski et al. (2011) are of very high quality, with a scatter of only 0.59 mmag per point, and for these it was possible to adopt the LD-fitted solution. The best fits are plotted in Fig. 28.

Table A135 shows that the agreement between the four light curves is poor for k ($\chi^2_\nu = 2.5$) but fine for the other photometric parameters. Literature values are in good agreement with my final results, except for those of Chan et al. (2011). These authors find a lower k than I achieve for any of the four datasets considered.

The physical properties from the five different model sets display a comparatively poor agreement. The *VRSS* models are the most discrepant, but not by enough to entertain rejecting them. My final results (Table A136) therefore have a significant systematic error component, which however is still dwarfed by the statistical uncertainties. WASP-12 would really benefit from more precise measurements of the stellar $T_{\rm eff}$ and $\left[\frac{\rm Fe}{\rm H}\right]$; the mass of the star is uncertain by 14% ($M_{\rm A} = 1.38 \pm 0.19\,{\rm M}_\odot$) primarily due to the uncertainty in the star's atmospheric parameters. In comparison to literature results, I find $R_{\rm b} = 1.825 \pm 0.091 \pm 0.024\,{\rm R}_{\rm Jup}$, which is 1σ smaller than that from Maciejewski et al. (2011) and 1σ larger than that from Chan et al. (2011). WASP-12 b is therefore confirmed to have an unusually large radius.

5.28 WASP-13

Skillen et al. (2009) presented the discovery of the planetary nature of this system, with an analysis including observation of one full transit from the 0.95 m James Gregory Telescope at St. Andrews, UK. Barros et al. (2012) subsequently observed four transits using LT/RISE, although none in their entirety. I have analysed both datasets here, with $P_{\rm orb}$ incuded as a fitted parameter for the LT data (1530 datapoints) but not for the single transit from the JGT (173 datapoints). In both cases I found that correlated noise was significant: the RP errors are greater than the MC errors by a factor of 1.5 for the JGT data and by a factor of 2 for the LT data. The full solutions can be found in Table A137 and Table A138.

The photometric solutions are summarised in Table A139 and plotted in Fig. 29. The agreement between the two datasets is good except for k, as usual. The parameters found by Skillen et al. (2009) disagree with my own, by roughly 2σ depending on parameter. The reasons for this are not clear, given than I found the JGT and LT data to be consistent with each other, but may be related to inclusion of the SuperWASP data in their analysis. Barros et al. (2012) found photometric parameters which agree with my own, but with errorbars a factor of 2 smaller.

The *DSEP* models returned results in some disagreement with the other model sets, so were discluded when calculating the final physical properties. The extant $T_{\rm eff}$ and $\left[\frac{\rm Fe}{\rm H}\right]$ measurements for WASP-13 A are comparatively poor, and contribute to the uncertainties in the properties of this system. I find a larger and more massive star and planet, the change in each case being approximately the same size as the errorbars (Table A140). My revised system parameters makes WASP-13 b a rather large ($R_{\rm b} = 1.528 \pm 0.084 \pm 0.004\,{\rm R}_{\rm Jup}$) and low-density ($\rho_{\rm b} = 0.134 \pm 0.023\,\rho_{\rm Jup}$) TEP. The corresponding values found by Skillen et al. (2009) and Barros et al. (2012) are for a smaller and less massive star and planet. WASP-13 deserves further photometry and spectroscopy.

5.29 WASP-14

Discovered by Joshi et al. (2009), this planet is massive ($7.9 \pm 0.5\,{\rm M}_{\rm Jup}$) and has a definitely eccentric orbit ($e = 0.087 \pm 0.002$). These two properties are known to preferentially coincide (Southworth et al. 2009c). Johnson et al. (2009) has found that the planetary orbit is misaligned with the stellar spin ($\lambda = -33.1 \pm 7.4$ degrees) from Rossiter-McLaughlin observations. Blecic et al. (2011) obtained Spitzer observations of three occutations in order to probe the atmospheric properties of the planet from its infrared flux distribution.

The orbital eccentricity was detected by Joshi et al. (2009)

and has been confirmed by Husnoo et al. (2011) from continued RV monitoring. The most precise value comes from Blecic et al. (2011), whose three occultations allow a good constraint on $e\cos\omega$. I have adopted the measured $e\cos\omega = -0.02557 \pm 0.00038$ and $e\sin\omega = 0.0831 \pm 0.0021$ as constraints on the JKTEBOP models.

Joshi et al. (2009) presented an LT/RISE light curve of one transit containing 419 datapoints. The LD-fit/fix solutions are reasonable, and LD-fitted ones were not attempted (Table A141). Correlated noise occurs, causing RP errors to be 1.5 times greater than the MC errors.

Johnson et al. (2009) observed one transit (247 datapoints) using the UH 2.2m and OPTIC CCD, in a non-standard filter centred on 850 nm and 40 nm wide. They used this to constrain the orbital ephemeris to aid their Rossiter-McLaughlin measurement, but did not attempt a revision of the other parameters of the system. I adopted LD coefficients for the Cousins I band as this is reasonably close to the actual filter used (given that the predicted LD coefficients are significantly scattered). I found that the MC errors were larger than the RP ones, and that the LD-fit/fix solution is good (Table A142).

The light curve solutions are collected in Table A143 and the best fits are shown in Fig. 30. The agreement between the two light curves is unimpressive, with k having $\chi^2_\nu = 0.8$ and the other photometric parameters having $\chi^2_\nu = 1.5$–1.9. There is no specific reason to prefer one light curve over the other, so two results for the two have been combined and the errorbars inflated to account for the modest discrepancy. WASP-14 would clearly benefit from further photometric observations. Joshi et al. (2009) obtained results in agreement with those I find from their data, but in less good agreement with my final photometric parameters; no results are available from the other works cited above.

It is no surprise that I find a significantly different set of physical properties of WASP-14 compared to previous works (Table A144). The star becomes more massive and more evolved ($M_\mathrm{A} = 1.35 \pm 0.12\,\mathrm{M}_\odot$ and $R_\mathrm{A} = 1.67 \pm 0.10\,\mathrm{R}_\odot$). The planet's size is similarly revised, to $R_\mathrm{b} = 1.633 \pm 0.092 \pm 0.009\,\mathrm{R}_\mathrm{Jup}$), an increase of 4σ over the value of $1.281^{+0.075}_{-0.082}\,\mathrm{R}_\mathrm{Jup}$ found by Joshi et al. (2009). This new R_b is in clear disagreement with standard theoretical models of planets (e.g. Bodenheimer et al. 2003; Fortney et al. 2007; Chabrier et al. 2009). New light curves are vital in sorting out the moderate discrepancy between the two existing ones, and new stellar atmospheric parameters would allow a great improvement in our understanding of WASP-14.

5.30 WASP-21

Bouchy et al. (2010) discovered this planetary system, and obtained its physical properties using their version of the dEB constraint. They obtained adaptive-optics imaging which show no faint stars contaminating the flux from the system. The interest in WASP-21 lies in its Saturn-mass planet ($M_\mathrm{b} = 0.295 \pm 0.030\,\mathrm{M}_\mathrm{Jup}$) and the metallicity which is the lowest known for a TEP host star ($\left[\frac{\mathrm{Fe}}{\mathrm{H}}\right] = -0.46 \pm 0.11$). Barros et al. (2011) analysed LT/RISE observations covering three transits, of which the first was originally presented in the discovery paper (Bouchy et al. 2010). They used the Y^2 models to provide their additional constraint, yielding significant differences compared to those found by Bouchy et al. (2010): $M_\mathrm{A} = 0.86 \pm 0.04\,\mathrm{M}_\odot$ versus $1.01 \pm 0.03\,\mathrm{M}_\odot$, and $M_\mathrm{b} = 0.27 \pm 0.01\,\mathrm{M}_\odot$ versus $0.300 \pm 0.011\,\mathrm{M}_\odot$. WASP-21 is therefore an obvious candidate for inclusion in the *Homogeneous Studies* project.

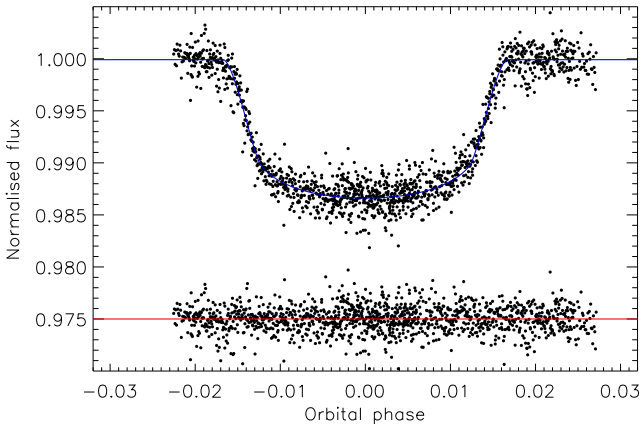

Figure 31. The LT light curve of WASP-21 compared to the JKTEBOP best fit. Other comments are the same as Fig. 6.

The LT data contain 1302 points over three transits (one each in 2008, 2009 and 2010), of which only one has full coverage. These were modelled with P_orb included as a fitted parameter. As with WASP-13, I found the RP errors to be 1.5 times larger than the MC errors, and that the LD-fit/fix solution was the best. The full set of solutions is in Table A145 and the best fit is plotted in Fig. 31. I find photometric parameters in reasonable agreement with those of Barros et al. (2011) but with larger errorbars (Table A146). The parameters from Bouchy et al. (2010) are discrepant, as has been discussed by Barros et al. (2011).

The physical properties arising from the five model sets are not in great agreement and this is straightforwardly attributable to the low $\left[\frac{\mathrm{Fe}}{\mathrm{H}}\right]$, for which the model predictions diverge. I find stellar and planetary masses closer to those from Bouchy et al. (2010) than Barros et al. (2011), but stellar and planetary radii which are bigger than found by either study (Table A147). The planet is now one of the least dense known ($\rho_\mathrm{b} = 0.137 \pm 0.021 \pm 0.003\,\rho_\mathrm{Jup}$). A new spectroscopic study of WASP-21 should be given priority, to confirm the low $\left[\frac{\mathrm{Fe}}{\mathrm{H}}\right]$ and increase the precision of the T_eff and $\left[\frac{\mathrm{Fe}}{\mathrm{H}}\right]$ measurements. A new light curve would be useful, as the current one dominates the uncertainty in R_A and R_b.

5.31 TEPs without new photometric studies: CoRoT-2, WASP-1, WASP-2, WASP-4, WASP-5, WASP-7, WASP-18 and XO-2

CoRoT-2 was studied in Paper IV but has since been the subject of a high-resolution spectroscopic study by Schröter et al. (2011). They find improved atmospheric parameters for the star ($T_\mathrm{eff} = 5598 \pm 34$ K and $\left[\frac{\mathrm{Fe}}{\mathrm{H}}\right] = 0.04 \pm 0.02$). For comparison, the values used in Paper IV were 5696 ± 70 K and 0.03 ± 0.06, respectively. The errorbars on the new measurements are rounded up to ± 50 K and ± 0.05 dex for the reasons given in Paper II. The new T_eff yields a slightly smaller system scale (Table A148), which means lower masses and radii for both components. The *Claret* models disagree slightly with the others, resulting in comparatively large systematic errorbars for some calculated quantities.

WASP-1 is in receipt of new results from Albrecht et al. (2011), who revised K_A to $125 \pm 5\,\mathrm{m\,s^{-1}}$ versus $111 \pm 9\,\mathrm{m\,s^{-1}}$, T_eff to 6213 ± 51 K versus 6110 ± 50 K, and $\left[\frac{\mathrm{Fe}}{\mathrm{H}}\right]$ to 0.17 ± 0.05 versus 0.23 ± 0.08. It is slightly unusual that an upward revision in T_eff brings about a downward revision in $\left[\frac{\mathrm{Fe}}{\mathrm{H}}\right]$, as the two are positively correlated in the spectral analysis of F, G and K stars.

The change in $T_{\rm eff}$ is also more than the errorbars, so a confirmation of this result would be appropriate. Table A149 shows that the new measurements modify the physical properties of WASP-1 only within the errorbars compared to Paper III. WASP-1 b's status as a hot and bloated planet is secure.

WASP-2 was studied by Southworth et al. (2010). New spectroscopic results (covering both RVs and atmospheric parameters) are now available from Albrecht et al. (2011). It is not straightforward to deduce the star's $T_{\rm eff}$ as multiple values available in the literature do not agree: Collier Cameron et al. (2007) found 5200 ± 200 K; Ghezzi et al. (2010) obtained 5227 ± 46 K; Triaud et al. (2010) found 5150 ± 80 K; Albrecht et al. (2011) obtained 5206 ± 50 K; and Maxted et al. (2011) deduced 5110 ± 60 K. I have therefore adopted 5170 ± 60 K as a value which encompasses all these determinations and leans towards the slightly lower $T_{\rm eff}$ from Maxted et al. (2011). Their value was obtained using the InfraRed Flux Method (IRFM: Blackwell & Shallis 1977; Blackwell et al. 1980), which I consider to be the most reliable method due to its emphasis on the stellar spectral energy distribution (which is conceptually nicer for $T_{\rm eff}$ determinations) and its limited dependence on theoretical calculations. Table A150 shows that the agreement between models is not great, as the star is substantially less massive than the Sun, but the overall results are a big step forward from previous measurements. This is due to the more precise $T_{\rm eff}$ and $\left[\frac{\rm Fe}{\rm H}\right]$, and means that WASP-2 is now one of the best-understood TEP systems.

WASP-4 gets a new $T_{\rm eff}$ of 5540 ± 55 K from Maxted et al. (2011), which is a substantial improvement on the 5500 ± 100 K (Gillon et al. 2009) used in Paper III and Southworth et al. (2009b). The agreement between models is imperfect with respect to the system properties, but the final results achieve a high precision and are in agreement with literature values (Table A151). WASP-4 is one of the best-understood TEP systems. The most effective improvement would be an increase in the precision of $\left[\frac{\rm Fe}{\rm H}\right]$, but this is not a high priority.

WASP-5 has received a new $T_{\rm eff}$ measurement of 5770 ± 65 K from Maxted et al. (2011) which is a useful improvement on the 5700 ± 100 K (Gillon et al. 2009) adopted in Paper III and by Southworth et al. (2009a). The ensuing physical properties (Table A152) show a modest agreement between models but a good agreement overall with literature values. WASP-5 could do with a better light curve and $\left[\frac{\rm Fe}{\rm H}\right]$ determination. New photometric data of WASP-5 have been obtained by several researchers – some is already published – and this will help in the near future.

WASP-7 has a revised $T_{\rm eff}$ of 6250 ± 70 K from Maxted et al. (2011), compared to the 6400 ± 100 K (Hellier et al. 2009b) used in Southworth et al. (2011). Note that WASP-7 was recently found to have an almost polar orbit through observations of the Rossiter-McLaughlin effect (Albrecht et al. 2012), but this study did not generate a new $K_{\rm A}$. Table A153 shows that there is little change in the system parameters with the new $T_{\rm eff}$. WASP-7 could still do with a better light curve and $\left[\frac{\rm Fe}{\rm H}\right]$ measurement.

WASP-18 gets a new $T_{\rm eff}$ of 6455 ± 70 K from Maxted et al. (2011), which is more precise than the 6400 ± 100 K (Hellier et al. 2009a) adopted in Paper III. Table A154 shows that there is not much difference in the physical properties, but reinforces the suggestion that the system is young as a zero age is the preferred solution for three of the five models. The errorbars may be artifically small due to the concomitant edge effects. WASP-18 would benefit from a new spectral-synthesis study as well as additional light curve data.

XO-2 has been awarded a revised $K_{\rm A}$ by Narita et al. (2011), who found 92.2 ± 1.7 m s^{-1} compared to the 85 ± 8 m s^{-1} (Burke et al. 2007) used in Paper III. XO-2 A remains the TEP host star with the highest $\left[\frac{\rm Fe}{\rm H}\right]$ at $+0.45 \pm 0.05$ dex. The models continue to disagree significantly (Table A155), due to the high $\left[\frac{\rm Fe}{\rm H}\right]$, and in such a way that is not accounted for by most analyses of this system. The new results are very similar to the previous ones from Paper III.

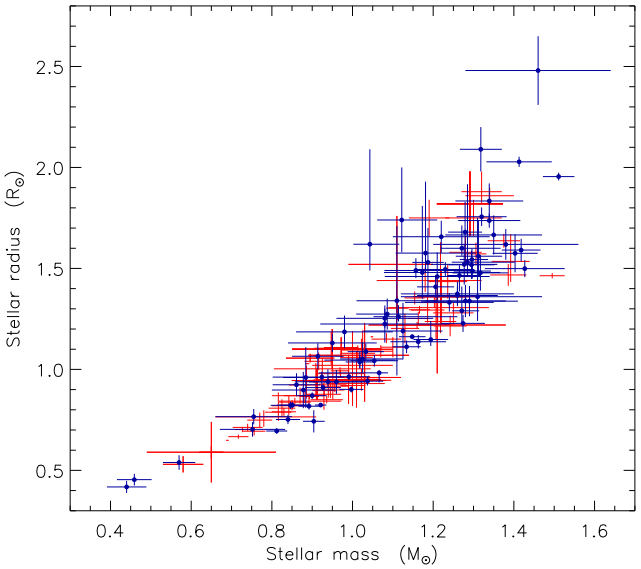

Figure 32. Mass–radius plot for the host stars of the known transiting extrasolar planets. Those objects studied in this work are shown with (blue) filled circles and numbers taken from the literature with (red) crosses.

6 PHYSICAL PROPERTIES OF THE TRANSITING EXTRASOLAR PLANETARY SYSTEMS

The primary result of this work is measurements of the physical properties of 38 transiting planetary systems. These are collected in Table 3 for the stellar components and in Table 4 for the planetary components. When combined with previous results from the *Homogeneous Studies* project, homogeneous physical properties are available for a total of 82 TEP systems. In the discussion below I have added results for all other known TEP systems as aggregated in the *Transiting Extrasolar Planets Catalogue* (TEPCat[11]) on 2012/05/02, which comprises 199 TEPs and six transiting brown dwarf systems including those objects in the *Homogeneous Studies* project.

Fig. 32 is a mass–radius plot for the host stars. This sample is very inhomogeneous due to observational biases and selection effects, particularly because the majority of objects have been discovered by wide-field surveys with small ground-based telescopes. The happy hunting ground is clearly unevolved stars in the mass interval 0.9–1.2 $\rm M_{\odot}$. Lower-mass stars are intrinsically dim and predominate at faint apparent magnitudes, which are inaccessible to wide-field telescopes with coarse pixel scales. Higher-mass stars are brighter and plentiful in such surveys, but exhibit faster rotation and fewer spectral lines, making confirmatory RV measurements difficult. More evolved stars are easier for RV measurements,

[11] The Transiting Extrasolar Planet Catalogue (TEPCat) is available at `http://www.astro.keele.ac.uk/jkt/tepcat/`

Table 3. Derived physical properties of the stellar components of the TEPs studied in this work. For most quantities the first errorbar gives the statistical errors and the second errorbar gives the systematic errors arising from the dependence on stellar theory.

System	Semimajor axis (AU)	Mass ($\mathrm{M}_\odot$)	Radius ($\mathrm{R}_\odot$)	$\log g_\mathrm{A}$ [cm/s]	Density ($\rho_\odot$)	Age (Gyr)
CoRoT-2	$0.02835 \pm 0.00029 \pm 0.00037$	$0.997 \pm 0.030 \pm 0.039$	$0.901 \pm 0.015 \pm 0.012$	$4.527 \pm 0.016 \pm 0.006$	1.362 ± 0.064	$1.2^{+1.8\ +0.7}_{-1.7\ -1.2}$
CoRoT-17	$0.04810^{+0.00109\ +0.00023}_{-0.00064\ -0.00034}$	$1.043^{+0.073\ +0.015}_{-0.041\ -0.022}$	$1.62^{+0.47\ +0.01}_{-0.13\ -0.01}$	$4.035^{+0.069\ +0.002}_{-0.208\ -0.003}$	$0.243^{+0.066}_{-0.126}$	$8.0^{+0.7\ +0.3}_{-3.5\ -0.4}$
CoRoT-18	$0.02860 \pm 0.00065 \pm 0.00019$	$0.861 \pm 0.059 \pm 0.017$	$0.924 \pm 0.057 \pm 0.006$	$4.442 \pm 0.043 \pm 0.003$	1.09 ± 0.16	unconstrained
CoRoT-19	$0.0512^{+0.0018\ +0.0003}_{-0.0011\ -0.0003}$	$1.181^{+0.125\ +0.024}_{-0.074\ -0.022}$	$1.576^{+0.354\ +0.011}_{-0.096\ -0.010}$	$4.115^{+0.047\ +0.003}_{-0.152\ -0.003}$	$0.302^{+0.049}_{-0.125}$	$4.9^{+0.6\ +0.3}_{-1.7\ -0.3}$
CoRoT-20	$0.0892 \pm 0.0028 \pm 0.0004$	$1.11 \pm 0.10 \pm 0.01$	$1.34 \pm 0.37 \pm 0.01$	$4.23 \pm 0.24 \pm 0.00$	0.46 ± 0.48	$5.9^{+1.6\ +0.8}_{-11.4\ -1.6}$
CoRoT-23	$0.04809^{+0.00122\ +0.00039}_{-0.00088\ -0.00056}$	$1.122^{+0.088\ +0.027}_{-0.061\ -0.039}$	$1.74^{+0.26\ +0.01}_{-0.16\ -0.02}$	$4.008^{+0.076\ +0.004}_{-0.107\ -0.005}$	$0.214^{+0.064}_{-0.066}$	$5.4^{+2.4\ +0.5}_{-1.7\ -1.0}$
HAT-P-3	$0.03842 \pm 0.00050 \pm 0.00063$	$0.900 \pm 0.036 \pm 0.044$	$0.870 \pm 0.016 \pm 0.014$	$4.513 \pm 0.020 \pm 0.007$	1.365 ± 0.078	$7.5^{+4.2\ +3.6}_{-3.8\ -2.7}$
HAT-P-6	$0.05244 \pm 0.00077 \pm 0.00051$	$1.295 \pm 0.057 \pm 0.038$	$1.518 \pm 0.070 \pm 0.015$	$4.188 \pm 0.035 \pm 0.004$	0.370 ± 0.045	$2.3^{+0.4\ +0.4}_{-0.8\ -0.3}$
HAT-P-9	$0.0529 \pm 0.0014 \pm 0.0003$	$1.28 \pm 0.10 \pm 0.02$	$1.339 \pm 0.080 \pm 0.008$	$4.293 \pm 0.046 \pm 0.002$	0.534 ± 0.082	$1.6^{+1.4\ +0.4}_{-2.0\ -0.4}$
HAT-P-14	$0.06108 \pm 0.00069 \pm 0.00036$	$1.418 \pm 0.048 \pm 0.025$	$1.591 \pm 0.056 \pm 0.009$	$4.187 \pm 0.025 \pm 0.003$	0.352 ± 0.031	$1.5^{+0.4\ +0.4}_{-0.4\ -0.2}$
Kepler-7	$0.06324 \pm 0.00042 \pm 0.00090$	$1.413 \pm 0.081 \pm 0.060$	$2.028 \pm 0.025 \pm 0.029$	$3.974 \pm 0.018 \pm 0.006$	0.169 ± 0.007	$2.9^{+0.0\ +0.3}_{-0.1\ -0.3}$
Kepler-12	$0.0555^{+0.0022\ +0.0003}_{-0.0013\ -0.0002}$	$1.157^{+0.147\ +0.022}_{-0.078\ -0.011}$	$1.490^{+0.061\ +0.009}_{-0.038\ -0.005}$	$4.155^{+0.018\ +0.003}_{-0.014\ -0.001}$	$0.3496^{+0.0064}_{-0.0091}$	$5.3^{+1.5\ +0.3}_{-5.0\ -0.3}$
Kepler-14	$0.0771 \pm 0.0010 \pm 0.0006$	$1.318 \pm 0.052 \pm 0.029$	$2.09 \pm 0.11 \pm 0.02$	$3.918 \pm 0.040 \pm 0.003$	0.145 ± 0.020	$2.2^{+1.6\ +0.9}_{-1.9\ -0.5}$
Kepler-15	$0.0583 \pm 0.0022 \pm 0.0009$	$1.08 \pm 0.12 \pm 0.05$	$1.253 \pm 0.047 \pm 0.020$	$4.275 \pm 0.017 \pm 0.007$	0.548 ± 0.008	$6.7^{+6.7\ +0.9}_{-1.6\ -1.1}$
Kepler-17	$0.02605^{+0.00018\ +0.00037}_{-0.00124\ -0.00050}$	$1.066^{+0.022\ +0.045}_{-0.150\ -0.061}$	$0.983^{+0.013\ +0.014}_{-0.047\ -0.019}$	$4.481^{+0.005\ +0.006}_{-0.023\ -0.008}$	$1.121^{+0.015}_{-0.034}$	$1.5^{+9.9\ +2.6}_{-1.2\ -1.5}$
KOI-135	$0.0440 \pm 0.0013 \pm 0.0002$	$1.24 \pm 0.11 \pm 0.02$	$1.332 \pm 0.046 \pm 0.007$	$4.281 \pm 0.017 \pm 0.002$	0.523 ± 0.022	$2.7^{+2.4\ +1.2}_{-1.4\ -0.5}$
KOI-196	$0.02895^{+0.00091\ +0.00020}_{-0.00086\ -0.00016}$	$0.939^{+0.092\ +0.019}_{-0.082\ -0.015}$	$0.939^{+0.062\ +0.006}_{-0.031\ -0.005}$	$4.466^{+0.018\ +0.003}_{-0.054\ -0.002}$	$1.135^{+0.046}_{-0.183}$	$6.2^{+5.2\ +0.6}_{-5.1\ -0.5}$
KOI-204	$0.0457 \pm 0.0017 \pm 0.0001$	$1.21 \pm 0.13 \pm 0.01$	$1.46 \pm 0.12 \pm 0.00$	$4.192 \pm 0.055 \pm 0.001$	0.388 ± 0.071	$4.7^{+4.4\ +0.3}_{-6.7\ -0.4}$
KOI-254	$0.02954 \pm 0.00068 \pm 0.00075$	$0.570 \pm 0.040 \pm 0.044$	$0.539 \pm 0.036 \pm 0.014$	$4.730 \pm 0.039 \pm 0.011$	3.63 ± 0.52	unconstrained
KOI-423	$0.1539 \pm 0.0073 \pm 0.0013$	$1.08 \pm 0.16 \pm 0.03$	$1.225 \pm 0.092 \pm 0.010$	$4.294 \pm 0.039 \pm 0.004$	0.586 ± 0.072	$4.4^{+2.2\ +0.7}_{-4.2\ -0.5}$
KOI-428	$0.0802 \pm 0.0032 \pm 0.0032$	$1.46 \pm 0.18 \pm 0.18$	$2.48 \pm 0.17 \pm 0.10$	$3.812 \pm 0.048 \pm 0.017$	0.096 ± 0.014	$0.8^{+3.6\ +0.7}_{-1.5\ -0.8}$
OGLE-TR-56	$0.02453 \pm 0.00046 \pm 0.00041$	$1.339 \pm 0.077 \pm 0.066$	$1.737 \pm 0.035 \pm 0.029$	$4.086 \pm 0.018 \pm 0.007$	0.256 ± 0.011	$3.0^{+2.9\ +0.3}_{-1.3\ -0.4}$
OGLE-TR-111	$0.04676 \pm 0.00092 \pm 0.00081$	$0.846 \pm 0.049 \pm 0.043$	$0.822 \pm 0.019 \pm 0.014$	$4.536 \pm 0.024 \pm 0.008$	1.52 ± 0.10	$9.7^{+9.6\ +5.3}_{-8.8\ -2.8}$
OGLE-TR-113	$0.02265 \pm 0.00099 \pm 0.00021$	$0.755 \pm 0.095 \pm 0.021$	$0.766 \pm 0.038 \pm 0.007$	$4.548 \pm 0.021 \pm 0.004$	1.679 ± 0.064	unconstrained
OGLE-TR-132	$0.03026 \pm 0.00098 \pm 0.00029$	$1.29 \pm 0.12 \pm 0.04$	$1.338 \pm 0.075 \pm 0.013$	$4.297 \pm 0.036 \pm 0.004$	0.540 ± 0.062	$1.7^{+3.5\ +2.1}_{-2.2\ -0.7}$
OGLE-TR-L9	$0.04047 \pm 0.00093 \pm 0.00026$	$1.427 \pm 0.099 \pm 0.028$	$1.499 \pm 0.042 \pm 0.010$	$4.241 \pm 0.016 \pm 0.003$	0.424 ± 0.018	$1.0^{+0.6\ +0.3}_{-1.3\ -0.2}$
TrES-4	$0.0502 \pm 0.0010 \pm 0.0002$	$1.339 \pm 0.084 \pm 0.016$	$1.834 \pm 0.087 \pm 0.007$	$4.038 \pm 0.033 \pm 0.002$	0.217 ± 0.025	$2.5^{+2.8\ +0.9}_{-0.7\ -2.5}$
WASP-1	$0.03920^{+0.00053\ +0.00015}_{-0.00031\ -0.00015}$	$1.265^{+0.052\ +0.015}_{-0.030\ -0.014}$	$1.465^{+0.051\ +0.006}_{-0.079\ -0.005}$	$4.209^{+0.051\ +0.002}_{-0.028\ -0.002}$	$0.403^{+0.069}_{-0.037}$	$2.7^{+0.4\ +0.5}_{-3.5\ -0.4}$
WASP-2	$0.03092 \pm 0.00046 \pm 0.00038$	$0.851 \pm 0.038 \pm 0.032$	$0.823 \pm 0.015 \pm 0.010$	$4.537 \pm 0.016 \pm 0.005$	1.524 ± 0.067	$8.2^{+6.3\ +2.5}_{-3.3\ -1.7}$
WASP-4	$0.02318 \pm 0.00037 \pm 0.00028$	$0.927 \pm 0.044 \pm 0.034$	$0.910 \pm 0.015 \pm 0.011$	$4.487 \pm 0.009 \pm 0.005$	1.230 ± 0.022	$6.4^{+2.7\ +1.9}_{-5.3\ -1.9}$
WASP-5	$0.02740 \pm 0.00040 \pm 0.00019$	$1.033 \pm 0.045 \pm 0.021$	$1.088 \pm 0.040 \pm 0.008$	$4.379 \pm 0.030 \pm 0.003$	0.801 ± 0.080	$5.6^{+2.2\ +1.1}_{-2.2\ -1.0}$
WASP-7	$0.0624 \pm 0.0011 \pm 0.0003$	$1.317 \pm 0.069 \pm 0.022$	$1.478 \pm 0.088 \pm 0.008$	$4.218 \pm 0.048 \pm 0.002$	0.408 ± 0.068	$1.9^{+0.7\ +0.3}_{-0.6\ -0.3}$
WASP-12	$0.02309 \pm 0.00096 \pm 0.00030$	$1.38 \pm 0.18 \pm 0.05$	$1.619 \pm 0.076 \pm 0.021$	$4.159 \pm 0.023 \pm 0.006$	0.325 ± 0.016	$2.0^{+0.7\ +0.3}_{-2.6\ -0.6}$
WASP-13	$0.0557 \pm 0.0018 \pm 0.0001$	$1.22 \pm 0.12 \pm 0.01$	$1.657 \pm 0.079 \pm 0.004$	$4.086 \pm 0.033 \pm 0.001$	0.268 ± 0.029	$5.0^{+2.6\ +1.6}_{-1.7\ -0.9}$
WASP-14	$0.0372 \pm 0.0011 \pm 0.0002$	$1.35 \pm 0.12 \pm 0.02$	$1.666 \pm 0.097 \pm 0.009$	$4.126 \pm 0.042 \pm 0.002$	0.293 ± 0.042	$2.4^{+1.5\ +0.2}_{-1.0\ -0.2}$
WASP-18	$0.02043 \pm 0.00029 \pm 0.00014$	$1.274 \pm 0.054 \pm 0.027$	$1.228 \pm 0.042 \pm 0.009$	$4.365 \pm 0.027 \pm 0.003$	0.687 ± 0.062	$0.4^{+1.0\ +0.4}_{-0.7\ -0.3}$
WASP-21	$0.0516 \pm 0.0020 \pm 0.0012$	$0.98 \pm 0.12 \pm 0.07$	$1.186 \pm 0.081 \pm 0.028$	$4.281 \pm 0.031 \pm 0.010$	0.587 ± 0.061	unconstrained
XO-2	$0.03616^{+0.00065\ +0.00100}_{-0.00182\ -0.00167}$	$0.924^{+0.054\ +0.076}_{-0.122\ -0.124}$	$0.962^{+0.026\ +0.027}_{-0.054\ -0.044}$	$4.436^{+0.037\ +0.012}_{-0.035\ -0.020}$	$1.034^{+0.127}_{-0.058}$	$6.5^{+23.2\ +5.3}_{-3.5\ -3.8}$

but their larger radii means transits of planet-sized objects are both longer and shallower, making it difficult to identify the photometric signature of a TEP in the first place. Space-based surveys are less biased towards unevolved stars, so the characteristics of this diagram will change in the near future as new discoveries flood in from *Kepler*.

Fig. 33 shows the mass–radius plot for the known TEPs in the region of parameter space occupied by Jupiter, with loci of constant density overlaid. Note that Jupiter does not lie on the $\rho_\mathrm{b} = \rho_\mathrm{Jup}$ locus because of the rotationally-induced difference between its equatorial radius (71 492 km) and volume-equivalent radius (66 991 km[12]). This Figure shows that the dominant population of TEPs is currently of mass 0.5–1.2 M_Jup and radius 0.9–1.7 R_Jup. The Saturnian objects are currently easily differentiated based on their masses and radii, but future discoveries may fill in the gaps between them, the Jupiter-like planets, and the lower-mass planets.

Correlations have previously been noticed between P_orb and g_b (Southworth et al. 2007) and P_orb and M_b (Mazeh et al. 2005). The relevant plots are shown in Figs. 34 and 35. In both cases there are quite a few planets whose properties put them outside the range of P_orb shown in these plots. For the following discussion I have neglected those planets which lie outside the relevant plot due to large mass or long period. I have also ignored super-Earth planets ($M_\mathrm{b} < 10\,\mathrm{M}_\oplus$) in order to obtain a sample of definitely gaseous objects.

The rank correlation test of Spearman (1904) returns a probability of 99.988% (3.9σ) that the P_orb–g_b correlation is real and 99.987% (3.8σ) that the P_orb–M_b correlation is real. In both cases, inclusion of all TEPs returns an increased significance level of

[12] `http://nssdc.gsfc.nasa.gov/planetary/factsheet/jupiterfact.html`

Table 4. Derived physical properties of the planets of the TEPs studied in this work. For many quantities the first errorbar gives the statistical errors and the second errorbar gives the systematic errors arising from the dependence on stellar theory.

System	Mass ($M_{\rm Jup}$)	Radius ($R_{\rm Jup}$)	$g_{\rm b}$ ($\rm m\,s^{-2}$)	Density ($\rho_{\rm Jup}$)	$T'_{\rm eq}$ (K)	Θ
CoRoT-2	$3.57 \pm 0.13 \pm 0.09$	$1.460 \pm 0.025 \pm 0.019$	41.5 ± 1.7	$1.073 \pm 0.057 \pm 0.014$	1521 ± 18	$0.1390 \pm 0.0048 \pm 0.0018$
CoRoT-17	$2.46^{+0.26}_{-0.24}{}^{+0.02}_{-0.04}$	$1.007^{+0.345}_{-0.092}{}^{+0.005}_{-0.007}$	60^{+13}_{-27}	$2.26^{+0.77}_{-1.35}{}^{+0.02}_{-0.01}$	1610^{+210}_{-70}	$0.225^{+0.031}_{-0.062}{}^{+0.002}_{-0.001}$
CoRoT-18	$3.27 \pm 0.17 \pm 0.04$	$1.251 \pm 0.083 \pm 0.008$	51.8 ± 6.6	$1.56 \pm 0.30 \pm 0.01$	1490 ± 45	$0.173 \pm 0.012 \pm 0.001$
CoRoT-19	$1.090^{+0.092}_{-0.077}{}^{+0.015}_{-0.014}$	$1.190^{+0.260}_{-0.069}{}^{+0.008}_{-0.007}$	$19.1^{+2.4}_{-6.2}$	$0.60^{+0.11}_{-0.27}{}^{+0.00}_{-0.00}$	1630^{+150}_{-40}	$0.0794^{+0.0064}_{-0.0150}{}^{+0.0005}_{-0.0005}$
CoRoT-20	$5.06 \pm 0.36 \pm 0.04$	$1.16 \pm 0.26 \pm 0.00$	93 ± 46	$3.0 \pm 2.5 \pm 0.0$	1100 ± 150	$0.70 \pm 0.17 \pm 0.00$
CoRoT-23	$3.06^{+0.32}_{-0.30}{}^{+0.05}_{-0.07}$	$1.18^{+0.19}_{-0.11}{}^{+0.01}_{-0.01}$	54^{+12}_{-14}	$1.75^{+0.63}_{-0.64}{}^{+0.02}_{-0.01}$	1710^{+110}_{-80}	$0.222^{+0.031}_{-0.036}{}^{+0.003}_{-0.002}$
HAT-P-3	$0.584 \pm 0.020 \pm 0.019$	$0.947 \pm 0.027 \pm 0.015$	16.14 ± 0.90	$0.643 \pm 0.052 \pm 0.011$	1189 ± 16	$0.0526 \pm 0.0019 \pm 0.0009$
HAT-P-6	$1.063 \pm 0.053 \pm 0.021$	$1.395 \pm 0.080 \pm 0.014$	13.5 ± 1.6	$0.366 \pm 0.064 \pm 0.004$	1704 ± 40	$0.0617 \pm 0.0043 \pm 0.0006$
HAT-P-9	$0.778 \pm 0.083 \pm 0.009$	$1.38 \pm 0.10 \pm 0.01$	10.1 ± 1.7	$0.275 \pm 0.066 \pm 0.002$	1540 ± 53	$0.0463 \pm 0.0056 \pm 0.0003$
HAT-P-14	$2.271 \pm 0.079 \pm 0.027$	$1.219 \pm 0.059 \pm 0.007$	37.9 ± 3.7	$1.17 \pm 0.17 \pm 0.01$	1624 ± 32	$0.1603 \pm 0.0089 \pm 0.0010$
Kepler-7	$0.453 \pm 0.067 \pm 0.013$	$1.649 \pm 0.030 \pm 0.024$	4.13 ± 0.35	$0.0944 \pm 0.0085 \pm 0.0014$	1619 ± 15	$0.0245 \pm 0.0021 \pm 0.0004$
Kepler-12	$0.430^{+0.053}_{-0.044}{}^{+0.005}_{-0.003}$	$1.706^{+0.069}_{-0.039}{}^{+0.011}_{-0.006}$	$3.66^{+0.33}_{-0.34}$	$0.0810^{+0.0075}_{-0.0081}{}^{+0.0003}_{-0.0005}$	1485^{+25}_{-25}	$0.0241^{+0.0022}_{-0.0024}{}^{+0.0001}_{-0.0002}$
Kepler-14	$7.68 \pm 0.37 \pm 0.11$	$1.126 \pm 0.049 \pm 0.008$	150 ± 13	$5.04 \pm 0.67 \pm 0.04$	1605 ± 39	$0.798 \pm 0.047 \pm 0.006$
Kepler-15	$0.696 \pm 0.097 \pm 0.022$	$1.289 \pm 0.050 \pm 0.021$	10.4 ± 1.1	$0.304 \pm 0.036 \pm 0.005$	1251 ± 27	$0.0582 \pm 0.0068 \pm 0.0009$
Kepler-17	$2.340^{+0.060}_{-0.228}{}^{+0.066}_{-0.089}$	$1.310^{+0.016}_{-0.063}{}^{+0.018}_{-0.025}$	$33.82^{+0.85}_{-1.01}$	$0.974^{+0.054}_{-0.037}{}^{+0.019}_{-0.014}$	1712^{+26}_{-25}	$0.0873^{+0.0047}_{-0.0023}{}^{+0.0017}_{-0.0012}$
KOI-135	$3.09 \pm 0.21 \pm 0.03$	$1.115 \pm 0.041 \pm 0.006$	61.6 ± 3.3	$2.09 \pm 0.16 \pm 0.01$	1603 ± 39	$0.1969 \pm 0.0100 \pm 0.0011$
KOI-196	$0.493^{+0.072}_{-0.070}{}^{+0.007}_{-0.005}$	$0.852^{+0.071}_{-0.031}{}^{+0.006}_{-0.005}$	$16.9^{+2.3}_{-3.2}$	$0.75^{+0.11}_{-0.18}{}^{+0.00}_{-0.01}$	1554^{+53}_{-29}	$0.0356^{+0.0048}_{-0.0054}{}^{+0.0002}_{-0.0002}$
KOI-204	$1.030 \pm 0.087 \pm 0.006$	$1.20 \pm 0.11 \pm 0.00$	17.6 ± 2.9	$0.55 \pm 0.14 \pm 0.00$	1568 ± 59	$0.0647 \pm 0.0063 \pm 0.0002$
KOI-254	$0.500 \pm 0.055 \pm 0.026$	$0.999 \pm 0.064 \pm 0.026$	12.4 ± 1.8	$0.469 \pm 0.093 \pm 0.012$	787 ± 26	$0.0518 \pm 0.0059 \pm 0.0013$
KOI-423	$17.9 \pm 1.8 \pm 0.3$	$1.092 \pm 0.077 \pm 0.009$	372 ± 38	$12.9 \pm 2.1 \pm 0.1$	851 ± 25	$4.69 \pm 0.35 \pm 0.04$
KOI-428	$2.16 \pm 0.40 \pm 0.18$	$1.44 \pm 0.11 \pm 0.06$	25.7 ± 5.0	$0.67 \pm 0.17 \pm 0.03$	1744 ± 51	$0.165 \pm 0.028 \pm 0.007$
OGLE-TR-56	$1.41 \pm 0.17 \pm 0.05$	$1.734 \pm 0.051 \pm 0.029$	11.6 ± 1.3	$0.253 \pm 0.031 \pm 0.004$	2482 ± 30	$0.0298 \pm 0.0033 \pm 0.0005$
OGLE-TR-111	$0.55 \pm 0.10 \pm 0.02$	$1.011 \pm 0.035 \pm 0.017$	13.2 ± 2.5	$0.49 \pm 0.10 \pm 0.01$	1019 ± 20	$0.060 \pm 0.011 \pm 0.001$
OGLE-TR-113	$1.23 \pm 0.20 \pm 0.02$	$1.088 \pm 0.054 \pm 0.010$	25.7 ± 3.4	$0.89 \pm 0.13 \pm 0.01$	1342 ± 22	$0.0678 \pm 0.0095 \pm 0.0006$
OGLE-TR-132	$1.17 \pm 0.15 \pm 0.02$	$1.229 \pm 0.075 \pm 0.012$	19.2 ± 2.8	$0.59 \pm 0.11 \pm 0.01$	1991 ± 42	$0.0445 \pm 0.0056 \pm 0.0004$
OGLE-TR-L9	$4.4 \pm 1.5 \pm 0.1$	$1.633 \pm 0.045 \pm 0.011$	40 ± 13	$0.94 \pm 0.32 \pm 0.01$	2034 ± 22	$0.151 \pm 0.051 \pm 0.001$
TrES-4	$0.897 \pm 0.075 \pm 0.007$	$1.735 \pm 0.072 \pm 0.007$	7.39 ± 0.76	$0.161 \pm 0.021 \pm 0.001$	1805 ± 40	$0.0387 \pm 0.0033 \pm 0.0002$
WASP-1	$0.980^{+0.047}_{-0.042}{}^{+0.008}_{-0.007}$	$1.493^{+0.061}_{-0.091}{}^{+0.006}_{-0.006}$	$10.9^{+1.5}_{-0.9}$	$0.275^{+0.058}_{-0.032}{}^{+0.001}_{-0.001}$	1830^{+33}_{-49}	$0.0406^{+0.0031}_{-0.0023}{}^{+0.0002}_{-0.0002}$
WASP-2	$0.880 \pm 0.031 \pm 0.022$	$1.063 \pm 0.025 \pm 0.013$	19.31 ± 0.80	$0.685 \pm 0.042 \pm 0.008$	1286 ± 17	$0.0601 \pm 0.0019 \pm 0.0007$
WASP-4	$1.249 \pm 0.043 \pm 0.030$	$1.364 \pm 0.024 \pm 0.016$	16.64 ± 0.33	$0.460 \pm 0.014 \pm 0.006$	1673 ± 17	$0.0458 \pm 0.0010 \pm 0.0005$
WASP-5	$1.595 \pm 0.048 \pm 0.022$	$1.175 \pm 0.055 \pm 0.008$	28.6 ± 2.6	$0.92 \pm 0.12 \pm 0.01$	1753 ± 35	$0.0719 \pm 0.0034 \pm 0.0005$
WASP-7	$0.98 \pm 0.13 \pm 0.01$	$1.374 \pm 0.094 \pm 0.008$	12.9 ± 2.4	$0.353 \pm 0.087 \pm 0.002$	1530 ± 45	$0.067 \pm 0.010 \pm 0.000$
WASP-12	$1.43 \pm 0.13 \pm 0.04$	$1.825 \pm 0.091 \pm 0.024$	10.63 ± 0.53	$0.220 \pm 0.019 \pm 0.003$	2523 ± 45	$0.0262 \pm 0.0013 \pm 0.0003$
WASP-13	$0.512 \pm 0.060 \pm 0.002$	$1.528 \pm 0.084 \pm 0.004$	5.44 ± 0.73	$0.134 \pm 0.023 \pm 0.000$	1531 ± 37	$0.0307 \pm 0.0035 \pm 0.0001$
WASP-14	$7.90 \pm 0.46 \pm 0.09$	$1.633 \pm 0.092 \pm 0.009$	73.4 ± 7.1	$1.69 \pm 0.25 \pm 0.01$	2090 ± 59	$0.265 \pm 0.015 \pm 0.001$
WASP-18	$10.38 \pm 0.30 \pm 0.15$	$1.163 \pm 0.054 \pm 0.008$	190 ± 16	$6.18 \pm 0.83 \pm 0.04$	2413 ± 44	$0.286 \pm 0.013 \pm 0.002$
WASP-21	$0.295 \pm 0.027 \pm 0.014$	$1.263 \pm 0.085 \pm 0.029$	4.58 ± 0.45	$0.137 \pm 0.021 \pm 0.003$	1340 ± 32	$0.0245 \pm 0.0019 \pm 0.0006$
XO-2	$0.593^{+0.025}_{-0.057}{}^{+0.033}_{-0.054}$	$0.984^{+0.031}_{-0.071}{}^{+0.027}_{-0.045}$	$15.2^{+1.8}_{-0.8}$	$0.582^{+0.116}_{-0.046}{}^{+0.028}_{-0.016}$	1328^{+17}_{-28}	$0.0472^{+0.0040}_{-0.0016}{}^{+0.0022}_{-0.0013}$

the correlation (4.8σ and 5.8σ respectively). Both correlations are therefore supported by the current data.

Hansen & Barman (2007) divided up eighteen of the twenty TEPs then known into two classes based on their position in a diagram of Θ versus $T_{\rm eq}$. An updated version of the diagram can be seen in Fig. 36, and agrees with previous conclusions (Paper II) that the division between the classes is blurred into insignificance. A dotted line at $\Theta = 0.055$ has been drawn to show the expected boundaries between Class I ($\Theta \approx 0.07 \pm 0.01$) and Class II ($\Theta \approx 0.04 \pm 0.01$). The previously postulated gap in the distribution is no longer apparent, so the division into two classes can now be safely ignored.

Fig. 37 takes a different approach to illustrating the distributions of physical properties of the known TEPs. Distributions have been obtained for each property given in Table 4, and for the *Homogeneous Studies* objects and for all objects. Each distribution was obtained by calculating a Gaussian function for each planet with a mean and standard deviation equal to the relevant property and its uncertainty, and then taking the sum over all planets in the sample. This produces an alternative to the histogram which avoids the loss of information implicit in the binning process.

Fig. 37a shows that the mass distribution of TEPs has a broad plateau around 0.5–1.2 $M_{\rm Jup}$, with a peak at the lower edge of this interval. A secondary peak, representing the Saturnian TEPs, occurs around 0.2 $M_{\rm Jup}$. The distribution then rises towards the lowest masses. Fig. 37b shows the situation for planet radius; the distribution is bimodal with peaks near 1.2 $R_{\rm Jup}$ and 0.2 $R_{\rm Jup}$. The lower-radius peak is almost entirely absent from the *Homogeneous Studies* sample, as it is dominated by planets from the *Kepler* satellite which were discovered and characterised by TTVs. Such systems are more complicated to study than normal Hot Jupiters, and there are no plans to include them in the current series of papers.

Fig. 37c shows the distribution of planet surface gravities. The sharp peak around 9 $\rm m\,s^{-2}$ is due to the extremely precise measurement for HD 209458. The determination of $g_{\rm b}$ requires only directly measurable photometric and spectroscopic parameters ($r_{\rm b}$, i, $K_{\rm A}$ and e), so can be measured to extremely high precision in favourable cases. In the case of HD 209458, $g_{\rm b}$ =

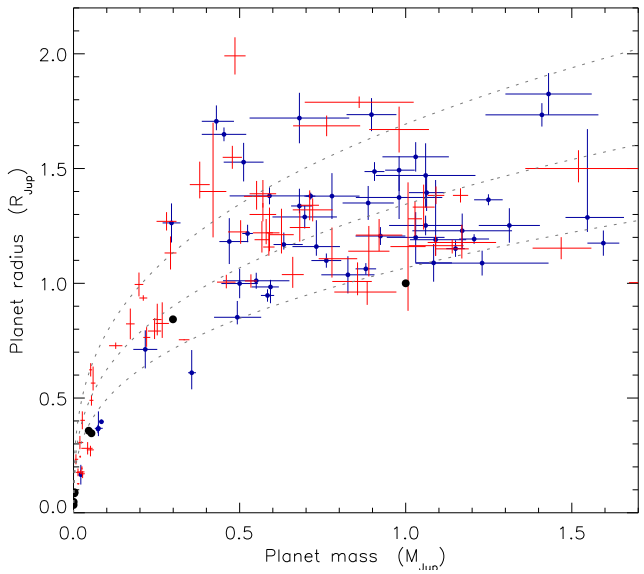

Figure 33. Mass–radius plot for the known transiting extrasolar planets. Symbols are as in Fig. 32 The four gas giant planets in our Solar System are denoted with (black) filled circles. Dotted lines show loci where density equals 1.0, 0.5 and 0.25 $\rho_{\rm Jup}$.

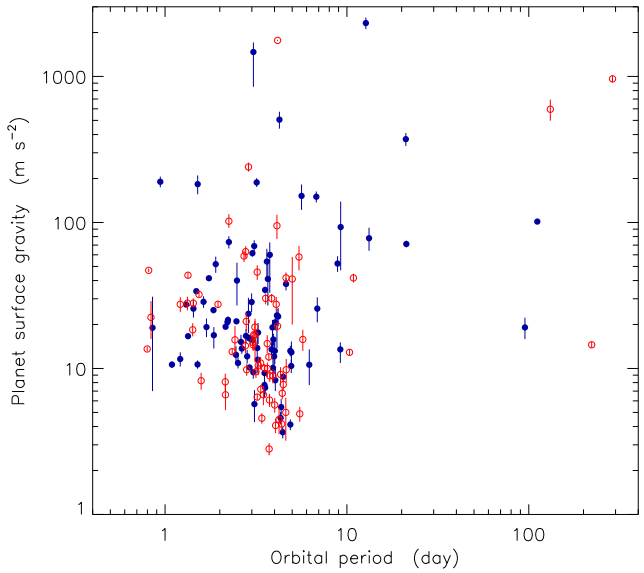

Figure 34. Plot of the orbital periods versus the surface gravities of the dominant population of known TEPs. Symbols are as in Fig. 32.

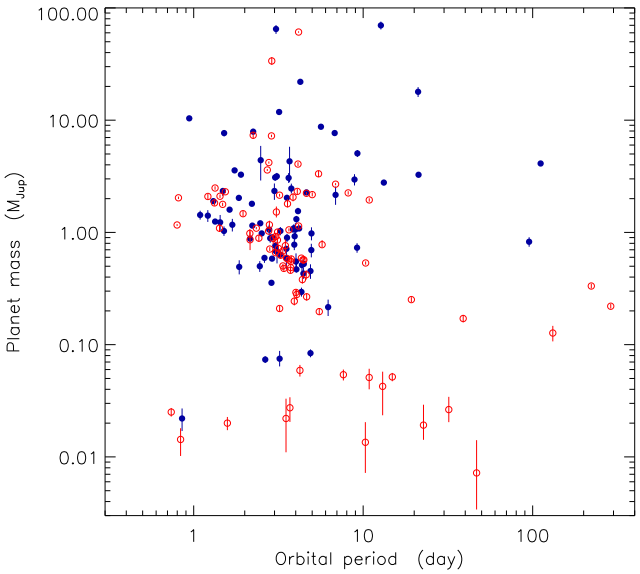

Figure 35. Plot of the orbital periods versus the masses of the dominant population of known TEPs. Symbols are as in Fig. 32.

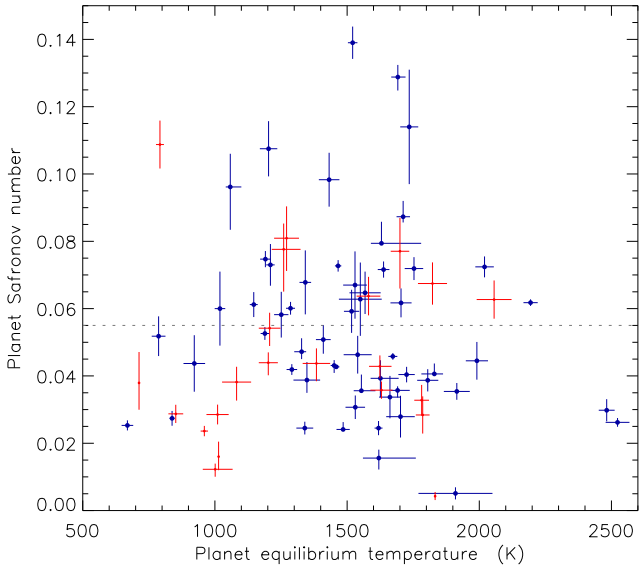

Figure 36. Plot of equilibrium temperature versus Safronov number for the full sample of planets. Objects shown with (blue) circles were studied in this work; those which are just (red) errorbars were not. The dotted line shows the separation between Class A and Class B proposed by Hansen & Barman (2007).

$9.30 \pm 0.08\,{\rm m\,s^{-2}}$ (Paper I). The distribution of planetary densities is plotted in Fig. 37d, and has a very similar functional form to that for $g_{\rm b}$ but with greater smoothness. This is because the precision of a $\rho_{\rm b}$ value is very sensitive to the quality of the transit light curves, but is also subject to systematic error from the model-derived additional constraint. In the case of HD 209458, $\rho_{\rm b} = 0.254 \pm 0.004 \pm 0.002\,\rho_{\rm Jup}$.

Fig. 37e depicts the distribution of $T'_{\rm eq}$, which is noisy but has a broad peak around 1500–1800 K. Ground-based surveys are observationally biased in favour of short-period planets, so hot planets are over-represented in the known TEP population. Finally, Fig. 37f shows the result for Θ. The division between Class I and Class II planets (Hansen & Barman 2007) is shown with a grey dotted line, and coincides with one of several local minima in the distribution function.

7 FOLLOW-UP OBSERVATIONS

Most of the TEPs in the current work would benefit from further observations of some sort, and this is summarised in Table 5. In many cases the dominant uncertainty stems from the quality of the light curve. This remains true for many of the CoRoT systems, even though they have space-based data. In each case this is due to their relative faintness (remember that the aperture of the CoRoT tele-

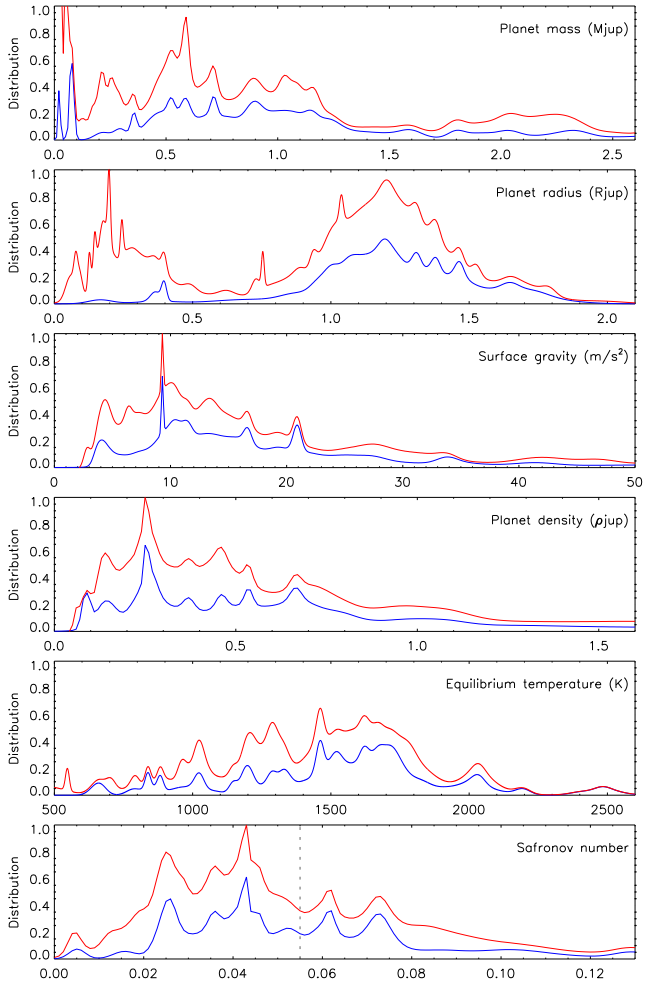

Figure 37. Plots of the distributions of planet properties. From top to bottom these are $M_{\rm b}$, $R_{\rm b}$, $g_{\rm b}$, $\rho_{\rm b}$, $T'_{\rm eq}$ and Θ. In each case the upper (red) line shows the distribution for all known TEPs and the lower (blue) line shows that for the TEPs considered within the current series of papers.

scope is only 27 cm) and/or that few transits were seen due to either a short observing sequence or a long orbital period.

Additional RV measurements are useful too. In many circumstances, particularly for the fainter objects, the RVs are good enough to unambiguously confirm the planetary nature of a system but are the dominant source of uncertainty in the planetary masses. Now over 200 TEPs are known it seems appropriate to concentrate follow-up resources on measuring the physical properties of a golden subset of these to high precision. An additional requirement of RVs is definition of the orbital shape (e and ω), and imprecise measurements of these quantities compromise measurements of the photometric parameters (in particular $r_{\rm A}$).

The physical properties of quite a few of the TEPs are also limited by the precision of the $T_{\rm eff}$ and $\left[\frac{\rm Fe}{\rm H}\right]$ measurements available. In many cases this can be improved, but in some cases this is not an option because the errorbars are already close to the limit set by our understanding of low-mass stars (taken to be 50 K in $T_{\rm eff}$ and 0.05 dex in $\left[\frac{\rm Fe}{\rm H}\right]$). There is no immediate prospect of lowering these thresholds; in fact there is evidence that they are already slightly optimistic (Bruntt et al. 2010b, 2012).

Quite a few of the TEPs have ephemerides which will become uncertain over the timescale of a few years. To investigate this I compiled a catalogue of ephemerides of all known TEPs and identified the first predicted times of transit which were uncertain by one hour, and by half of one transit duration. A list of objects for which one of these dates is earlier than the year 2022 is given in Table 6. The *Kepler* planets are not included in this analysis because they continue to be observed and will benefit from significantly improved ephemerides once these data become available. The list of the other planets is dominated by CoRoT objects, and it is notable that the ephemerides for CoRoT-4, CoRoT-14 and CoRoT-17 are already uncertain by more than one hour. HAT-P-31 is present in the list due to the fact that there is no published follow-up photometry of this object at all, only the discovery data from the HAT survey cameras. Further photometric observations of these objects, such as those obtained by the TERMS project (Kane et al. 2009; Dragomir et al. 2011), are needed before the predictive power of their ephemerides deteriorates much further.

Table 5. Summary of which further observations would be useful for the TEPs studied in this work. ⋆ indicates where additional data would be useful, and ⋆⋆ denotes where it would be useful but difficult to either obtain or analyse. I do not suggest the need for new data when such data are already in the process of being obtained (e.g. *Kepler* photometry).

System	Photometric observations	Radial velocities	Spectral synthesis
CoRoT-2			
CoRoT-17	⋆⋆	⋆⋆	⋆⋆
CoRoT-18	⋆⋆		⋆⋆
CoRoT-19	⋆		
CoRoT-20	⋆		
CoRoT-23	⋆⋆	⋆⋆	⋆⋆
HAT-P-3			
HAT-P-6	⋆		
HAT-P-9	⋆		⋆
HAT-P-14	⋆		
Kepler-7		⋆	
Kepler-12		⋆	⋆
Kepler-14			⋆⋆
Kepler-15		⋆	⋆
Kepler-17			
KOI-135			⋆
KOI-196			⋆
KOI-204		⋆⋆	⋆⋆
KOI-254		⋆⋆	⋆⋆
KOI-423	⋆	⋆	⋆
KOI-428		⋆⋆	⋆⋆
OGLE-TR-56		⋆⋆	
OGLE-TR-111		⋆⋆	
OGLE-TR-113		⋆⋆	⋆⋆
OGLE-TR-132		⋆⋆	
OGLE-TR-L9		⋆⋆	⋆⋆
TrES-4	⋆	⋆	⋆
WASP-1			⋆
WASP-2			
WASP-4			
WASP-5			⋆
WASP-7	⋆	⋆	⋆
WASP-12			⋆
WASP-13	⋆	⋆	⋆
WASP-14	⋆		⋆
WASP-18			
WASP-21	⋆		⋆
XO-2			

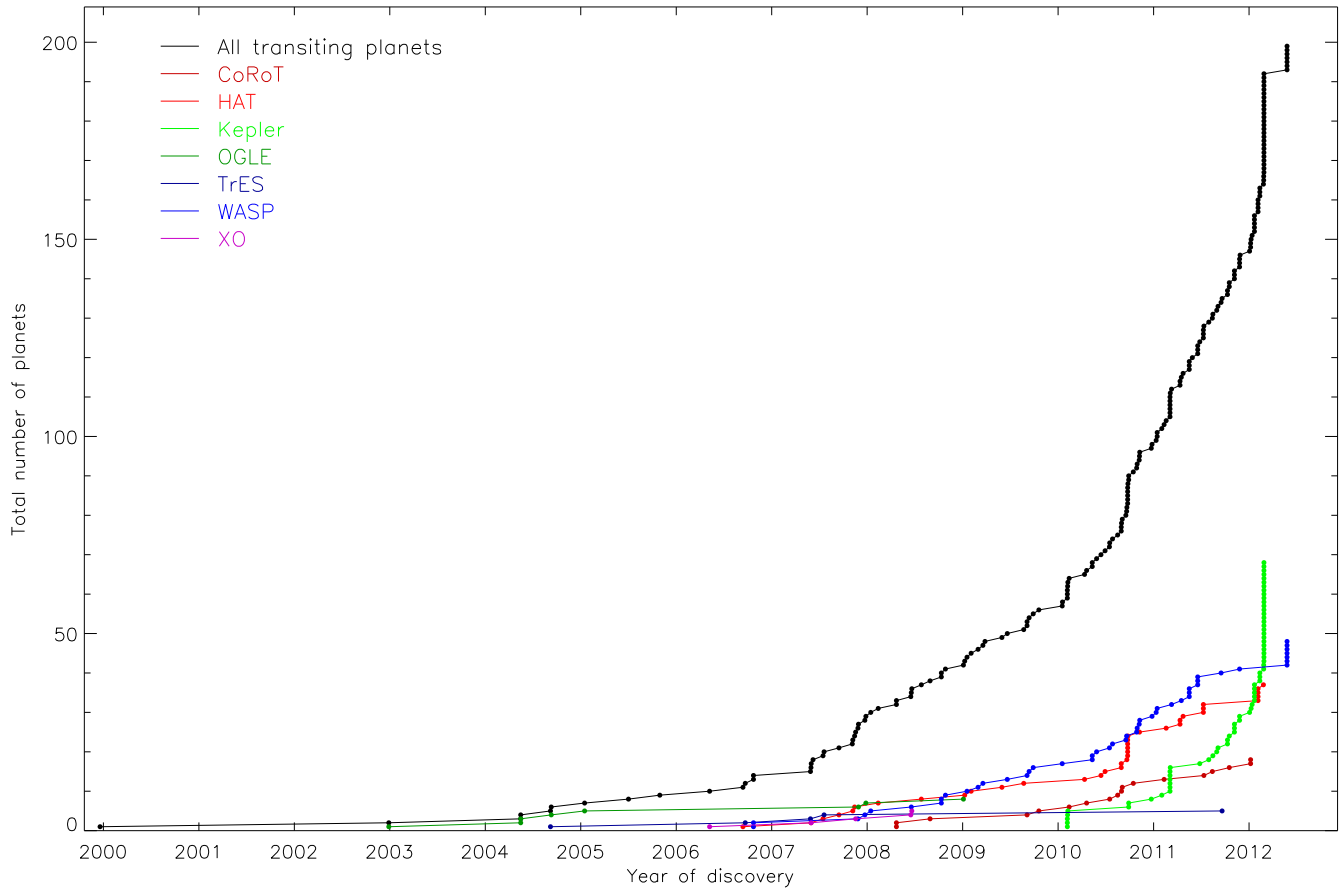

Figure 38. Plot of the discovery rate of the known TEPs. The total number is shown by the upper black line, whereas the discovery rate of selected individual surveys are indicated below this using coloured lines as indicated in the key on the top left of the plot (please see the electronic version of this paper for the colour figure).

Table 6. Limits of the current ephemerides of the known TEPs. The two dates for each TEP indicate the first transits whose midpoints are uncertain by 1 hour and by half the transit duration. RHJD = HJD − 24000000. The *Kepler* planets are not included because they are the subject of continued observations using the satellite.

TEP	1 hour uncertainty		Half-transit uncertainty	
	RHJD	UT date	RHJD	UT date
CoRoT-04	55181.195810	2009 12 15	56432.674610	2013 05 20
CoRoT-14	55268.529920	2010 03 13	55186.874360	2009 12 21
CoRoT-17	55447.075200	2010 09 07	56163.014200	2012 08 23
CoRoT-20	56550.756250	2013 09 15	56698.641850	2014 02 10
HAT-P-31	56573.327850	2013 10 07	60137.190450	2023 07 11
CoRoT-23	56823.191100	2014 06 14	58250.292000	2018 05 11
CoRoT-10	57040.629000	2015 01 18	58377.929600	2018 09 16
CoRoT-09	57461.558700	2016 03 14	66131.474500	2039 12 08
OGLE-211	58524.988640	2019 02 10	64688.042880	2035 12 26
CoRoT-08	58780.283621	2019 10 23	60451.414110	2024 05 20
CoRoT-15	59004.400840	2020 06 03	61639.370800	2027 08 21
Qatar-1	59217.596165	2021 01 03	58499.059467	2019 01 15

8 DISCOVERY RATE AND SKY POSITIONS OF THE TRANSITING EXTRASOLAR PLANETARY SYSTEMS

Whilst scientifically less relevant than the analyses described above, the discovery rate of the transiting planets is of sufficient interest to be worthy of discussion. Fig. 38 shows the discovery rate of the known TEPs. For discovery time I have taken the date at which important details[13] of that system became available in a refereed journal article. If the article was lodged on the arXiv[14] preprint server prior to this, I have instead taken the date at which this preprint became public.

The population of known TEPs continues to increase at an exponential rate; a plot of Fig. 38 but with a logarithmic ordinate axis (not shown) exhibits an approximately straight line. The early front-runners were the OGLE survey (including the follow-up observations which were performed by a range of associated and independent consortia), but the SuperWASP consortium (Pollacco et al. 2006) held the lead during the years 2009-11. The greatest number of known TEPs is now attributable to data obtained by the *Kepler* satellite, and once again this number includes both associated and independent groups of researchers. *Kepler* has now been used to find over 2000 candidate TEPs (Batalha et al. 2012) and possibly as many as 5000 (Tenenbaum et al. 2012); the rate of false positives is probably small but remains under discussion (Morton &

[13] I define the 'important details' to comprise confirmation of the planetary nature of the system (which in turn requires an assessment of the physical properties of the putative planet) and sufficient information to allow the execution of follow-up observations (i.e. the full sky position and orbital ephemerides).

[14] `http://arxiv.org/`

Johnson 2011; Santerne et al. 2012; Colón et al. 2012). The candidate list provides the ammunition to continue the exponential rise in the number of known TEPs.

Fig. 39 shows the sky positions of the known TEPs, overlaid with the celestial equator and galactic plane, and is a good tool to illustrate the strength and diversity of the selection effects which afflict this population. The most obvious feature in Fig. 39 is a strong clustering around 19 hr right ascension and $+42^\circ$ declination, which is the *Kepler* field. The *Kepler* satellite (Borucki et al. 2010) is currently the most successful TEP discovery machine, and has a modest field of view (105 deg^2). This concentration of points is the result.

Additional clusters of TEPs occur around the intersections of the Galactic plane with the celestial equator, the two areas targeted by the CoRoT satellite (Baglin et al. 2006). CoRoT aims for these positions in order to obtain a high surface density of stars (to give plenty of targets in its small 8.2 deg^2 field of view) which are easily followed up using ground-based telescopes in both hemispheres. Two other small groups of TEPs come via the OGLE survey (Udalski et al. 2002c) observations of the Galactic centre (18 hr R.A. and -30° Dec) and Carina regions (11 hr R.A. and -60° Dec).

The wider spread of objects in Fig. 39 is dominated by HAT (Bakos et al. 2002) in the north and SuperWASP (Pollacco et al. 2006) in the south[15]. These, plus other similar projects, operate multiple small wide-field telescopes with very coarse pixel scales. They are thus able to cover large amounts of sky but must avoid the crowded fields towards the Galactic plane, due to problems with blending. Blending makes it more difficult to measure good photometry and also elevates the rate of false alarms in a search for TEPs.

The surveys operating small ground-based telescopes tend to point away from the Galactic plane, which introduces a bias towards intrinsically faint stars. This is advantageous because it reduces the fraction of giants in the studied sample; these surveys cannot find planets around giant stars but are able to detect larger transiting object which are of lesser scientific interest. Conversely, the *Kepler* satellite studies stars with fainter apparent magnitudes which are located close to the Galactic plane. These stars have slightly different population characteristics to those studied by other surveys with different designs; Schlaufman & Laughlin (2011) show that the host stars of the *Kepler* planet candidates are preferentially metal-rich. Such biases must be accounted for when studying the population characteristics of the known TEPs and their host stars.

9 SUMMARY

The *Homogeneous Studies* project aims to provide measurements of the physical properties of a large sample of transiting extrasolar planetary systems, using consistent methods and with careful attention paid to the estimation of robust statistical and systematic errors. The transit light curves are modelled using the JKTEBOP code, and uncertainties are gauged with Monte Carlo and residual-permutation algorithms. Attention is paid to the treatment of limb darkening, orbital eccentricity, and contaminating 'third' light. To the resulting photometric parameters are added measured spectroscopic quantities: the $T_{\rm eff}$, $\left[\frac{\rm Fe}{\rm H}\right]$ and velocity amplitude of the host star. One additional constraint is needed, and is supplied either by one of five sets of theoretical stellar evolutionary models or by a semi-empirical calibration of low-mass star properties based on detached eclipsing binaries. The statistical errors are propagated using a perturbation algorithm, leading to complete error budgets for each output quantity. The inclusion of multiple stellar models allows systematic errors to be deduced too.

The current paper has presented complete analyses of thirty TEP systems, and updated the physical properties of eight more systems based on newly published spectroscopic results. Combined with previous work, this yields a total of 82 transiting planets and host stars with homogeneously-measured physical properties. In many cases these results are based on more numerous datasets than previous measurements, so should be preferred over literature values even if homogeneity is not of specific importance to the matter in hand. Headline results from the current paper are summarised below.

Analyses in the current work were the first to consider all available good light curves for HAT-P-3 (five datasets), HAT-P-6 (three), HAT-P-9 (four), HAT-P-14 (four), WASP-12 (four) and WASP-14 (four). For WASP-14 this has resulted in a change in planetary radius ($R_{\rm b}$) from $1.281^{+0.075}_{-0.082}\,{\rm R_{Jup}}$ to $1.633 \pm 0.092 \pm 0.009\,{\rm R_{Jup}}$, moving this object away from the parameter space occupied by theoretical predictions.

The current study is also the first to present results based on short-cadence data for Kepler-14, Kepler-15 and KOI-135. The measured mass of Kepler-14 A has decreased by 2.6σ, and the measured radii of both components in the Kepler-15 system are both significantly larger. The density deduced for Kepler-15 b is lower by a factor of two compared to previous studies.

Additional data was modelled for KOI-196, KOI-204, KOI-254, KOI-423 and KOI-428. In two cases (KOI-423 and KOI-428) the available data is more than a factor three more extensive than used in published studies. For KOI-428 the radii of the components are larger than previously found; the star is now comfortably the largest known known to host a TEP at $R_{\rm A} = 2.48 \pm 0.17 \pm 0.20\,{\rm R_\odot}$.

The physical properties of OGLE-TR-56 have been heavily revised based on the first complete analysis of newly-published high-quality photometry (Adams et al. 2011b). The radius of the planet is $R_{\rm b} = 1.73 \pm 0.06\,{\rm R_{Jup}}$, which is much larger than all previous determinations (1.23–1.38 $\rm R_{Jup}$). This radius makes OGLE-TR-56 b one of the largest known planets, as expected for its high equilibrium temperature and hot and massive host star. Its measured density is smaller by a factor of three. Previous analyses were based either on survey-quality photometry, a single transit light curve which is now known to be strongly affected by correlated noise, or on unnecessary assumptions. Two morals can be deduced from this. Firstly, one should always use a newly-derived stellar density in calculating revised physical properties of a TEP system. Secondly, results based on only one transit light curve cannot be definitive as systematic errors may lurk undetected in the data.

New results have also been calculated for OGLE-TR-111, OGLE-TR-113, OGLE-TR-132 and OGLE-TR-L9. These comprise the first complete analyses of recently published high-quality photometry for each system.

For WASP-13 and WASP-21 my analysis has resulted in the upward revision of the planetary radii, making them two of the least dense planets known. For WASP-13 $R_{\rm b}$ changes from $1.389^{+0.045}_{-0.056}\,{\rm R_{Jup}}$ to $1.528 \pm 0.084 \pm 0.004\,{\rm R_{Jup}}$, and for WASP-21 the change is from $1.143^{+0.045}_{-0.030}\,{\rm R_{Jup}}$ to $1.263 \pm 0.085 \pm$

[15] Declaration of bias: the author is a member of the SuperWASP consortium.

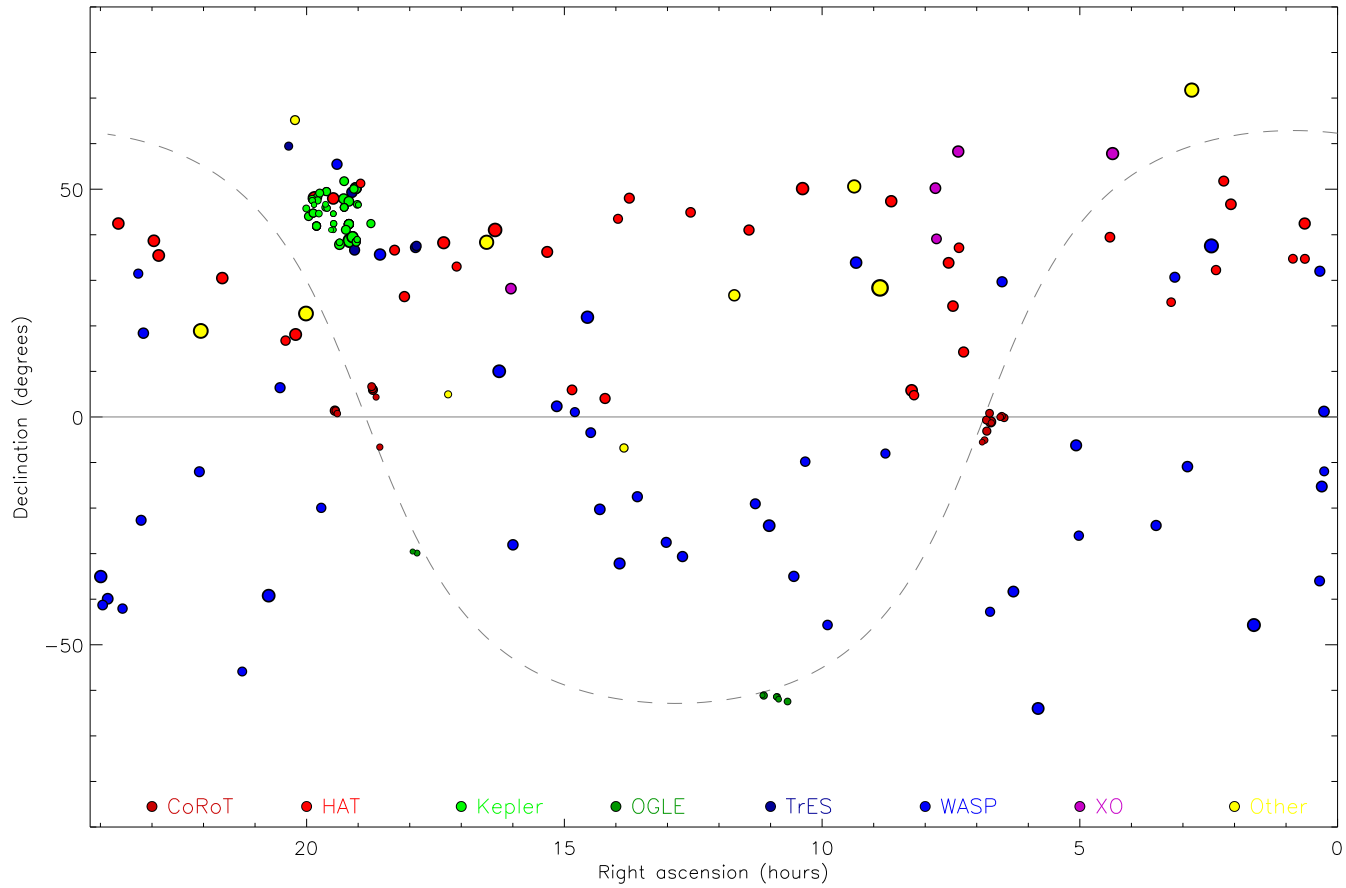

Figure 39. Plot of the sky positions of the known TEP systems. The celestial equator is shown using a solid grey line and the plane of the Milky Way galaxy with a dashed grey line. The TEPs are colour-coded to indicate those found by selected discovery surveys (please see the electronic version of this paper for the colour figure).

$0.029\,\mathrm{R_{Jup}}$. Finally, the inclusion of an improved $T_{\rm eff}$ measurement makes WASP-2 one of the best-understood TEP systems.

Previously found correlations between $P_{\rm orb}$ and planet gravity, and $P_{\rm orb}$ and planet mass, have been revisited and found to be of improved statistical significance (3.9σ and 3.8σ respectively). The division of TEPs into two classes based on their Safronov number is shown to be spurious.

I recommend further observations of specific types for the majority of the objects studied here. These are summarised in Sect. 7. In particular, some orbital ephemerides are of low precision and will soon be of limited use. The affected systems would benefit from new transit photometry to solve this problem. Finally, the discovery rate and distribution of sky positions of the known TEPs are plotted and discussed.

The main results from this work will be made available in a convenient format in the *Transiting Extrasolar Planets Catalogue* (TEPCat[16]).

ACKNOWLEDGMENTS

I acknowledge financial support from STFC in the form of an Advanced Fellowship. I am grateful to Barry Smalley for many conversations and to Conrad Vilela for discussions about the *Kepler* archive. I am grateful for data provided by Joel Hartmann (HAT-P-6 and HAT-P-9), Neale Gibson (HAT-P-3), Guillaume Hébrard (CoRoT-18), Jason Dittmann (HAT-P-9), Pedro Sada (HAT-P-9), Kamen Todorov (HAT-P-9) and Monika Lendl (OGLE-TR-L9). I thank the CDS, MAST, IAS and NSTeD websites for archiving the many datasets now available for transiting planets. The following internet-based resources were used in research for this paper: the ESO Digitized Sky Survey; the NASA Astrophysics Data System; the SIMBAD database operated at CDS, Strasbourg, France; and the arχiv scientific paper preprint service operated by Cornell University.

[16] The Transiting Extrasolar Planet Catalogue (TEPCat) is available at `http://www.astro.keele.ac.uk/jkt/tepcat/`

REFERENCES

Adams, E. R., López-Morales, M., Elliot, J. L., Seager, S., Osip, D. J., 2010a, ApJ, 714, 13
Adams, E. R., López-Morales, M., Elliot, J. L., Seager, S., Osip, D. J., 2010b, ApJ, 721, 1829
Adams, E. R., López-Morales, M., Elliot, J. L., Seager, S., Osip, D. J., 2011a, ApJ, 728, 125
Adams, E. R., et al., 2011b, ApJ, 741, 102
Albrecht, S., Winn, J. N., Butler, R. P., Crane, J. D., Shectman, S. A., Thompson, I. B., Hirano, T., Wittenmyer, R. A., 2012, ApJ, 744, 189

Albrecht, S., et al., 2011, ApJ, 738, 50
Anderson, D. R., et al., 2010, ApJ, 709, 159
Anderson, D. R., et al., 2011, MNRAS, 416, 2108
Arras, P., Burkart, J., Quataert, E., Weinberg, N. N., 2012, MNRAS, 422, 1761
Baglin, A., et al., 2006, in 36th COSPAR Scientific Assembly, COSPAR, 75039 Paris Cedex 01, France, vol. 36 of *COSPAR, Plenary Meeting*, p. 3749
Bakos, G. Á., Lázár, J., Papp, I., Sári, P., Green, E. M., 2002, PASP, 114, 974
Barros, S. C. C., Pollacco, D. L., Gibson, N. P., Howarth, I. D., Keenan, F. P., Simpson, E. K., Skillen, I., Steele, I. A., 2011, MNRAS, 416, 2593
Barros, S. C. C., Pollacco, D. L., Gibson, N. P., Keenan, F. P., Skillen, I., Steele, I. A., 2012, MNRAS, 419, 1248
Batalha, N. M., et al., 2012, ApJS submitted, arXiv:1202.5852
Blackwell, D. E., Shallis, M. J., 1977, MNRAS, 180, 177
Blackwell, D. E., Petford, A. D., Shallis, M. J., 1980, A&A, 82, 249
Blecic, J., et al., 2011, ApJ, submitted, arXiv:1111.2363
Bodenheimer, P., Laughlin, G., Lin, D. N. C., 2003, ApJ, 592, 555
Bonomo, A. S., et al., 2012, A&A, 538, A96
Borucki, W. J., et al., 2010, Science, 327, 977
Borucki, W. J., et al., 2011, ApJ, 728, 117
Bouchy, F., Pont, F., Santos, N. C., Melo, C., Mayor, M., Queloz, D., Udry, S., 2004, A&A, 421, L13
Bouchy, F., Pont, F., Melo, C., Santos, N. C., Mayor, M., Queloz, D., Udry, S., 2005, A&A, 431, 1105
Bouchy, F., et al., 2010, A&A, 519, A98
Bouchy, F., et al., 2011, A&A, 533, A83
Brown, T. M., Latham, D. W., Everett, M. E., Esquerdo, G. A., 2011, AJ, 142, 112
Bruntt, H., et al., 2010a, MNRAS, 405, 1907
Bruntt, H., et al., 2010b, A&A, 519, A51
Bruntt, H., et al., 2012, MNRAS, 423, 122
Buchhave, L. A., et al., 2011, ApJS, 197, 3
Budaj, J., 2011, AJ, 141, 59
Burke, C. J., et al., 2007, ApJ, 671, 2115
Campo, C. J., et al., 2011, ApJ, 727, 125
Chabrier, G., Baraffe, I., Leconte, J., Gallardo, J., Barman, T., 2009, in American Institute of Physics Conference Series, vol. 1094 of *American Institute of Physics Conference Series*, p. 102
Chan, T., Ingemyr, M., Winn, J. N., Holman, M. J., Sanchis-Ojeda, R., Esquerdo, G., Everett, M., 2011, AJ, 141, 179
Charbonneau, D., Brown, T. M., Latham, D. W., Mayor, M., 2000, ApJ, 529, L45
Claret, A., 2004, A&A, 424, 919
Claret, A., 2005, A&A, 440, 647
Claret, A., 2006, A&A, 453, 769
Claret, A., 2007, A&A, 467, 1389
Collier Cameron, A., et al., 2007, MNRAS, 375, 951
Colón, K. D., Ford, E. B., Morehead, R. C., 2012, MNRAS submitted, arXiv:1207.2481
Cowan, N. B., Machalek, P., Croll, B., Shekhtman, L. M., Burrows, A., Deming, D., Greene, T., Hora, J. L., 2012, ApJ, 747, 82
Croll, B., Lafreniere, D., Albert, L., Jayawardhana, R., Fortney, J. J., Murray, N., 2011, AJ, 141, 30
Csizmadia, S., et al., 2011, A&A, 531, A41
Daemgen, S., Hormuth, F., Brandner, W., Bergfors, C., Janson, M., Hippler, S., Henning, T., 2009, A&A, 498, 567
Deleuil, M., et al., 2012, A&A, 538, A145
Demarque, P., Woo, J.-H., Kim, Y.-C., Yi, S. K., 2004, ApJS, 155, 667
Demory, B.-O., et al., 2011, ApJ, 735, L12
Désert, J.-M., et al., 2011, ApJS, 197, 14
Díaz, R. F., Rojo, P., Melita, M., Hoyer, S., Minniti, D., Mauas, P. J. D., Ruíz, M. T., 2008, ApJ, 682, L49
Díaz, R. F., et al., 2007, ApJ, 660, 850
Dittmann, J. A., Close, L. M., Scuderi, L. J., Turner, J., Stephenson, P. C., 2012, New Astronomy, 17, 438
Dotter, A., Chaboyer, B., Jevremović, D., Kostov, V., Baron, E., Ferguson, J. W., 2008, ApJS, 178, 89
Doyle, L. R., et al., 2011, Science, 333, 1602
Dragomir, D., et al., 2011, AJ, 142, 115
Endl, M., et al., 2011, ApJS, 197, 13
Enoch, B., Collier Cameron, A., Parley, N. R., Hebb, L., 2010, A&A, 516, A33
Enoch, B., Collier Cameron, A., Horne, K., 2012, A&A, 540, A99
Fortney, J. J., Marley, M. S., Barnes, J. W., 2007, ApJ, 659, 1661
Fortney, J. J., et al., 2011, ApJS, 197, 9
Fossati, L., et al., 2010, ApJ, 720, 872
Ghezzi, L., Cunha, K., Smith, V. V., de Araújo, F. X., Schuler, S. C., de la Reza, R., 2010, ApJ, 720, 1290
Gibson, N. P., et al., 2008, A&A, 492, 603
Gilliland, R. L., et al., 2010, ApJ, 713, L160
Gillon, M., Pont, F., Moutou, C., Bouchy, F., Courbin, F., Sohy, S., Magain, P., 2006, A&A, 459, 249
Gillon, M., et al., 2007, A&A, 466, 743
Gillon, M., et al., 2009, A&A, 496, 259
Gillon, M., et al., 2010, A&A, 511, A3
Gillon, M., et al., 2011, A&A, 533, A88
Giménez, A., 2006, A&A, 450, 1231
Goldreich, P., Soter, S., 1966, Icarus, 5, 375
Grether, D., Lineweaver, C. H., 2006, ApJ, 640, 1051
Guenther, E. W., et al., 2012, A&A, 537, A136
Hansen, B. M. S., Barman, T., 2007, ApJ, 671, 861
Harmanec, P., Prša, A., 2011, PASP, 123, 976
Hebb, L., et al., 2009, ApJ, 693, 1920
Hébrard, G., et al., 2010, A&A, 516, A95
Hébrard, G., et al., 2011a, A&A, 527, L11
Hébrard, G., et al., 2011b, A&A, 533, A130
Hellier, C., et al., 2009a, Nature, 460, 1098
Hellier, C., et al., 2009b, ApJ, 690, L89
Henry, G. W., Marcy, G. W., Butler, R. P., Vogt, S. S., 2000, ApJ, 529, L41
Hilditch, R. W., 2001, An Introduction to Close Binary Stars, Cambridge University Press, Cambridge, UK
Hoyer, S., Rojo, P., López-Morales, M., Díaz, R. F., Chambers, J., Minniti, D., 2011, ApJ, 733, 53
Husnoo, N., et al., 2011, MNRAS, 413, 2500
Jenkins, J. M., et al., 2010, ApJ, 713, L120
Johnson, J. A., Winn, J. N., Albrecht, S., Howard, A. W., Marcy, G. W., Gazak, J. Z., 2009, PASP, 121, 1104
Johnson, J. A., et al., 2012, AJ, 143, 111
Joshi, Y. C., et al., 2009, MNRAS, 392, 1532
Kane, S. R., Mahadevan, S., von Braun, K., Laughlin, G., Ciardi, D. R., 2009, PASP, 121, 1386
Kipping, D. M., 2008, MNRAS, 389, 1383
Kipping, D. M., Bakos, G. Á., 2011, ApJ, 730, 50
Konacki, M., Torres, G., Jha, S., Sasselov, D. D., 2003, Nature, 421, 507
Latham, D. W., et al., 2010, ApJ, 713, L140

Léger, A., et al., 2009, A&A, 506, 287
Lendl, M., Afonso, C., Koppenhoefer, J., Nikolov, N., Henning, T., Swain, M., Greiner, J., 2010, A&A, 522, A29
Lissauer, J. J., et al., 2011, Nature, 470, 53
López-Morales, M., 2007, ApJ, 660, 732
López-Morales, M., Coughlin, J. L., Sing, D. K., Burrows, A., Apai, D., Rogers, J. C., Spiegel, D. S., Adams, E. R., 2010, ApJ, 716, L36
Lucy, L. B., Sweeney, M. A., 1971, AJ, 76, 544
Maciejewski, G., Errmann, R., Raetz, S., Seeliger, M., Spaleniak, I., Neuhäuser, R., 2011, A&A, 528, A65
Madhusudhan, N., et al., 2011, Nature, 469, 64
Mandel, K., Agol, E., 2002, ApJ, 580, L171
Mandushev, G., et al., 2007, ApJ, 667, L195
Maxted, P. F. L., Koen, C., Smalley, B., 2011, MNRAS, 418, 1039
Mazeh, T., Zucker, S., Pont, F., 2005, MNRAS, 356, 955
McLaughlin, D. B., 1924, ApJ, 60, 22
Minniti, D., et al., 2007, ApJ, 660, 858
Morton, T. D., Johnson, J. A., 2011, ApJ, 738, 170
Moutou, C., Pont, F., Bouchy, F., Mayor, M., 2004, A&A, 424, L31
Moutou, C., et al., 2011, A&A, 533, A113
Narita, N., Hirano, T., Sanchis-Ojeda, R., Winn, J. N., Holman, M. J., Sato, B., Aoki, W., Tamura, M., 2010, PASJ, 62, L61
Narita, N., Hirano, T., Sato, B., Harakawa, H., Fukui, A., Aoki, W., Tamura, M., 2011, PASJ, 63, L67
Nascimbeni, V., Piotto, G., Bedin, L. R., Damasso, M., 2011, A&A, 527, A85
Noyes, R. W., et al., 2008, ApJ, 673, L79
Pietrinferni, A., Cassisi, S., Salaris, M., Castelli, F., 2004, ApJ, 612, 168
Pollacco, D. L., et al., 2006, PASP, 118, 1407
Pont, F., Bouchy, F., Queloz, D., Santos, N. C., Melo, C., Mayor, M., Udry, S., 2004, A&A, 426, L15
Pont, F., Husnoo, N., Mazeh, T., Fabrycky, D., 2011, MNRAS, 414, 1278
Pont, F., et al., 2007, A&A, 465, 1069
Ribas, I., Morales, J. C., Jordi, C., Baraffe, I., Chabrier, G., Gallardo, J., 2008, Memorie della Societa Astronomica Italiana, 79, 562
Rossiter, R. A., 1924, ApJ, 60, 15
Rouan, D., et al., 2012, A&A, 537, A54
Sada, P. V., et al., 2012, PASP, 124, 212
Safronov, V. S., 1972, Evolution of the Protoplanetary Cloud and Formation of the Earth and Planets (Jerusalem: Israel Program for Scientific Translation)
Santerne, A., Bonomo, A. S., Hébrard, G., Deleuil, M., Moutou, C., Almenara, J.-M., Bouchy, F., Díaz, R. F., 2011a, A&A, 536, A70
Santerne, A., et al., 2011b, A&A, 528, A63
Santerne, A., et al., 2012, A&A submitted, arXiv 1206.0601
Santos, N. C., et al., 2006, A&A, 458, 997
Schlaufman, K. C., Laughlin, G., 2011, ApJ, 738, 177
Schröter, S., Czesla, S., Wolter, U., Müller, H. M., Huber, K. F., Schmitt, J. H. M. M., 2011, A&A, 532, A3
Seager, S., Mallén-Ornelas, G., 2003, ApJ, 585, 1038
Shporer, A., Mazeh, T., Pont, F., Winn, J. N., Holman, M. J., Latham, D. W., Esquerdo, G. A., 2009a, ApJ, 694, 1559
Shporer, A., et al., 2009b, ApJ, 690, 1393
Simpson, E. K., et al., 2011, AJ, 141, 161
Skillen, I., et al., 2009, A&A, 502, 391
Snellen, I. A. G., Covino, E., 2007, MNRAS, 375, 307
Snellen, I. A. G., et al., 2009, A&A, 497, 545
Southworth, J., 2008, MNRAS, 386, 1644, (Paper I)
Southworth, J., 2009, MNRAS, 394, 272, (Paper II)
Southworth, J., 2010, MNRAS, 408, 1689, (Paper III)
Southworth, J., 2011, MNRAS, 417, 2166, (Paper IV)
Southworth, J., Maxted, P. F. L., Smalley, B., 2004, MNRAS, 351, 1277
Southworth, J., Maxted, P. F. L., Smalley, B., 2005, A&A, 429, 645
Southworth, J., Wheatley, P. J., Sams, G., 2007, MNRAS, 379, L11
Southworth, J., Bruni, I., Mancini, L., Gregorio, J., 2012a, MNRAS, 420, 2580
Southworth, J., et al., 2009a, MNRAS, 396, 1023
Southworth, J., et al., 2009b, MNRAS, 399, 287
Southworth, J., et al., 2009c, ApJ, 707, 167
Southworth, J., et al., 2010, MNRAS, 408, 1680
Southworth, J., et al., 2011, A&A, 527, A8
Southworth, J., et al., 2012b, MNRAS, submitted
Sozzetti, A., et al., 2009, ApJ, 691, 1145
Spearman, C., 1904, American Journal of Psychology, 15, 72
Swain, M., et al., 2012, Icarus, submitted, arXiv:1205.4736
Tenenbaum, P., et al., 2012, ApJS, 199, 24
Todorov, K. O., et al., 2012, ApJ, 746, 111
Torres, G., Konacki, M., Sasselov, D. D., Jha, S., 2004, ApJ, 609, 1071
Torres, G., Winn, J. N., Holman, M. J., 2008, ApJ, 677, 1324
Torres, G., et al., 2007, ApJ, 666, L121
Torres, G., et al., 2010, ApJ, 715, 458
Triaud, A. H. M. J., et al., 2010, A&A, 524, A25
Udalski, A., Szewczyk, O., Zebrun, K., Pietrzynski, G., Szymanski, M., Kubiak, M., Soszynski, I., Wyrzykowski, L., 2002a, Acta Astronomica, 52, 317
Udalski, A., Zebrun, K., Szymanski, M., Kubiak, M., Soszynski, I., Szewczyk, O., Wyrzykowski, L., Pietrzynski, G., 2002b, Acta Astronomica, 52, 115
Udalski, A., Pietrzynski, G., Szymanski, M., Kubiak, M., Zebrun, K., Soszynski, I., Szewczyk, O., Wyrzykowski, L., 2003, Acta Astronomica, 53, 133
Udalski, A., et al., 2002c, Acta Astronomica, 52, 1
VandenBerg, D. A., Bergbusch, P. A., Dowler, P. D., 2006, ApJS, 162, 375
von Braun, K., et al., 2012, ApJ, 753, 171
Welsh, W. F., et al., 2012, Nature, 481, 475
Winn, J. N., Holman, M. J., Fuentes, C. I., 2007, AJ, 133, 11
Winn, J. N., et al., 2011, AJ, 141, 63